

# KOBELCO TECHNOLOGY REVIEW

No. **41** Mar. 2024

**Feature : Welding and Joining Technologies**

## Contents

Development of Non-short-circuit-type Wire Feed Control GMAW Process  
“AXELARC™” ..... 1

Yoshiaki KITAMURA · Dr. Kei YAMAZAKI · Shogo NAKATSUKASA · Akira OGAWA · Yoshihide INOUE · Hiroshi HASHIMOTO

Welding Machine “SENSARC™ RA500” with Highly Efficient Welding  
Processes ..... 9

Shogo NAKATSUKASA · Akira OGAWA · Eiji SATO · Baini JO · Shota SEKIGUCHI

Digital Transformation (DX) Technology to Promote Adoption of Welding Robot  
Systems ..... 16

Atsushi FUKUNAGA · Kazuki HIDAKA · Takaya HIGASHIRA · Fumiaki SAWAKAWA · Kohei MATSUSHIMA · Kohei KOMUKAI

Robotic Welding System with New Equipment for Steel Structures ..... 23

Takao TOGAWA · Baini JO · Ryohei KURIYAMA · Shimpei KAWANISHI · Hirohisa KISHIKAWA · Taisei FUJIMOTO

Welding Process and Welding Consumables for Offshore Wind Power Generation  
Facilities ..... 30

Kosuke YAMAGUCHI · Satoru KANO

Development of Automatic Welding System for 9% Ni Steel LNG Tanks ..... 36

Kenta YAMASAKI · Hirofumi MANIWA · Dr. Yoshihiko KITAGAWA · Tsuyoshi MIWA · Keito ISHIZAKI

Welding Consumables for 780 MPa Class Steel with Excellent Notch Toughness after  
PWHT ..... 43

Satoru KANO · Masayuki NAGAMI · Masahiro INOMOTO · Dr. Takanori ITO

Effect of Tungsten (W) on Creep Properties of 9Cr-3W-3Co-Nd-B Steel Weld  
Metals ..... 48

Hiroimi OYAMADA · Hideaki TAKAUCHI · Shigenobu NANBA

Slag Control Technology to Improve Electrodeposition Coatability of Arc Weld  
Joints ..... 53

Hikaru KINASHI · Yue SUN · Kazuya IKAI

Influence of LME Cracks in Resistance Spot Welds of Zinc-coated Ultra-high  
Strength Steel Sheets on Joint Strength ..... 61

Kyohei MAEDA · Dr. Reiichi SUZUKI · Masao HADANO

Metal Surface Preparation Technology for Adhesive Joining Reliability ..... 70

Dr. Yusuke TAKAHASHI · Shintaro YAMAMOTO · Daiki KATSUNO · Yoko MURATA

Editor-in-chief :  
Yuichiro GOTO  
Associate Editor :  
Masao KINEFUCHI

Editorial Committee :  
Yasuyuki YOKOTA  
Koichi HONKE  
Hideo IKEDA  
Katsushige NISHIGUCHI  
Kentaro NOZAWA  
Hiroki SANARI  
Hiroshi SUGITATSU  
Reiichi SUZUKI  
Shinya TAKAKU  
Toshiro YAMASHITA

Published by

**Technical Development Group  
Kobe Steel, Ltd.**

5-5, Takatsukadai 1-chome,  
Nishi-ku, Kobe, HYOGO 651-2271, JAPAN  
<https://www.kobelco.co.jp>

Editorial Office: **Kobelco Business Partners  
Co., Ltd.**

2-4, Wakinohama-Kaigandori 2-chome,  
Chuo-ku, Kobe, HYOGO 651-8585,  
JAPAN  
Fax: +81-78-261-7843  
E-mail: [rd-office@kobelco.com](mailto:rd-office@kobelco.com)

© Kobe Steel, Ltd. 2024

# Development of Non-short-circuit-type Wire Feed Control GMAW Process “AXELARC™”

Yoshiaki KITAMURA\*1 • Dr. Kei YAMAZAKI\*2 • Shogo NAKATSUKASA\*2 • Akira OGAWA\*2 • Yoshihide INOUE\*2 • Hiroshi HASHIMOTO\*3

\*1 Technical Center, Welding Business (currently Planning & Administration Department, Technical Development Group)

\*2 Technical Center, Welding Business

\*3 Mechanical Engineering Research Laboratory, Technical Development Group

## Abstract

*While conventional short-circuit wire feed control processes are effective in achieving low spatter and low-heat-input welding, they present challenges when it comes to high-current ranges, medium-to-thick plates, and multi-layer multi-pass welding. To address this issue, the world’s first non-short-circuit-type wire feed control process, AXELARC™, has been developed, in which the process leverages the inertia for droplet transfer by alternating the wire feed direction forward and backward. The applicability of the process to the field of medium-to-thick plates has been examined. The results confirm its ability to achieve low spatter and low fume welding in a wide range of conditions, from low to high currents. Additionally, it enables deep penetration, high deposition, and high-speed welding capabilities. The newly developed process is expected to make a significant contribution to improving welding quality and efficiency in the field of medium-to-thick plates.*

## Introduction

In the gas shielded metal arc welding process, the welding wire serves as the electrode. The electrode wire melts due to the Joule heat and the arc heat at the wire extension. As the droplet detaches from the wire tip, the arc length changes. In other words, the frequency of droplet transfer and the droplet size are factors that govern the arc stability, and droplets that cannot transfer smoothly may lead to spatter and fume emission. Therefore, in the arc-welding process, advanced technologies of droplet transfer control play significant roles in increasing efficiency, improving welding quality and pursuing further functional enhancement. Typical droplet transfer control technologies so far include the method of detecting necking of a droplet during the short circuit transfer process and controlling the current waveform,<sup>1)</sup> as well as the method of regularly detaching droplets by changing the welding current pulse-wise, as in pulsed MAG and MIG welding.<sup>2)</sup> These methods balance external forces acting on the droplet, such as surface tension, electromagnetic force, shear force caused by plasma stream, and arc pressure, through the operation of the welding

current waveform. However, relying solely on the control of external force balance through the current waveform makes it challenging to expect significant progress in the arc welding process in the future.

Hence, Kobe Steel has developed the world’s first wire feed control process, AXELARC™<sup>Note 1)</sup>, which utilizes “inertia” as a new droplet transfer control factor by changing the wire feed direction and speed over time and reversing the wire feed direction. This paper introduces an overview of AXELARC™ and provides an example of its effectiveness.

## 1. Overview of the newly developed non-short-circuit-type wire feed control process, AXELARC™

### 1.1 Outlines and issues of short-circuit wire feed control processes

In recent years, an extremely low-spatter and low-heat-input welding method has been gaining popularity, especially in the field of thin-plate welding. This method closely coordinates welding current waveform control with wire feed control by AC servo motors. Various welding processes have been introduced by welding equipment manufacturers in Japan and other countries.<sup>3-7)</sup> The droplet transfer mode for these welding processes, using wire feed control, is consistently the short-circuit transfer mode. When the droplet at the tip of the welding wire short-circuits to the molten pool, the welding current is reduced, and reversing and retracting the welding wire opens the short circuit. The common feature is the significant reduction of spatter generation upon the re-establishment of the arc. These short-circuit wire feed control processes have the advantage of suppressing short-circuit currents, achieving lower heat input compared with conventional short-circuit welding processes, which is particularly beneficial for extremely thin plates, around 1.0 mm thick, reducing distortion and preventing burn-through.

However, this excellent low-spatter effect mainly relies on the stabilization of the short-

Note 1) AXELARC is a registered trademark (TM) of Kobe Steel.

circuit transfer phenomenon in the low current range, and maintaining a similar droplet transfer mode and its benefits in the high current range is generally challenging. Moreover, assuming short-circuit transfer as the basis results in shallow penetration and high weld reinforcement, often leading to a narrow convex bead shape. Increasing the welding current (wire melting rate) to enhance welding efficiency exacerbates this convex bead formation tendency. Consequently, the efficiency improvements sought in the medium-to-thick plate welding field, including high current and faster welding speeds, become less attainable. Additionally, when performing multi-layer, multi-path welding within a groove, issues like insufficient penetration and lack of fusion become more likely, presenting challenges for the application of short-circuit wire feed control processes in medium-to-thick plate welding. In contrast, AXELARC™ assumes no short-circuiting of the droplet at the wire tip with the molten pool. This means it's a process developed to overcome the challenges associated with the short-circuit wire feed control processes mentioned above. It holds the potential for application in medium-to-thick plate welding.

## 1.2 System configuration of AXELARC™

The configuration of the experimental apparatus for the AXELARC™ process is shown in Fig. 1. The feeding unit of this system comprises a push feeder that forwards the wire at a set speed, a pull feeder integrated into the welding torch, and a servo driver that controls the pull feeder. Furthermore, a wire buffer mechanism has been provided between the push feeder and the pull feeder to detect and correct errors in the amount of wire feeding. A mild-steel solid wire with a diameter of 1.2 mm, subjected to a special surface treatment, is used as the welding wire, and 100 % CO<sub>2</sub> is used for the shielding gas.

## 1.3 Droplet transfer mode for AXELARC™

Fig. 2 schematically illustrates the welding current waveform and wire feed speed waveform for AXELARC™ and presents images with examples of droplet transfer. The forward and backward feeding of the wire occurs repeatedly, and the current waveform is a pulse current waveform synchronized with the wire feed waveform's phase. As shown in Fig. 2(a) to (b), by forming droplets at the wire tip while advancing the wire, the droplets are accelerated in the direction of the molten pool. Consequently, as shown in Fig. 2(c), even after reversing the wire feed direction, the droplets at the wire tip attempt to move in the molten pool direction due to inertia. As a result, necking occurs at the top of the droplet (Fig. 2(d)), allowing the droplet to detach (free transfer) even without a short circuit (Fig. 2(e)). It should be noted that if the current is in a low current state, or the base current, at the time of droplet detachment, the generation of small particle spatter immediately after the droplet detachment is suppressed. Normally, in the high current range of CO<sub>2</sub> arc welding, a repulsion transfer mode occurs due to the upward force of the arc on the lower part of the droplet, leading to the generation of a significant amount of large-sized spatter. In contrast, the present process effectively utilizes inertia for the droplet detachment, and thus the detachment direction does not deviate greatly

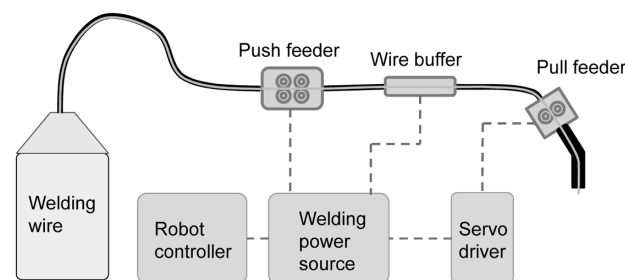


Fig. 1 Schematic diagram of the experimental system

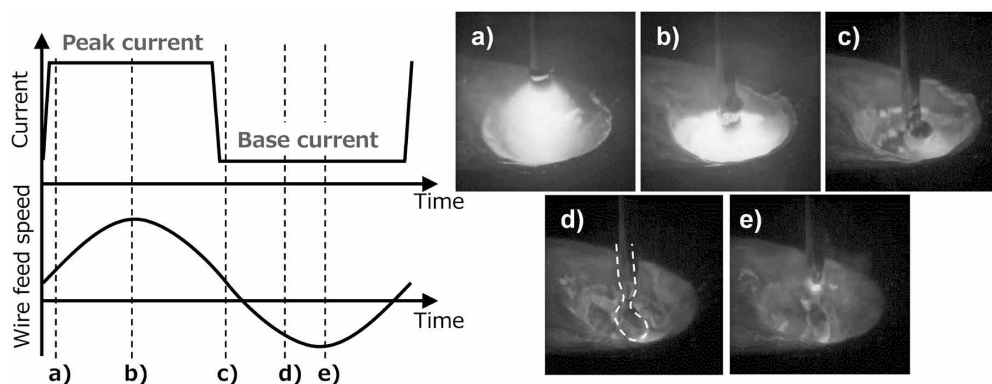


Fig. 2 Droplet transfer phenomenon using inertia

from the wire feed direction. Therefore, a regular droplet transfer synchronized with the wire feed speed waveform is achieved across a wide range of conditions, from low current to high current, with very little occurrence of large-sized spatter.

#### 1.4 Effect of droplet size and the maximum wire feed speed at wire tip on AXELARC™ droplet transfer phenomenon

In order to achieve stable droplet transfer in AXELARC™, various welding parameters related to the welding current waveform and wire feed speed waveform must be optimized. In this study, attention is focused on droplet size and the maximum speed of the wire tip to observe the droplet transfer phenomenon. It should be noted that, in AXELARC™, droplet transfer is based on one droplet detachment per one period of the forward-backward movement of the wire. The droplet size ( $V_{\text{drop}}$ ) is determined using Equation (1):

$$V_{\text{drop}} = Wf_{\text{avg}} \times \frac{\pi d^2}{4} \times \frac{1}{f} \dots\dots\dots (1)$$

wherein,  $Wf_{\text{avg}}$  represents the average wire feed speed,  $d$  is the wire diameter, and  $f$  is the frequency of forward-backward feed.

Additionally, the maximum speed of the wire tip is determined using the highest acceleration rate ( $Wf_{\text{max}}$ ) and is calculated with Equation (2):

$$Wf_{\text{max}} = L_m \times \pi \times f \dots\dots\dots (2)$$

wherein,  $L_m$  stands for the amplitude of wire feeding, and  $f$  is the frequency of the forward and backward feed.

$Wf_{\text{max}}$  represents the speed added to the average wire feed speed when the wire tip reaches its maximum speed.

In the following experiment, the welding current waveform parameters were adjusted within the range of an average wire feed speed of 13 to 19 meters per minute. Specifically, the droplet size and the maximum wire feed speed of the wire tip were changed by manipulating the amplitude and frequency in the wire feeding parameters.

First, the following describes the case where the droplet size is kept constant, and the maximum wire feed speed is varied. Fig. 3 shows the droplet transfer phenomenon at two different maximum wire feed speeds, 90 m/min and 70 m/min, at an average wire feed speed of 19 m/min with a droplet size of 3 mm<sup>3</sup>. In Fig. 3(a), with the maximum wire feed speed at 90 m/min, the droplet transfer phenomenon can achieve free transfer, similar to that shown in Fig. 2. However, as shown in Fig. 3(b), when the maximum wire feed speed is 70 m/min, no necking occurs on the top of the droplet in the steps 3) to 4) in Fig. 3, and in step 5), the droplet does not detach. In AXELARC™, to utilize inertia for droplet transfer, it is necessary to configure wire feeding conditions to secure a predetermined average wire feed speed while setting an appropriate maximum wire feed speed depending on the droplet size.

Next, the following describes the case where the maximum wire feed speed is kept constant, and the droplet size is varied. Fig. 4 shows the droplet transfer phenomenon with droplet sizes of 2 mm<sup>3</sup> and 3 mm<sup>3</sup> at an average wire feed speed of 13 m/min and the maximum wire feed speed of 70 m/min. In Fig. 4(a), with a droplet size of 3 mm<sup>3</sup>, the droplet transfer phenomenon is similar to that shown in Fig. 2. However, in the case where the droplet size is 2 mm<sup>3</sup> as shown in Fig. 4(b), the droplet cannot detach in the steps 3) to 5) in Fig. 4. To realize droplet transfer in AXELARC™, the current waveform and wire feed speed waveform

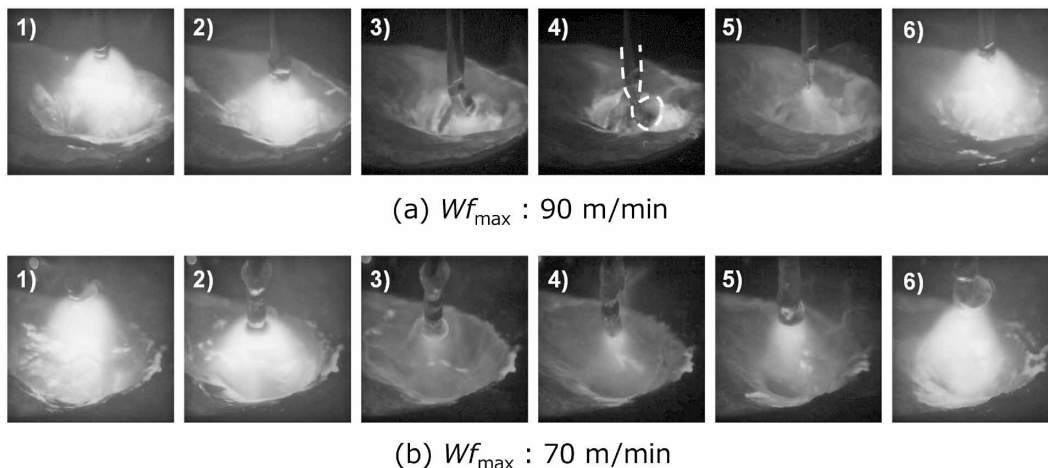
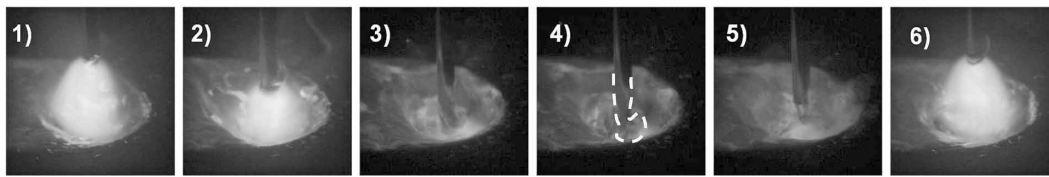
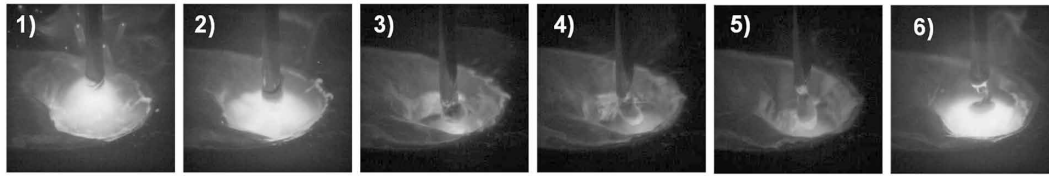


Fig. 3 Effect of maximum wire feed speed on droplet transfer phenomenon ( $Wf_{\text{avg}}$ : 19 m/min,  $V_{\text{drop}}$ : 3 mm<sup>3</sup>)



(a)  $V_{\text{drop}} : 3 \text{ mm}^3$



(b)  $V_{\text{drop}} : 2 \text{ mm}^3$

Fig. 4 Effect of droplet size on droplet transfer phenomenon ( $Wf_{\text{avg}}$ : 13 m/min,  $Wf_{\text{max}}$ : 70 m/min)

parameters must be set such that the droplet size becomes appropriate for the average wire feed speed.

The above experimental results indicate that the key factor determining the success of droplet detachment in AXELARC™ is the ability to accelerate the droplet to form necking on the top of the droplet through inertia. If a droplet reaches only an insufficient speed, the droplet is pulled back along with the wire without forming necking when the wire enters the backward movement. Consequently, in the subsequent wire melting period, the droplet enlarges, resulting in an unstable droplet transfer mode. On the other hand, when the droplet size and the maximum wire feed speed of the wire tip are properly configured, the formed droplet is synchronized with the wire and sufficiently accelerated towards the molten pool. If necking occurs on the top of the droplet due to inertia after the wire enters the backward movement, the droplet can detach during the backward movement. It should be noted that achieving this droplet transfer requires setting the parameters of the current waveform and wire feed speed waveform, and the optimal parameters may vary depending on the wire composition, wire diameter, shielding gas composition, and average wire feed speed.

## 2 Application effects of new wire feed control process, AXELARC™

### 2.1 Reduction in spatter and fume

Comparisons have been made between the conventional CO<sub>2</sub> arc welding process using constant voltage control and AXELARC™. Fig. 5 compares

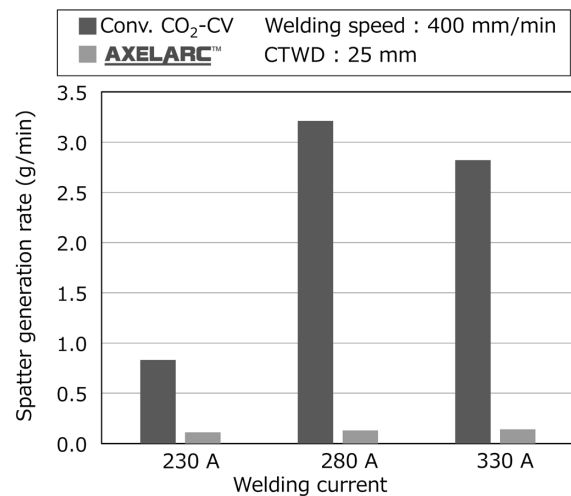


Fig. 5 Comparison of spatter generation rate

the spatter generation rate, and Fig. 6 compares the scattering of spatter during welding. In Fig. 5, the comparison was made on the spatter generation rate when welding at currents ranging from 230 to 330 A, with the wire feed speed and the contact-to-work distance (CTWD) held constant. In the conventional CO<sub>2</sub> arc welding process, a significant portion of the spatter consists of spatter due to arc re-ignition after short circuit and large-sized spatter caused by droplets that rotate themselves and scatter due to repulsion and detachment. On the other hand, in AXELARC™, the droplet transfer process generates minimal short circuits, and thanks to the utilization of inertia, the detachment direction of the droplet remains aligned with the wire feed direction. As a result, the spatter generation rate is significantly reduced even under CO<sub>2</sub> arc welding process gas shield. Compared with the conventional CO<sub>2</sub> arc welding process, the spatter generation rate for AXELARC™ is generally less than 1/10 in a wide



Wire feed rate : 16 m/min  
350 A-37 V-500 mm/min



Wire feed rate : 16 m/min  
310 A-38 V-500 mm/min

Fig. 6 Comparison of spatter scattering

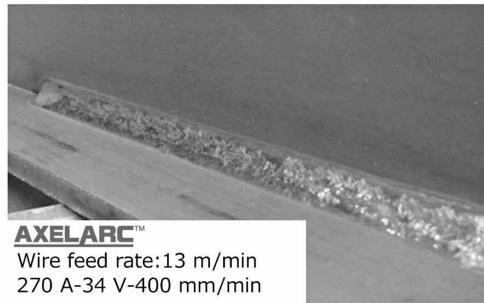
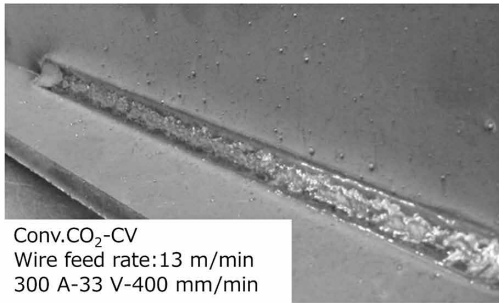


Fig. 7 Comparison of bead appearance in flat fillet welding

range of current conditions from low to high. As shown in Fig. 7, the amount of spatter adhering to the vicinity of the welding bead is also minimal.

Next, the fume emission rates for the conventional CO<sub>2</sub> arc welding process and for AXELARC™ were compared, and the results are shown in Fig. 8. Compared with the conventional CO<sub>2</sub> arc welding process, the fume emission rate for AXELARC™ is consistently lower under various wire feed speed conditions, and especially under high-speed wire feeding (high current) conditions, for which the fume emission rate using AXELARC™ is 40% or less that of the conventional method. Welding fume originates mainly from metal vapor emitted from droplet surfaces overheated by the arc. It diffuses through the repeated contraction and expansion of the surrounding gas during short circuits and re-arcing.<sup>8)</sup> The reduction in fume emission with AXELARC™ is attributed to the minimal occurrence of short circuits and the reduced heating time of the droplet thanks to the shorter droplet transfer period.

## 2.2 Melting characteristics of wires

Fig. 9 shows the relationship between the welding current and wire melting rate for the conventional CO<sub>2</sub> arc welding process and AXELARC™. The wire melting rate with AXELARC™ is approximately 15-20% higher for the same average current. Therefore, under the same average current conditions, an increase in deposition

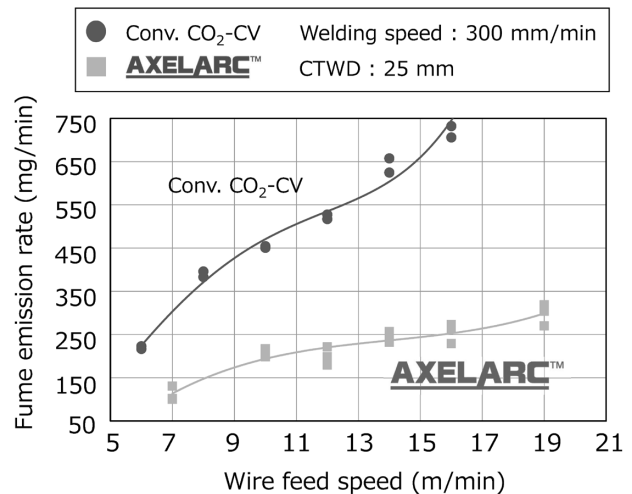


Fig. 8 Comparison of fume emission rate

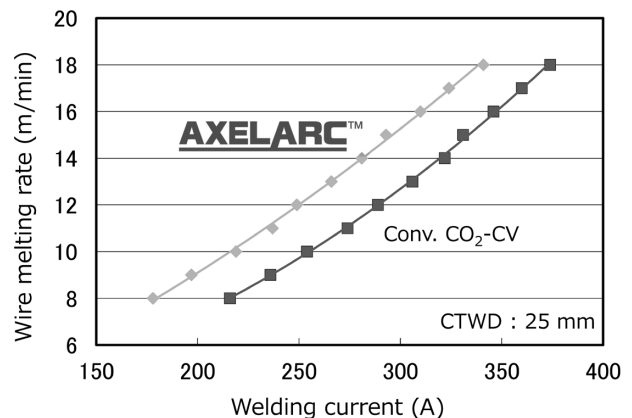


Fig. 9 Comparison of wire melting rate

is expected, which leads to improved welding efficiency. This difference is believed to be primarily the result of the pulse current used in AXELARC™, resulting in a higher Joule heating rate in the wire extension part, unlike the conventional CO<sub>2</sub> arc welding process, which experiences relatively small current variations.

### 2.3 Deep penetration performance

Fig.10 shows the penetration depths for various welding processes when bead-on-plate welding is performed by varying the welding speed, using a common wire feed speed of 16 m/min and a contact-to-work distance of 25 mm. AXELARC™ exhibits deeper penetration compared with conventional short-circuit wire feed control processes and pulsed MAG welding process, achieving penetration depths equivalent to those of the conventional CO<sub>2</sub> arc welding process. Fig.11 shows the penetration depth in flat fillet welding. In a wide range of wire feed speed conditions, AXELARC™ exhibits deeper penetration, achieving depths equivalent to or greater than those of the conventional CO<sub>2</sub> arc welding process. In addition, it advantageously yields a flatter bead shape compared with conventional short-circuit wire feed control processes. Fig.12 compares penetration shapes in flat fillet welding by various welding processes. AXELARC™ exhibits a flat bead shape even at a wire feed speed of 7 m/min, which is in contrast to the conventional CO<sub>2</sub> arc welding process. This improvement in bead shape is attributed to AXELARC™'s ability to minimize short circuit occurrences and promote free droplet transfer, while

conventional CO<sub>2</sub> arc welding is based on short-circuit transfer. The above experiments indicate the possibility that AXELARC™ will improve defect tolerance and has the potential to contribute to the

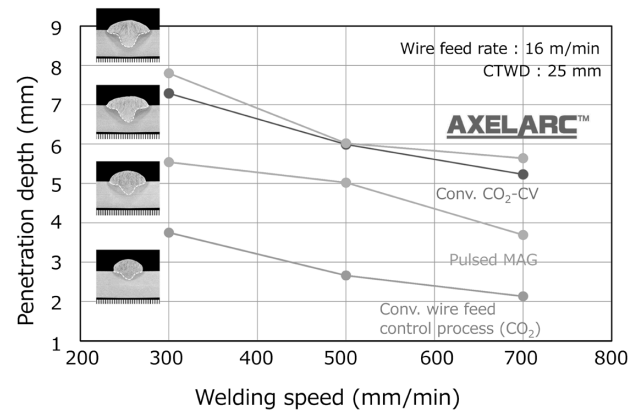


Fig.10 Comparison of penetration depth in Bead-on-plate welding

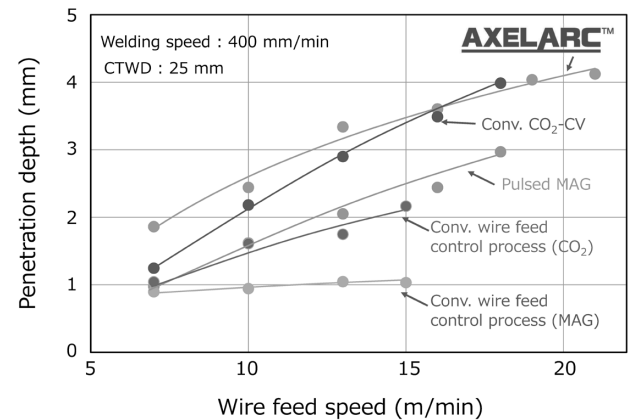


Fig.11 Comparison of penetration depth in flat fillet welding

Wire feed rate	7 m/min	13 m/min	16 m/min	21 m/min
Conv. wire feed control process (MAG)				
Conv. wire feed control process (CO <sub>2</sub> )				
Pulsed MAG				
Conv. CO <sub>2</sub> -CV				
<b>AXELARC™</b>				

Fig.12 Comparison of cross-sectional profile in flat fillet welding (CTWD: 25 mm, Welding speed: 400 mm/min)

high-quality welding of medium to thick plates.

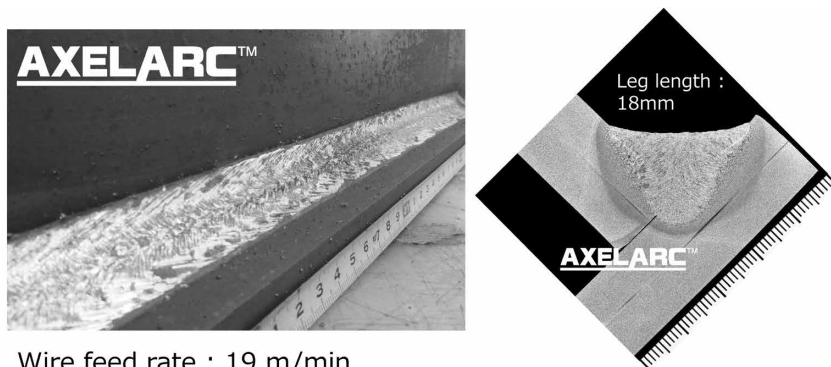
## 2.4 Improved welding efficiency for medium-to-thick plates

Fig.13 shows examples of welding conditions, bead appearance, and macroscopic cross-sectional photos in flat fillet welding. AXELARC™ increases the deposition rate compared with pulsed MAG welding, allowing for an approximately 20% faster welding speed while maintaining an equivalent leg length. It also results in a pronounced, deep penetration with a bowl-shaped appearance. In flat fillet welding, conventional pulsed MAG welding requires 3-4 passes to achieve a leg length of 18

mm, whereas AXELARC™ achieves the same leg length in a single pass, as shown in Fig.14. This fact demonstrates the potential of AXELARC™ for higher speed and a greater deposition rate in flat fillet welding. Fig.15 shows examples of horizontal fillet welding by pulsed MAG welding and AXELARC™, aiming at a leg length of 9 mm. AXELARC™ allows for an approximately 30% faster welding speed, while achieving an excellent bead appearance and a deep penetration shape. This feature is distinct from pulsed MAG welding, which exhibits small undercut on the vertical plate side. Thus, AXELARC™ contributes to improved quality and efficiency in welding medium-to-thick plates.

Process / Bead appearance	Leg length (mm)	Welding current (A)	Welding speed (mm/min)	Cross section
	8	380	420	
	10	380	300	
	14	380	1st 420 2nd 260	
	8	390	500	
	10	390	360	
	14	390	1st 500 2nd 310	

Fig.13 Welding conditions and results for flat fillet joint



Wire feed rate : 19 m/min  
380 A-43 V-150 mm/min

Fig.14 Bead appearance and cross-sectional profile in flat fillet welding with a large leg length

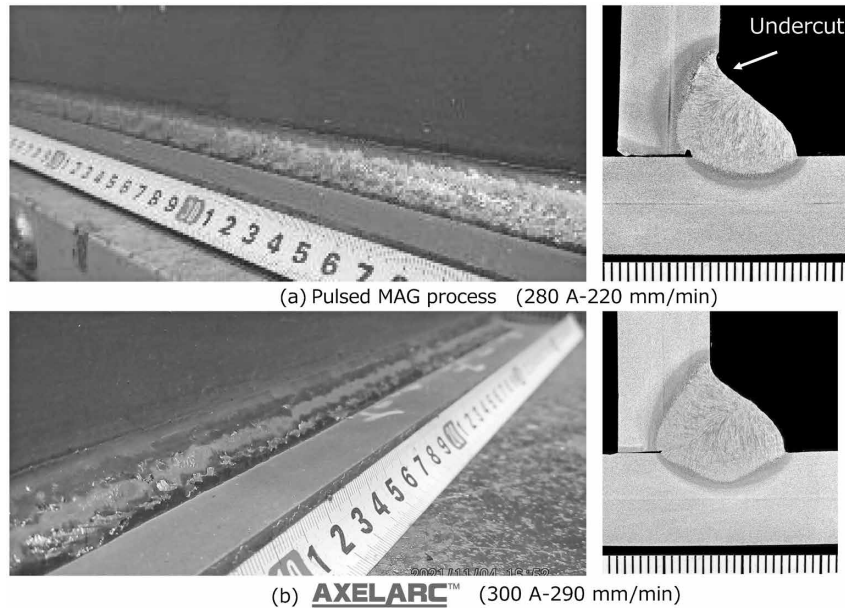


Fig.15 Bead appearance and cross-sectional profile in horizontal fillet welding aiming for a 9 mm leg length

## Conclusions

Kobe Steel has developed a new wire feed control process, AXELARC™, which utilizes droplet acceleration and the formation of necking as a result of inertia, eliminating the need for short-circuit transfer. This process enables low-spatter and low-fume welding over a wide range of current conditions while maintaining deep penetration, allowing for high deposition rates and increased welding speed. As a result, AXELARC™ is poised to significantly contribute to improving the quality and efficiency of welding in the medium-to-thick plate field. Kobe Steel will strive to utilize AXELARC™ and aim to create new welding solutions that go beyond the constraints of wire types, shielding gas compositions, and welding condition ranges that have been inherently limiting in conventional welding processes.

## References

- 1) T. Ogasawara et al. R&D Kobe Steel Engineering Reports. 1985, Vol.35, No.3, pp.22-26.
- 2) A. Matsunawa et al. Journal of the Japan Welding Society (Journal of JWS). 1984, Vol.53, No.6, pp.284-322.
- 3) G. Huisman. Proc International Conference on 'Advances in welding technology 2000', Orland, FL, USA, 2000 12-06/08, The American Welding Society, 2000, pp.165-172.
- 4) K. Himmelbauer. The CMT-Process - A revolution in welding technology. IIW Doc. XII-1875-05. 2005.
- 5) S. Eggarland. Improving Welding-Quality and Reducing Costs by Using the CMT-Welding Process under Pure CO<sub>2</sub>-Shielding Gas. IIW Doc. XII-1993-07. 2007.
- 6) J. Fujiwara. Welding Technology. 2011, Vol.59, No.2, pp.51-56.
- 7) T. Era. Journal of the Japan Welding Society (Journal of JWS). 2015, Vol.84, No.4, pp.234-238.
- 8) T. Suga et al. Quarterly Journal of the Japan Welding Society. 1984, Vol.2, No.2, pp.638-645.

# Welding Machine “SENSARC™ RA500” with Highly Efficient Welding Processes

Shogo NAKATSUKASA\*1 • Akira OGAWA\*1 • Eiji SATO\*1 • Bainsi JO\*1 • Shota SEKIGUCHI\*1

\*1 Technical Center, Welding Business

## Abstract

*SENSARC™ RA500 is an arc-welding machine newly developed with highly efficient processes. It was launched in the summer of 2021 as a higher-end model encompassing the current SENSARC™ AB500. This high-end welding machine is equipped with highly efficient processes and functions suitable for automated welding of medium-to-thick plates for, for example, architectural steel frames, construction machinery, bridges, and vehicles, which are Kobe Steel’s specialty. This paper introduces the highly efficient welding methods realized by SENSARC™ RA500, including pulsed MAG welding with expanded efficiency, REGARC™ with even lower spatter, and tandem welding specialized for high-speed welding.*

## Introduction

In the realm of large welding structures, like architectural steel frames and construction machinery, which entail thick plates and canning by multi-layered welding, the demand for enhanced efficiency is unceasing due to the substantial welding volume and prolonged welding processes. Conversely, in industries primarily dealing with thinner plates and single-pass fillet welding, there is a pressing need for improved efficiency through heightened welding speeds. However, achieving heightened efficiency in high-speed welding presents challenges in preserving welding quality, including addressing welding defects, bead appearance degradation, and increased spatter generation, among other issues. To resolve these

challenges, Kobe Steel offers a comprehensive solution leveraging its own products, encompassing welding materials, welding robots, and welding machines.

This paper introduces a new cutting-edge welding machine, SENSARC™<sup>Note 1)</sup> RA500 (hereafter referred to as “RA500”) (Fig. 1). The RA500 comes equipped with a range of high deposition welding processes and plays a pivotal role in the welding robot system, making a valuable contribution to overcoming various challenges.

## 1. Features of RA500

Since the early 1980s, Kobe Steel’s arc-welding robots have found widespread adoption among customers, both in Japan and other countries, primarily in the medium-thick plate sector. The key requirements for welding systems in this field include: i) improving efficiency (shortening cycle times and increasing operation rates), ii) achieving high-quality welding work, and iii) expanding automation. Improving efficiency is often associated with the “arc time,” which makes up 70-80% of the robot’s operational duration. To reduce the arc time, it is essential to increase the welding speed. Achieving this necessitates a welding power source with an expanded upper limit of welding current output and appropriately controlled welding current waveforms.

### 1.1 Welding power source

Table 1 presents a comparison of exemplary specifications between the newly developed welding power source, RA500, and the conventional model, SENSARC™ AB500. Regarding the basic performance, the RA500 has made substantial improvements through revisions to the power circuit and housing design, resulting in a significant expansion of its 100% usage rate. For the DC constant voltage welding method, the rated output has been increased from 450 A to 500 A, and for the DC pulse welding method, it has gone from 400 A to 450 A. This expansion allows for improved efficiency



Fig. 1 Outside viewing of welding power source SENSARC™ RA500

Note 1) SENSARC is a registered trademark (TM) of Kobe Steel.

Table 1 Comparison of specifications between developed power source and conventional power source

	RA500	AB500
Rated output	100%-500 A DC-CV 100%-450 A PULSE 60%-500 A PULSE	90%-500 A DC-CV 100%-400 A PULSE 40%-500 A PULSE
Physical dimensions	W386×D629×H810(mm) 71(kg)	W370×D663×H685(mm) 69(kg)
Temperature range	Operation -10°C to 40°C	Operation -10°C to 40°C
Controller	Control cycle : 12.5 μs Sampling cycle : 2 MHz	Control cycle : 50 μs Sampling cycle : 40 KHz
Connectable device	Welding robot Welding carriage	Welding robot
Industrial network	EtherCAT Ethernet/IP	CANopen

in the high-current range. Furthermore, as explained in more detail below, it has adopted new output control for the extended high current range of DC pulse, enabling both high efficiency and high-quality welding.

The control section of the power circuit has enhanced output control with an increased control period of 12.5 μs (four times longer than the conventional model) and raised feedback sampling frequency of 2 MHz (a 50-fold increase compared with the conventional model). These enhancements have enabled more precise control of arc length and droplet transfer, making it easier to customize welding for different materials and work needs.

Although the external dimensions of the welding power source have increased in height by 125 mm when compared with the conventional AB500 model, the ground contact area ratio has remained at a similar level. To enhance dust resistance, the heating part of the power circuit, the electronic circuit control section, and the cooling part are configured in complete isolation (Fig. 2). A side-flow structure is employed for forced air cooling, drawing air in from the sides and expelling it from the front and rear, thereby improving the cooling efficiency. For instance, while the conventional model requires a 300 mm clearance from surrounding obstructions, the RA500 can satisfy the usage rate with only a 50 mm clearance under specific conditions. Additionally, in terms of maintenance, the structure allows cleaning of the heat sink from the front panel. This facilitates cleaning without moving the welding power source from the robot system (Fig. 3).

## 1.2 Wire feeder

The wire feeder is designed with a full-cover structure to safeguard it against unintentional contact with the welding circuit. (Fig. 4). Furthermore, the dust resistance of the feeding

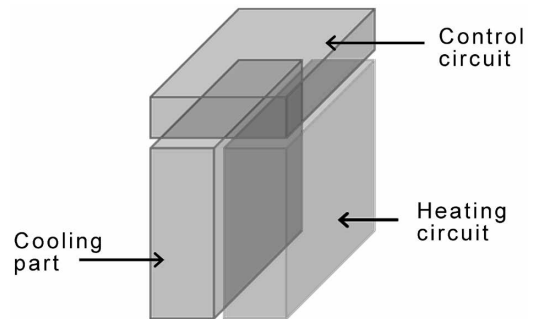


Fig. 2 Layout inside the welding power source



Fig. 3 Side flow structure

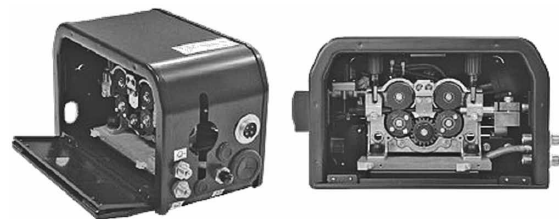


Fig. 4 Outside view of wire feeder

motor has been enhanced, achieving an IP53 protection rating. The feeder has undergone significant performance enhancements, including a 13% increase in the rated load torque and a durability boosted to 1.5 times that of the previous model (with a load of 1.5 Nm and a feeding speed of 22 mpm). Thus, this feeder seamlessly integrates safety, dust resistance, and durability, guaranteeing

robust performance for enduring extended periods of continuous welding, while achieving a maximum feeding speed of up to 30 mpm.

## 2. Welding process

### 2.1 Standard welding mode

The arc-welding machine comes equipped with specialized welding modes designed to suit a variety of materials, with a primary emphasis on general-purpose welding materials for mild steel (Table 2). The RA500 differentiates between rutile-based wires and metal-based wires, offering dedicated flux-cored wire welding modes for each, with the goal of improving welding quality through precise output control. If necessary, it is also possible to expand and integrate welding modes for materials other than mild steel.

Table 2 Built-in welding mode

Welding method	GAS	Wire materials	Wire diameter (mm)
DC-CV	CO <sub>2</sub>	MILD STEEL(SOLID)	1.2, 1.4, 1.6
		MILD STEEL(Rutile-FCW)	1.2, 1.4,
		MILD STEEL(Metal-FCW)	1.2, 1.4,
		STAINLESS(FCW)	1.2
	Ar+CO <sub>2</sub>	MILD STEEL(SOLID)	1.2
PULSE	Ar+CO <sub>2</sub>	MILD STEEL(SOLID)	1.2, 1.4

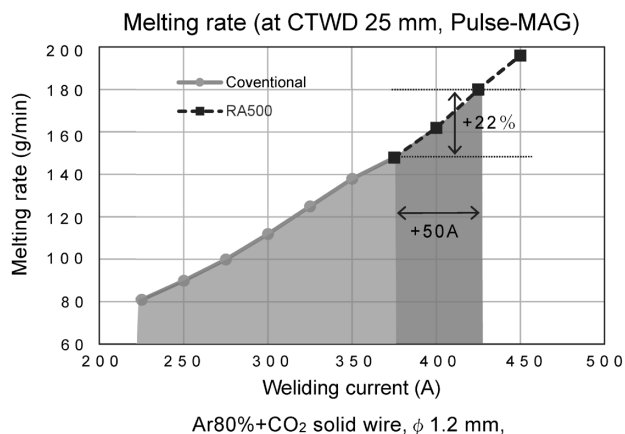


Fig. 5 Relationship between welding-current and wire melting rate

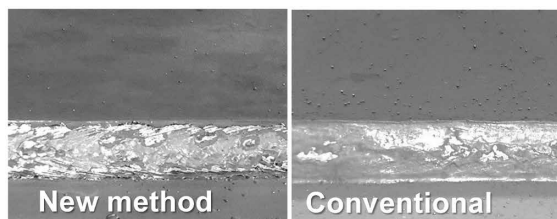


Fig. 6 Adhesive spatter reduced by new method

With the expansion of the 100% usage rate, high efficiency is achieved for DC pulse welding, with current conditions exceeding 400 A. Fig. 5 shows an example of the efficiency improvement for a solid wire with a diameter of  $\phi$  1.2 mm. RA500 has a maximum wire melting rate increased by approximately 20% from the previous 150 g/min to 185 g/min, enabling highly efficient welding work. It should be noted that the 100% usage rate for DC pulse welding is 450 A; however, considering the burden on consumables in the feeding system due to the increased feeding speed of  $\phi$  1.2 mm wire and the stability of molten metal, the upper limit for welding current is estimated to be around 430 A. In general, under welding conditions exceeding 400 A, minor spatter adhesion is observed even in pulse welding. However, RA500 employs optimal pulse output control for this range, significantly reducing such adhesive spatter (Fig. 6).

As a specific example of efficiency improvement, the calculated arc time for a 16 mm thick, 50° V-groove butt welding is shown in Fig. 7. In this example, the first layer ensures fusion, the finishing layer emphasizes appearance, and the maximum melting speed is applied primarily to the intermediate layer. Even in this example, where the intermediate layer has the smallest proportion, there is an expected reduction of approximately 13% in arc time compared with AB500.

### 2.2 New pulse control

In RA500, a new pulse control has been adopted for the DC pulse mode for solid wire, enabling stable pulsed arc welding across a wide current range, from low to high currents. This new pulse control is particularly effective in pulsed MAG welding with a  $\phi$  1.4 mm wire. In conventional pulse control, arc length control was performed by base-time modulation (Fig. 8), whereas the RA500's arc length control employs peak-current modulation (Fig. 9) in the high current range. Specifically, base-time

	Pass	Welding current [A]	Welding travel [mm/min]	Wire feed rate [m/min]	Melting rate [g/min]	ARC time [min/m]
RA500	1	280	280	12	105	10.6 <b>13%Up</b>
	2	430	290	22	190	
	3	400	290	20	173	
AB500	1	280	250	12	104	12.0
	2	380	250	18	154	
	3	380	250	18	154	

80%Ar+CO<sub>2</sub> DC-PULSE  
 $\phi$  1.2 mm, YGW15  
 CTWD: 25 mm



T: 16 mm  
 V: 50°  
 GAP: 5 mm

Fig. 7 Comparative examples of efficiency of butt welding

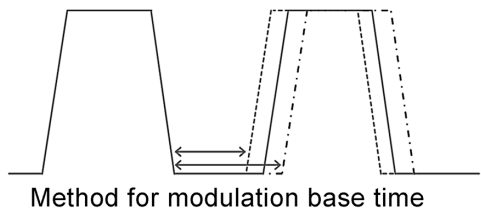


Fig. 8 Conventional method (modulating base-time)

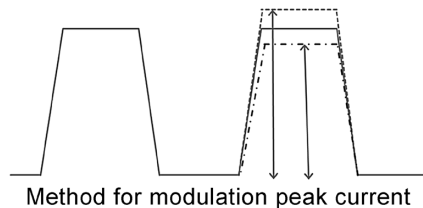


Fig. 9 New method (modulating peak-current)

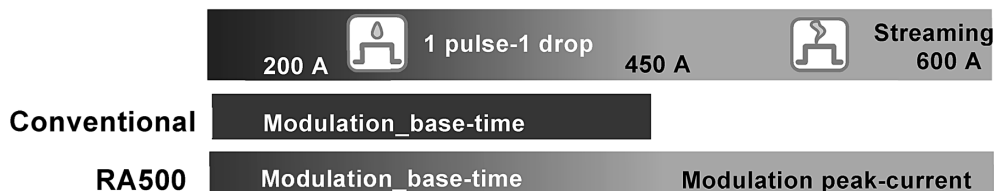
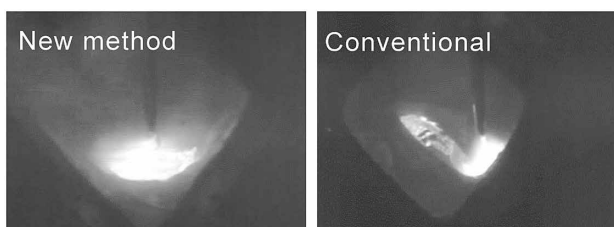
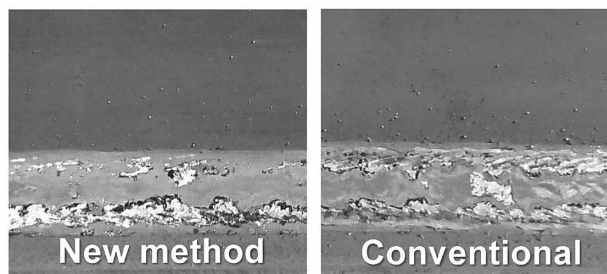


Fig.10 Application image of new pulse control



Welding current: 600 A, Wire feed rate: 24 ppm  
Solid wire (YGW11)  $\phi$  1.4 mm, CTWD: 30 mm

Fig.11 Comparison between new pulse control method and conventional pulse control method



Pulse-MAG, WFR: 20 ppm, CTWD: 30 mm  
Travel: 350 mm/min, Solid wire:  $\phi$  1.4 mm, Conditions:550 A

Fig.12 Appearance of welding bead

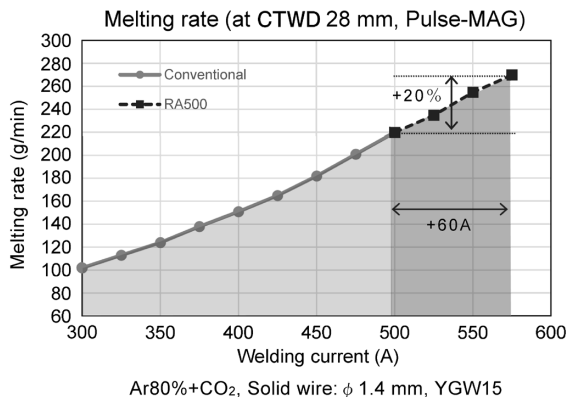


Fig.13 Welding current and wire melting rate

	Pass	Welding current [A]	Welding travel [mm/min]	Wire feed rate [m/min]	Melting rate [g/min]	ARC time [min/m]
RA500	1	280	350	9	109	8.6
	2	560	350	22	260	
	3	450	350	16	189	
AB500	1	280	350	9	109	9.8
	2	500	290	18	213	
	3	450	285	15	177	

80%Ar+CO<sub>2</sub>, DC-PULSE  
 $\phi$  1.4 mm, YGW15  
CTWD: 28 mm



Fig.14 Efficiency comparison example of butt welding

modulation control is applied for currents of 450-500 A or lower, and peak-current modulation control is applied for those of 500 A or higher (Fig.10). This effectively suppresses the vibration of the molten pool in high-current welding exceeding 500 A (Fig.11), which was a previous challenge, and enables the creation of beads with well-defined toes. This also reduces spatter adhesion to the base metal (Fig.12). However, in the high current range, droplet transfer may sometimes become a rotating transfer, and pore defects originating from the atmosphere are likely to occur due to turbulence in the shielding gas. Therefore, careful attention is required.

The recommended upper limit for the proper

welding current in this new pulse control process is approximately 560 A (with a wire diameter of  $\phi$  1.4 mm, in parallel configuration). At this current, the wire melting rate is around 260 g/min. This is about 20% higher than that of AB500, whose limit for stable bead formation is at around 500 A. Further increasing the output is possible, but it can make controlling the molten pool more challenging, as the molten metal may flow ahead, making it not advisable. The relationship between the melting speed and output current is shown in Fig.13.

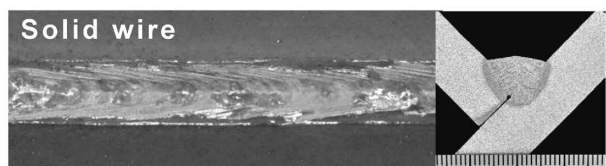
As a specific example, the calculated arc time for welding a 16 mm thick, 50° V-groove butt joint is shown in Fig.14, where an approximately 14%

reduction in arc time is expected, compared with AB500.

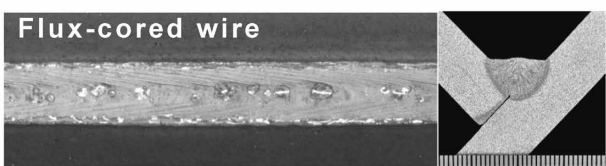
### 2.3 Tandem MAG pulse

Tandem MAG pulse welding is one of Kobe Steel's longest-standing high-efficiency welding methods and has continued to evolve alongside the development and improvements of welding machines. In the tandem mode of AB500, the tailing electrode pulses in sync with the leading electrode to achieve arc stability equivalent to single electrode welding, despite its double electrode configuration. In contrast, RA500 has reevaluated the control of the tailing electrode to further enhance the arc stability. It should be noted that the RA500 tandem welding system was launched in June 2022.

The tandem mode of RA500 includes a tandem welding mode for flux-cored wires in addition to the mode for solid wires. Tandem welding divides the electrode into two electrodes, offering superior welding speed compared with single electrode welding with the same melting speed. However, further increasing the speed can lead to challenges such as a convex bead shapes and destabilization of the molten pool due to increased deposition amounts. On the other hand, using flux-cored wires results in stable streaming transfer without interference between the electrodes even in the high current range of 400 A or higher, thanks to the effect of flux columns, which is characteristic of the droplet transfer of these wires. This action suppresses the movement of the molten pool, enabling the formation of flat beads even in high-speed welding with a leg length of 8 mm and a welding speed of 1,000 mm/min (Fig.15). High deposition applications are also possible. The use of a low-slag flux-cored wire with a diameter of  $\phi$  1.3 mm, under the conditions of a leading electrode



Tandem-Pulse-MAG, Travel: 800 mm/min  
CTWD 25 mm, Lead: 400 A-32 V, Trail: 360 A-33 V  
Leg length: 8.6 mm



Tandem-Dccv-MAG, Travel: 1,000 mm/min  
CTWD: 25 mm, Lead: 400 A-31 V, Trail: 360 A-37 V  
Leg length: 8.1 mm

Fig.15 Example of tandem welding method

at 430 A and a tailing electrode at 400 A, enables a deposition amount of approximately 350 g/min. This is the highest deposition amount in the welding methods hitherto proposed by Kobe Steel (Fig.16).

Another advantage of using flux-cored wire is as follows: In tandem welding where solid wire is generally used, the DC pulse welding method is typically employed. In the tandem welding mode using flux-cored wire, the application of the constant voltage direct current welding method is possible, thanks to the action of the flux columns. This makes the setting of welding conditions easier than in the case of the DC pulse welding method. Furthermore, the application of the DC pulse welding method is not mandatory, making it less prone to the destabilization of power supply due to tip wear (Table 3).

### 2.4 New REGARC™ Note 2)

The common practice in steel frame welding is to use the relatively inexpensive carbon dioxide gas as a shielding gas, and, therefore, welding is mainly performed at high currents to enhance efficiency. Especially within the high current range, there has been a long-standing challenge of increased spatter generation due to the irregular globular transfer of droplets. To address this challenge, Kobe Steel has developed the REGARC™ welding process. In

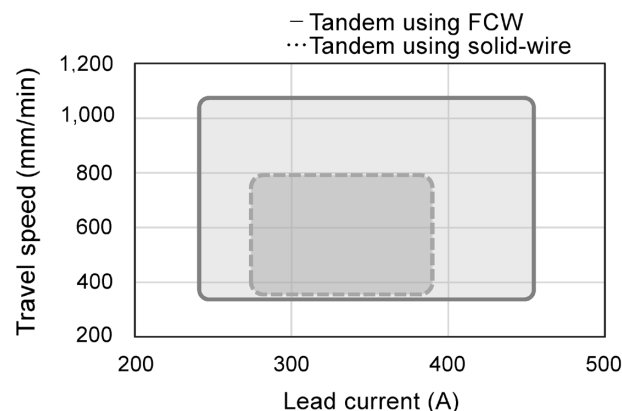


Fig.16 Applicable range of tandem welding method using FCW

Table 3 Advantages of flux-cored wire

	Solid wire	Flux-cored wire
Welding method	Pulse	DC-CV
Bead appearance	Average	good
Tip durability	Average	good
High speed welding	Average	good
Versatile	Average	good

Note 2) REGARC is a registered trademark (TM) of Kobe Steel.

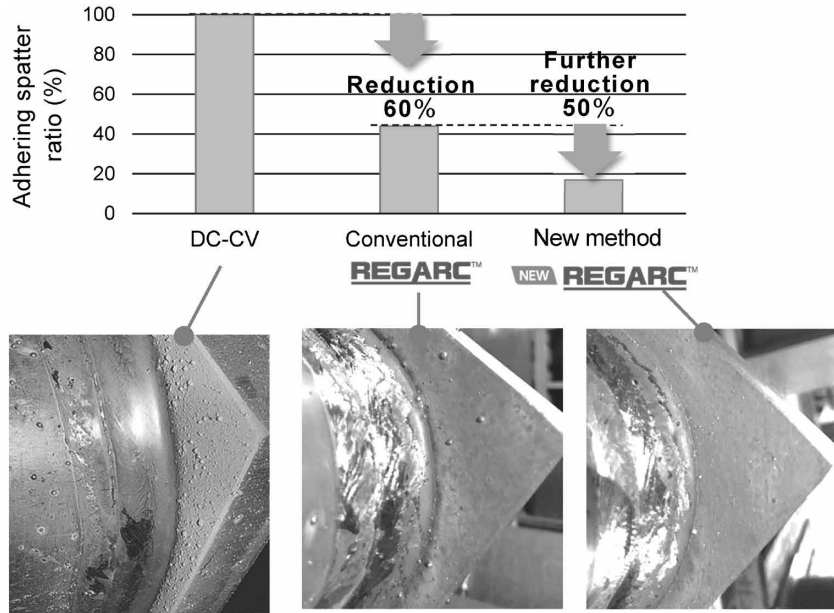


Fig.17 Reduced adhesive spatter amount in new REGARC™

carbon dioxide arc welding, this method involves shaping the welding current into a special pulse waveform at specific times during the droplet formation and detachment processes, thereby suppressing the upward movement of droplets. This allows the droplets to be transferred to the molten pool in an orderly manner before they grow large. This welding method effectively reduces the occurrence of short circuits and the generation of large-sized spatter, and its applications are rapidly expanding.<sup>1)</sup>

RA500 comprises a newly developed output control that enhances the output waveform and arc-length control of the conventional REGARC™ welding process, achieving further reduction of spatter (Fig. 17).

### 3. Application

#### 3.1 Robot function

RA500 serves as a welding machine within Kobe Steel's robot welding systems, featuring an information gathering function when combined with a robot. It includes applications useful for welding machine maintenance, such as recording operating time, welding duration, various alarms, and monitoring parameters like welding current and wire feed speed load (Table 4).

#### 3.2 Digital interface

In terms of digital interfaces, RA500 utilizes EtherCAT for digital connection with Kobe Steel's

Table 4 Combination function with robot

Maintenance information	<ul style="list-style-type: none"> <li>• Welding operation time</li> <li>• Temperature inside the welding power source</li> <li>• Rotation error of cooling fan</li> <li>• Fine-adjustment of welding ball removal control</li> <li>• Motor overcurrent warning detection level</li> <li>• Voltage detection error sensitivity adjustment</li> </ul>
Welding information	<ul style="list-style-type: none"> <li>• Wire-feed load monitor</li> <li>• Welding current monitor</li> <li>• Welding voltage monitor</li> </ul>

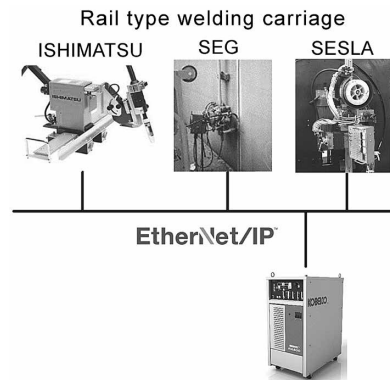


Fig.18 Cooperation with rail-type welding carriage

multi-articulated robot ARCMAN™<sup>Note 3)</sup>. It is also designed to be adaptable to various protocols for digital connection with small and portable robots. For example, plans are in place to establish system integration using EtherNet/IP™ for digital connection with Kobe Steel's ISHIMATSU controller (Fig. 18).

Note 3) ARCMAN is a registered trademark (TM) of Kobe Steel.

Furthermore, RA500 is equipped with Anybus® CompactCom, enabling the development of various digital communication protocols (a total of 11 protocols including Modbus, DeviceNet) tailored to other automation apparatuses. There are plans to gradually expand the range of protocols that can be used for digital communication interfaces.

Leveraging this digital communication interface and the robot functions described in the previous section, RA500 incorporates welding condition instructions for automation equipment connections, such as arc start and crater handling. Additionally, considerations are being made for functions like recording and monitoring welding information that cannot be executed by various automation equipment alone. In the future, there may also be functions that allow for reviewing work records specific to welding portions.

## Conclusions

This paper has introduced the newly developed high-end welding machine, SENSARC™ RA500. Alongside the welding processes and functions introduced in this paper, the ongoing development of new welding processes will continue. Plans are in place to incorporate AXELARC™<sup>Note 4)</sup>, a non-short-circuit-type wire feeding control method for carbon dioxide gas processes, into RA500, with the aim of commercialization in the fiscal year 2024 and beyond. Kobe Steel will strive to contribute to solving problems so as to improve welding quality and efficiency together with welding materials and welding equipment while expanding other functions.

## References

- 1) K. Yamazaki et al. Abstracts of the Welding Society National Conference. April 20-22, 2010, Welding Society, 2010, pp.138-139.
- 2) Y. Kitamura et al. Abstracts of the Welding Society National Conference. September 8-10, 2022, Welding Society, 2022, pp.282-283.

---

<sup>Note 4)</sup> AXELARC is a registered trademark (TM) of Kobe Steel.

# Digital Transformation (DX) Technology to Promote Adoption of Welding Robot Systems

Atsushi FUKUNAGA\*<sup>1</sup> · Kazuki HIDAKA\*<sup>1</sup> · Takaya HIGASHIRA\*<sup>1</sup> · Fumiaki SAWAKAWA\*<sup>1</sup> · Kohei MATSUSHIMA\*<sup>2</sup> · Kohei KOMUKAI\*<sup>1</sup>

\*<sup>1</sup> Welding System Department, Technical Center, Welding Business

\*<sup>2</sup> Welding System Department, Technical Center, Welding Business (currently Technical Center, Welding Business)

## Abstract

*The rapid development of information and communication technologies, as well as the widespread use of AI technologies, is expected to accelerate automation and labor-saving measures in production sites. Kobe Steel has been developing various functions to automate welding operations and increase the ratio of robots used in welding processes. However, the adoption of welding robot systems has resulted in new manual tasks such as teaching and maintenance. By reducing these manual operations, the introduction of welding robot systems can be more effective than ever before, leading to increased productivity. To overcome these challenges, Kobe Steel has leveraged ICT/AI technology to develop an automatic function that generates welding programs, reducing the need for manual teaching work. This feature has been added to the ARCMAN™ Offline Teaching System. A camera has been mounted on the ARCMAN™ PRODUCTION SUPPORT, expanding remote visualization capabilities, which is expected to improve safety by reducing the number of work at elevated areas.*

## Introduction

Kobe Steel has been developing and selling welding robot systems and apparatuses for medium-to-thick plate applications in, for example, construction steel frames, construction machinery, bridges, and shipbuilding, automating the welding process and saving labor. This contribution enhances society's development and improves its customers' production. When welding medium-to-thick plate components, challenges arise due to the large workpieces leading to assembly errors and the tendency for thermal distortion during multi-layer, repeated welding over extended periods. To address these challenges and achieve welding automation, the company has developed technologies such as arc sensors that detect changes in welding current and correct the robot tip position to a pre-taught location. Furthermore, in recent years, Kobe Steel has implemented automation in areas like flare grooves, traditionally performed by skilled welding workers, by measuring root gap with laser sensors and adjusting welding conditions depending on the root gap.<sup>1)</sup>

Thus, the application rate of welding systems has been increased to promote automation. However, introducing welding robot systems has brought about the need for new manual labor, including tasks like teaching work, robot operations, and recovery from short-time breakdowns, which were previously unnecessary in conventional manual welding operations.

To reduce such manual labor, Kobe Steel has provided solutions such as the ARCMAN™ Offline Teaching System to simplify teaching work and ARCMAN™ PRODUCTION SUPPORT, which allows for the visualization of robot production and helps in reducing short-time breakdowns.

This paper introduces functions achieved by adding ICT and AI technology to the software, aiming to reduce teaching work time and improve workability through further visualization of robot production. These functions make welding robot systems easier to use than ever before, promoting the automation of the welding process.

## 1. Teaching-less welding robot system

Before commencing production with a welding robot system, it is necessary to provide instructions for the robot, guiding it on how to weld different parts of the workpiece. This process involves establishing essential welding torch postures to ensure welding quality, avoiding any interference with the workpiece and clamp jigs, configuring sensors to account for potential workpiece misalignment, and defining its overall operation. This task demands a deep understanding of robot operation and welding expertise, especially for intricate workpieces, making it a challenging endeavor not easily undertaken by just anyone.

For more than two decades, Kobe Steel has been steadfast in the development of teaching-less welding systems. In the domain of construction steel frames, bridges, and shipbuilding, teaching-less systems have been successfully integrated, significantly contributing to the automation of welding for many customers<sup>2), 3)</sup> (Fig. 1). A key distinguishing feature of this approach lies not only in providing robot location information tailored to the specific workpiece but also in offering optimal



evaluation. This process aids in selecting the most suitable candidates for welding, culminating in the automatic generation of teaching programs (Fig. 4).

The utilization of this function can significantly reduce the teaching work, which typically takes two days on an actual machine, to just one day. This not only shortens the duration of teaching work, but also may decrease production line downtime. Furthermore, even operators with limited experience

in creating teaching programs can readily generate teaching ones that match those made by seasoned teaching personnel.

### 1.2 Cable simulation function

When teaching programs created offline are tested on the actual machine, there are instances where the welding torch cables attached to the robot

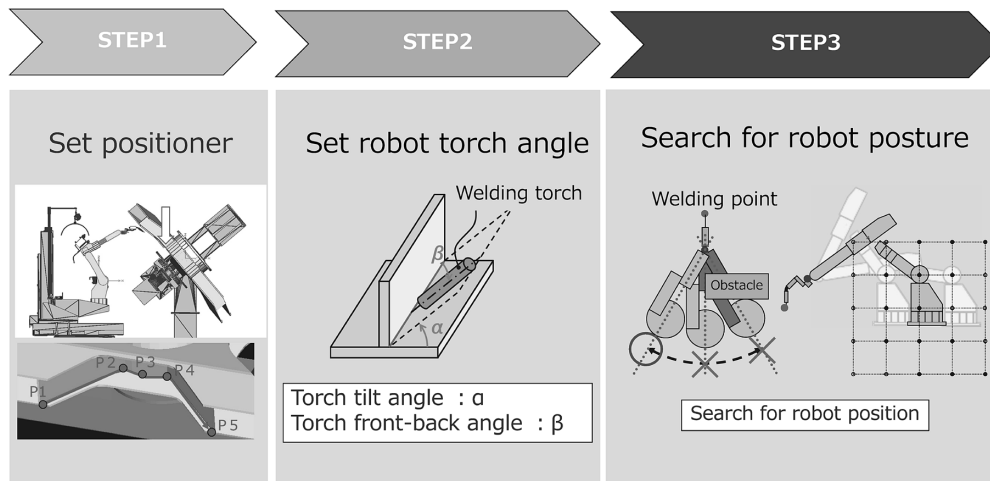


Fig. 3 Flow of robot pose search

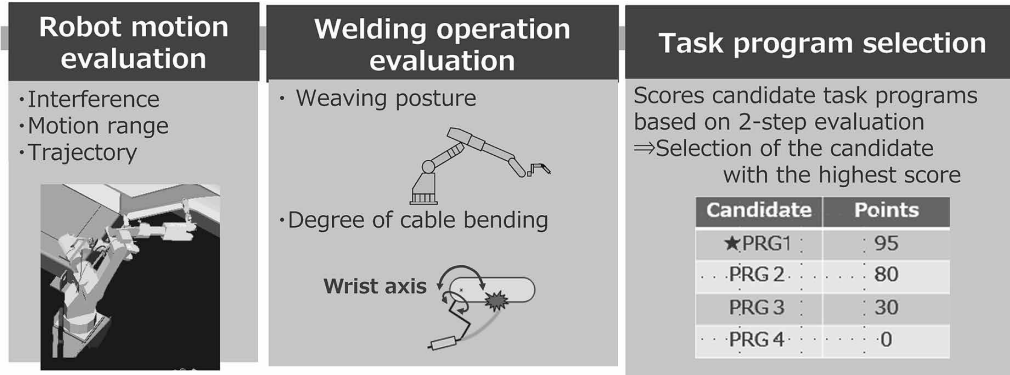


Fig. 4 Automatic selection of work programs on a two-step evaluation

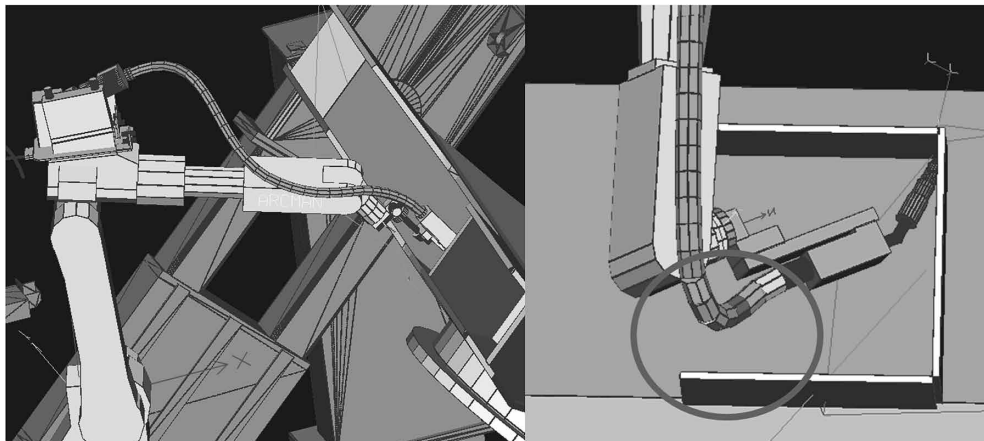


Fig. 5 Cable simulation to check distance between cable and workpiece

interfere, necessitating corrections and re-teaching, which can lead to prolonged teaching sessions. To address this issue, a cable simulation function has been developed, allowing the behavior of the cables to be confirmed offline. Fig. 5 shows how cable simulation is used to check the cable state in narrow areas that are difficult to assess with the naked eye in the actual system. Particularly, as indicated in the right side of Fig. 5, the relationship between the cable and the workpiece position can be easily understood. As a result, teaching programs without cable interference can be created through offline work, shortening the time required for teaching adjustments in the field.

The cable simulation uses geometric curve calculation logic to represent curves that resemble the actual cable's movements. Therefore, it requires fewer calculations to display the cables, compared with using a physical simulation, which requires precise calculation. This enables fast visualization without causing work stress.

The settings for cable movement include only four simple parameters: (1) the starting and ending positions of the cable, (2) the decision whether or not to use a spring balancer, (3) the selection of the torch cable's stiffness, and (4) the direction in which the cable bends. This makes it user-friendly and easy for anyone to use.

## 2. Production visualization system

Kobe Steel provides ARCMAN™ PRODUCTION SUPPORT, a solution designed to aid in the analysis of short-time breakdowns, welding defects, and production management by aggregating operational data from welding robot systems and rendering welding and production data visually<sup>7)</sup>.

This section begins with a discussion of ARCMAN™ View (Section 2.1), which bolsters productivity by linking video information from network cameras with traditional welding and production data. This is followed by the explanation of a work-type determination function (Section 2.2) aimed at preventing erroneous setup due to the robot operator teaching wrong program numbers, through the utilization of images captured prior to production. Additionally, the section introduces the wireless remote monitoring system (Section 2.3), which harnesses mobile computers to enhance work efficiency.

### 2.1 ARCMAN™ View

As an optional feature within ARCMAN™ PRODUCTION SUPPORT, a camera function

named ARCMAN™ View has been developed. This function enables real-time display and recording by connecting network cameras to a PC. Since the size of medium-to-thick plate welding systems tends to increase, ARCMAN™ View incorporates a unique function to control the camera, ensuring that the robot's tip always remains centered in the frame by utilizing the robot tip location information (Fig. 6, Fig. 7).

The videos recorded using ARCMAN™ View can be linked to error information and welding data, facilitating replay covering the time corresponding to specific information. Through this movie-log linkage function, users can readily review the images to verify the welding conditions when errors occur or welding defects manifest, enabling a detailed analysis of the root causes of short-time breakdowns (Fig. 8).

Moreover, ARCMAN™ View's images enable operators to manage the robot while monitoring the screen without the need to approach the robot physically. However, due to the limited depth

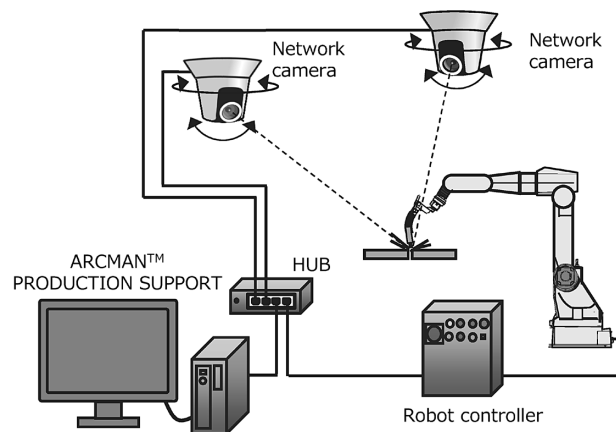


Fig. 6 ARCMAN™ View system configuration

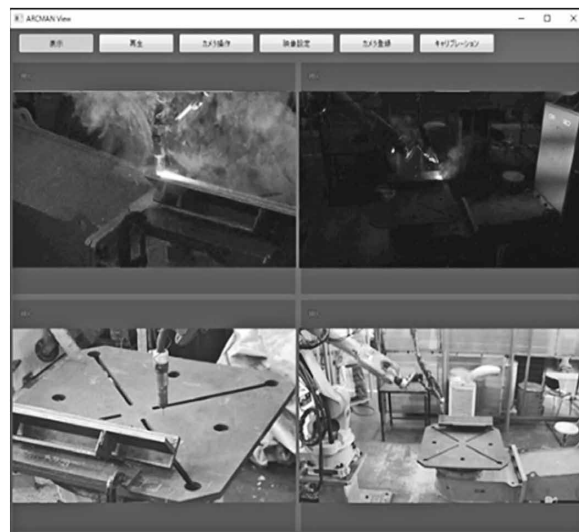


Fig. 7 Sample image of ARCMAN™ View

perception in images, accurately guiding the robot to the welding start position can be challenging. To address this challenge, a touch-sensing function has been devised, allowing the operator to execute it at any chosen time by applying sensing voltage to detect when the wire makes contact with the workpiece. This action triggers the remote sensing function, causing the robot to halt when the wire touches the workpiece (Fig. 9). With the help of this function, robot operation from outside the safety fence becomes feasible, thereby reducing the necessity for work in hazardous locations such as elevated areas.

## 2.2 Work-type determination software

In medium-to-thick plate welding systems, there are scenarios where an operator employs a crane to load a workpiece onto the system and manually selects a teaching program for playback via the teaching pendant or control panel. However, operator errors occasionally lead to the unintentional selection of a different program with similar shapes, resulting in issues like welding in an incorrect position or the torch coming into contact with the

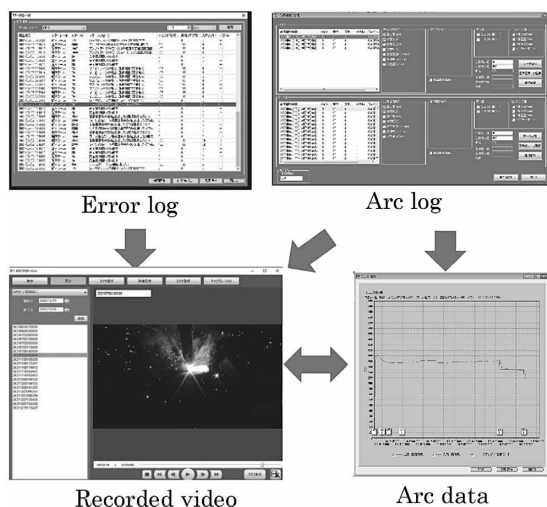


Fig. 8 Concept of log linkage function

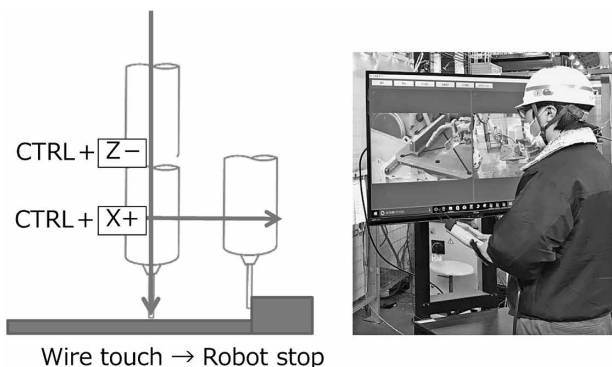


Fig. 9 Concept of sensing remote

workpiece.

One potential solution to this problem involves the utilization of Radio Frequency Identification (RFID). Nonetheless, using RFID for large metal objects like construction machinery necessitates highly precise RFID readers that are less susceptible to radio wave reflections from metal surfaces. This can result in increased initial investment and operational costs.

To tackle this challenge while keeping initial investment and operational costs manageable, Kobe Steel has devised a work-type determination software employing cameras and AI for discrimination. Picture recognition technology, widely explored across various fields, is employed to estimate the types of objects from camera images<sup>5),6)</sup>. However, even when AI recognition accuracy is on par with or exceeds human capability, achieving 100% accuracy presents certain challenges. To address this, a double-checking function involving both humans and AI has been integrated.

When an operator intends to initiate welding, the operator selects the program based on the work type after loading the workpiece and then activates the playback start switch. The developed work-type determination software establishes communication with the robot as soon as the playback start switch is pressed, identifies the program number chosen by the operator, and captures an image of the workpiece using the camera. By analyzing the captured image, the software distinguishes the work type and verifies whether the combination of the determined work type and the operator-selected program number is accurate. If it's an incorrect combination, the software suspends the playback and prompts the operator for confirmation (Fig.10).

In a production environment where the work-type determination software operates, incorporating new workpieces into the system necessitates learning new images of the added work. Traditionally, this process required the expertise of AI developers. To streamline this, a system has been put in place for automatic learning from workpiece images acquired during production. With this system, even in cases with a limited number of initial learning data or low determination accuracy for work types, or when new workpieces are introduced, the software learns and enhances determination accuracy while in operation (Fig.11).

## 2.3 Wireless remote monitoring system

Kobe Steel actively pursues the development of a wireless remote monitoring system, which makes use of mobile devices like tablets, alongside the

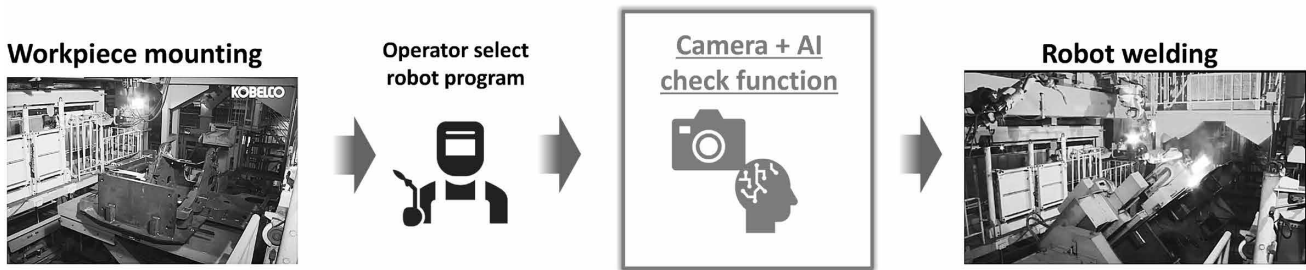


Fig.10 Work type determination software operational flow

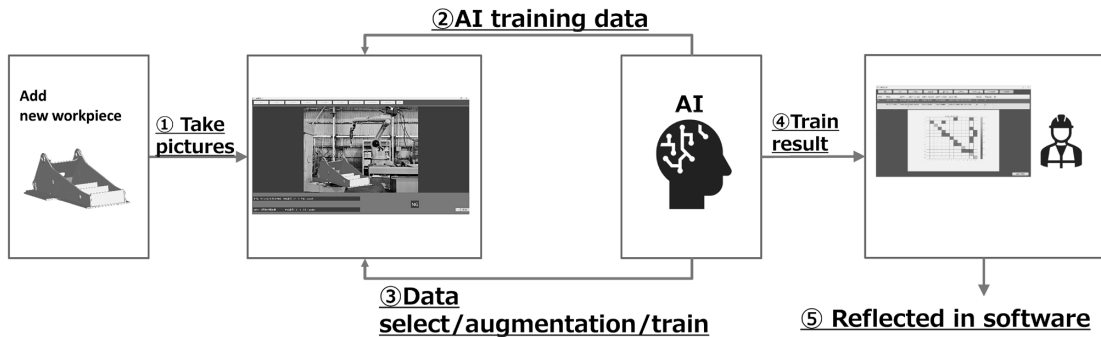


Fig.11 Automatic AI learning flow for new workpiece

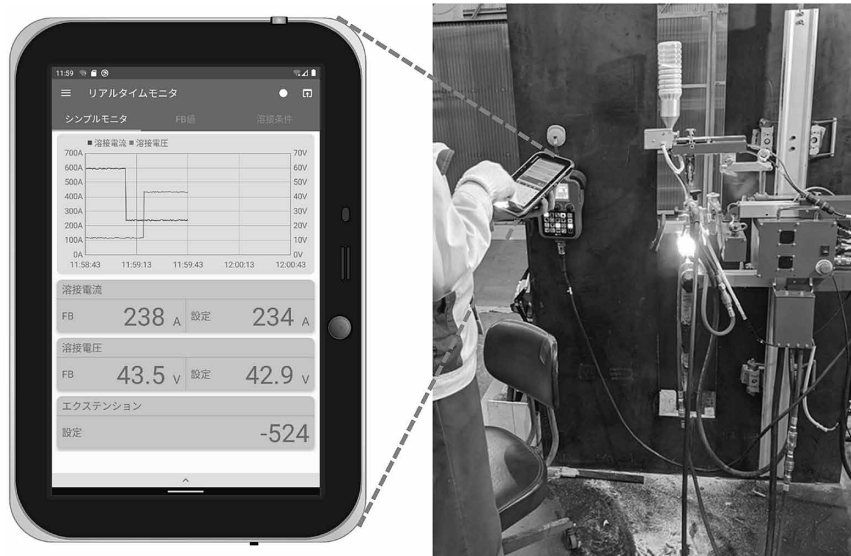


Fig.12 SESLA™ and remote application for SESLA™

visualization of welding processes on desktop PCs and laptops. In certain work environments, skilled operators may be required to continuously oversee welding conditions to ensure the quality of the welds.

However, with the recent decline in the number of skilled operators, the inability to manage multiple welding apparatuses simultaneously has emerged as a significant concern, leading to decreased work efficiency. The implementation of a wireless remote monitoring system addresses this issue by enabling remote monitoring of multiple welding systems from a distance. This monitoring system empowers

non-skilled operators to operate each welding apparatus, potentially allowing each skilled operator to support multiple operators concurrently.

The wireless remote monitoring system functions through wireless communication between the SESLA™ main unit and industrial mobile computers equipped with Android (a trademark of Google LLC)<sup>8)</sup>. It provides real-time monitoring of welding conditions, presenting data in numerical and graphical formats. Moreover, it allows for remote adjustments of welding conditions and the storage of monitoring data in CSV format (Fig.12).

It should be noted that the development of the

wireless remote monitoring system extends beyond the SESLA™ monitoring system and there are plans to make it available for various systems in the future.

## Conclusions

This paper has presented novel functions that merge Kobe Steel's proprietary expertise in welding technology with ICT and AI technology. The ongoing challenges posed by Japan's aging population suggest a sustained demand for automation and workforce reduction within production sites. In response, Kobe Steel remains unwavering in its commitment to development efforts focused on alleviating labor shortages and relieving operators from physically demanding tasks. The company is steadfast in its mission to enhance the automation and quality of welding, ultimately aiming to boost productivity and safety

for its valued customers.

## References

- 1) T. Higashira. Boudayori Technical Guide, Technical Report, 2019, Vol.60, 2019-5.
- 2) K. Sadahiro, et al. R&D Kobe Steel Engineering Reports," 2004, Vol.54, No.2, pp.76-80.
- 3) T. Izumi. Boudayori Technical Guide, Technical Report, 2005, Vol.45, 2005-12.
- 4) K. Sadahiro. Boudayori Technical Guide, Technical Report, 2017, Vol.58, 2017-2.
- 5) K. Yanai. Journal of Information Processing Society of Japan: Computer Vision and Image Media, 2007, Vol.48, No.SIG16 (CVIM19), pp.1-24.
- 6) M. Yano, et al. IEICE Transactions on Information and Systems D, 2019, Vol.J102-D, No.2, pp.34-52.
- 7) A. Fukunaga. Boudayori Technical Guide, Technical Report, 2011, Vol.51, 2011-3, pp.1-6.
- 8) T. Kakizaki. Boudayori Technical Guide, Technical Report, 2020, Vol.61, 2020-3.

# Robotic Welding System with New Equipment for Steel Structures

Takao TOGAWA\*<sup>1</sup> • Bainsi JO\*<sup>2</sup> • Ryohei KURIYAMA\*<sup>3</sup> • Shimpei KAWANISHI\*<sup>4</sup> • Hirohisa KISHIKAWA\*<sup>5</sup> • Taisei FUJIMOTO\*<sup>1</sup>

\*<sup>1</sup> Welding System Department, Technical Center, Welding Business

\*<sup>2</sup> Technical Center, Welding Business

\*<sup>3</sup> Welding Process Department, Technical Center, Welding Business

\*<sup>4</sup> Welding System Department, Technical Center, Welding Business (currently Kobelco Welding TechnoSolutions Co., Ltd.)

\*<sup>5</sup> Welding System Department, Technical Center, Welding Business (currently Kobelco Welding of America Inc.)

## Abstract

*A state-of-the-art welding robot system has been developed for architectural steel frames, featuring the latest technology such as the ARCMAN™ A60 manipulator and the SENSARC™ RA500 welding power source. The system is aimed at increasing productivity and has a reduced cycle time compared with the previous model. This paper provides an overview of the system's components, highlighting the technology that has contributed to the reduction in cycle time. Specifically, the REGARC™ process is covered in detail, which has been improved by the new welding power source, and the welding wire, which now benefits from surface treatment for improved feedability. These advancements have resulted in highly efficient welding conditions, improving the welding current and speed compared with conventional welding techniques, as outlined in this paper. Additionally, the development technology used to create the system equipment is described.*

## Introduction

Recent years have witnessed a consistent annual demand for steel in architectural frames in Japan, stabilizing at approximately 4.6 million tonnes per year<sup>1)</sup>. This demand is anticipated to endure, as there is a pressing need to replace buildings erected during the high economic growth period. However, this scenario poses a challenge due to a shortage of welding technicians, highlighting the imperative for enhancements in both productivity and welding quality. Consequently, there are ongoing initiatives to automate the welding process in the domain of architectural steel frames.

The automation for the welding process of architectural steel frames can be broadly categorized into two primary types: in-factory welding automation and construction site automation. These approaches further break down into automation using vertically articulated robots and automation employing simplified portable robots.

This paper specifically concentrates on in-factory welding automation within the facilities of steel-frame fabricators and introduces a welding robot system that utilizes a vertically articulated robot,

known for its benefits of prolonged continuous operation and high productivity.

## 1. Background of system development

The robotic automation of welding processes for the in-factory settings of architectural steel frames presents challenges due to the unique distinctive feature of each welded structure and the great thickness of the plates involved. The evolution of such robotic automation has involved incorporating mechanisms for automatically generating programs through software technology, enhancing robot functions for multi-layer welding, and integrating equipment to facilitate unmanned operation.

Steel frame fabricators, undertaking the installation of new robot systems, aim not only to introduce cutting-edge equipment but also to modernize existing systems, increase production volume, and reduce labor requirements. In response to such needs, Kobe Steel has been conducting product development to reduce cycle times and contribute to increased productivity. As for cycle time reduction, efforts have been made to shorten both welding and non-welding times. For welding time, a specific focus has been placed on developing welding conditions for cold-formed angular steel columns (hereafter referred to as "columns").

## 2. System Advantages and Configuration

The advantage of Kobe Steel's welding robot system for architectural steel frames lies in its ability to facilitate robot welding for workpieces, each unique and distinctive, without the need for manual teaching of welding paths or conditions on the actual machine. This comprehensive system comprises a welding robot, welding power source, welding wire, a positioner for mounting and posturing workpieces to be welded, a transfer device with a robotic manipulator to expand the range of motion, equipment associated with continuous operation, and steel frame software that automatically generates robot programs. **Fig. 1** displays an exemplary welding robot system for architectural steel frames.

This system introduces newly developed



Fig.1 Structural steel large assembly welding robot system

robotic functions, such as the capability to rectify discrepancies in root gaps that may occur during workpiece assembly and an arc-sensor function to monitor workpiece deformation during welding. Additionally, the system ensures seamless robotic rerun for grooved multi-layered welding by incorporating standard devices for exchanging short/long nozzles, an automated slag remover, a wire cutter, and torch cleaner.

The steel frame software encompasses multiple welding conditions categorized by target joints. Users can access specific welding conditions for each joint by inputting relevant joint information. Two types of welding conditions are offered: one for constant voltage welding and the other for welding utilizing the low-spatter REGARC™ process, which ensures stable globular transfer through pulse waveform control.

The REGARC™ process significantly reduces spatter generation during welding, compared with the constant voltage welding method, thanks to its combination of pulse waveform control and dedicated welding wire. Consequently, the spatter adhering to the base material surface is minimized, reducing the need for spatter removal work in subsequent processes.

The following sections delve into the enhanced performance of the REGARC™ process, made possible by a new power source, welding wire, high-efficiency welding conditions resulting from their use, and technology developed for the system equipment.

### 3. Welding work <sup>2), 3)</sup>

#### 3.1 Improvement of REGARC™ process

##### 3.1.1 Stability improvement of droplet transfer against changing wire extension length

The REGARC™ process alternately outputs two pulse waveforms with different peak currents to stabilize droplet formation and detachment, thereby achieving low spatter during globule transfer in carbon dioxide arc welding. However, a challenge has been the instability of droplet transfer and increased spatter due to the variation in wire extension length, which changes during welding, causing fluctuations in arc length.

The primary joint shape of welding structures for architectural steel frame is a single bevel groove with a gap. During the welding process, a weaving operation is performed to ensure a sound joint, including penetration. However, this weaving operation causes the wire extension length to change at both ends of the groove. This change in wire extension length leads to spatter generation, and in particular, spatter generated on the groove side may adhere to the vertical surface of the workpiece.

Fig. 2 illustrates an example of the mechanism where changes in wire extension length result in the instability of droplet transfer and the generation of spatter. When the wire extension length changes during welding, the base period of the pulse is modulated to track current changes. The base period that has become shorter due to modulation results in insufficient energy, preventing the droplet from adequately growing, leading to insufficient squeezing and weight of the droplet itself. This causes the droplet to be unable to detach with appropriate timing. The droplets that cannot detach may gradually grow and enlarge over time. These enlarged droplets can transform into large-sized spatter due to their contact with the molten pool and the repulsive force of the arc, among other factors <sup>4)</sup>.

To tackle this mechanism, enhancements have been made to improve the stability of droplet transfer and mitigate spatter generation while restraining arc length fluctuations in the globule transfer region, as depicted in Fig. 3.

In the conventional control method, only the base period for droplet formation has been modulated. However, in the new approach, both the base period and the pulse's peak current are modulated simultaneously to ensure sufficient energy for melting the wire and forming droplets. Furthermore, by ensuring a sufficient duration of the pulse's base period during the droplet formation phase,

## Conventional

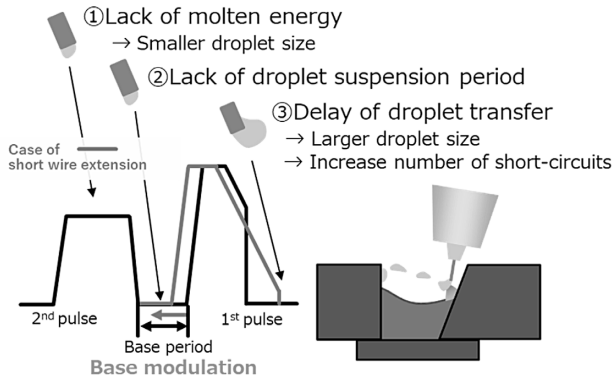


Fig.2 Spatter generation mechanism

## New method

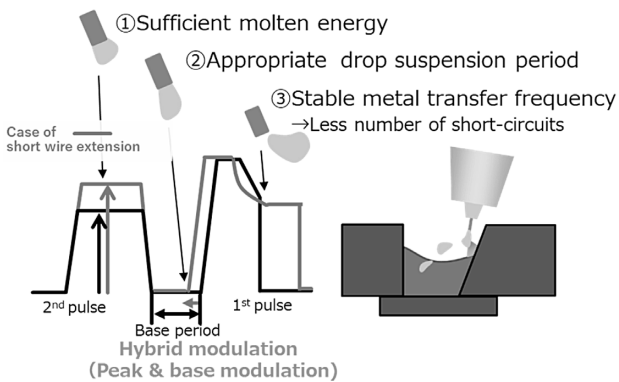


Fig.3 Method for reducing spatter generation

more stable droplet formation has been achieved. Additionally, by introducing a fixed current section during the pulse's descent period in the droplet detachment phase, the success rate of droplet detachment within the specified droplet transfer period has been increased. As a result, excessive droplet growth has been restrained, leading to a reduction in the generation of large-sized spatter. In the new REGARC™ process using the welding power source RA500, the basic waveform of the conventional REGARC™ has been retained, but waveform control has been further optimized to enhance the stability of the droplet transfer mode in

the globule region and reduce spatter. Fig. 4 shows a comparison of droplet transfer phenomena inside a groove.

### 3.1.2 Expansion of welding current region

As a result of enhancing droplet transfer stability, the wire feed speed in REGARC™ has been increased to 18.0 m/min from the conventional 16.4 m/min, and the maximum welding current has been expanded from 320 A to 340 A. This, as will be described in section 3.3, has contributed to realizing high-efficiency welding.

Figs. 5 and 6 compare the droplet transfer modes of the conventional REGARC™ process and the new REGARC™ process at a wire feed speed of 18 m/min and a set welding current of 340 A. In Fig. 5, the conventional method exhibits large spatter resulting from droplets growing and short-circuiting with the molten pool. However, in Fig. 6, the improved control method demonstrates regular droplet formation and stable droplet detachment.

### 3.1.3 Regarding the occurrence of spatter in the groove of steel frame structure

The new REGARC™ process also enhances stability in the droplet transfer mode within the conventional welding current range. Column specimens with a thickness of 22 mm, simulating the structure of an architectural steel frame, were welded using both the conventional REGARC™ process and the new REGARC™ process. Figs. 7 and 8 show the results of comparing the amount of spatter generated when the gap is 4 mm and 10 mm. Under the welding conditions of a set current of 280 A and a wire feed speed of 13.8 m/min, the amount of spatter generated is reduced for both gap conditions of 4 mm and 10 mm. This suggests that even with gap variations due to assembly errors, compared to the reference gap of 7 mm, a reduction in spatter is still observed.

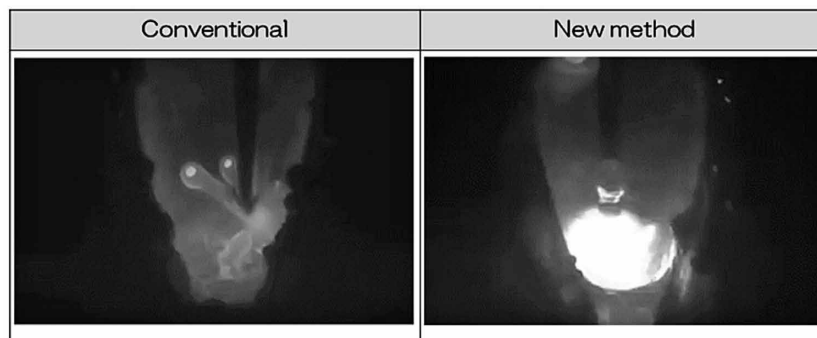


Fig.4 Observation of Metal droplet transfer in welding groove

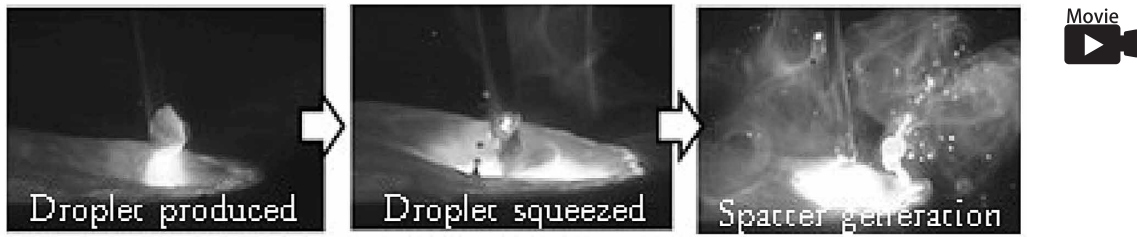


Fig.5 Metal droplet transfer by conventional process

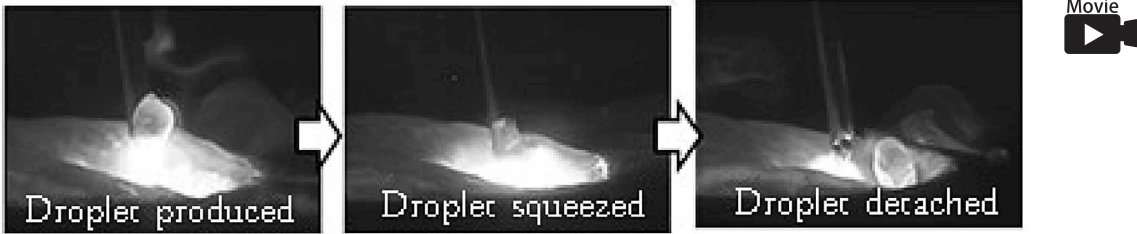


Fig.6 Metal droplet transfer by new process

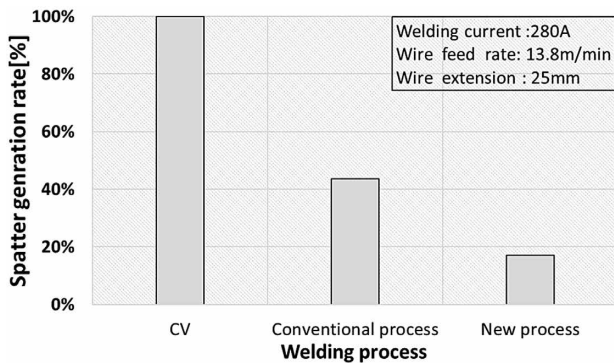


Fig.7 Comparison of spatter generation rate between conventional process and new process (column t: 22mm, gap: 4 mm)

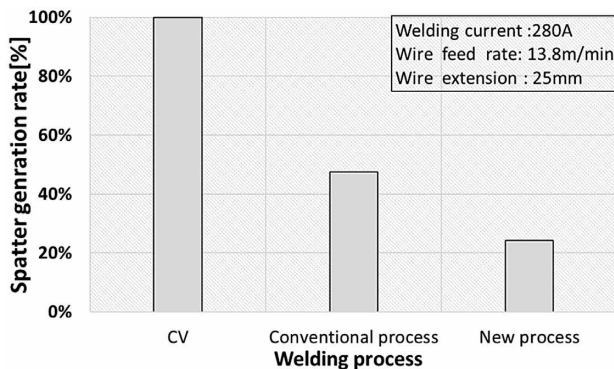


Fig.8 Comparison of spatter generation rate between conventional process and new process (column t: 22mm, gap: 10mm)

### 3.2 Development of dedicated welding wire

The welding wire used in the present process must be capable of responding to an increase in the wire melting rate, which corresponds to an increase in wire feed speed, compared with the conventional process. As the wire feed speed

increases, the reaction force experienced by the wire from the feeding path's inner surface also rises, making it more challenging to maintain a stable wire feed speed. When assuming intermittent, long-duration continuous welding, it is essential for wire feedability to be of superior quality to suppress variations in the wire feed speed and achieve stable welding.

Factors that can influence variations in wire feed speed include the curvature of the feeding path and clogging due to solid matter within the feeding path. Regarding the curvature of the feeding path, the robot system is designed to avoid extremely small curvature radii. And here, the focus is placed on the details of clogging due to solid matter within the feeding path.

The packaged wire installed in the robot system, passes through the feeder from the flexible conduit, and then travels through the conduit liner within the torch cable and the inner tube inside the welding torch before being supplied to welding via the contact tip while receiving power. During this process, solid matter such as copper dust generated from the wire surface continues to deposit on components like the conduit liner, inner tube, and contact tip located downstream of the feeder. This deposition can negatively impact wire feedability and arc stability. In particular, the contact tip, located at the tip of the wire feeding path, has a small clearance with the wire, making it more prone to clogging due to solid matter. While regular cleaning of the feeding path can help mitigate the effects of the deposited solid matter, it may not be practical to clean the feeding path frequently, especially when considering the continuous operation capability of the robot system.

The New REGARC™ dedicated wire, as shown in **Table 1**, has the advantage of suppressing the amount of clogging in the feeding path compared with conventional wire, even under severe welding conditions with high welding current, as demonstrated in **Fig. 9**. This advantage is mainly achieved through a special treatment of the wire surfaces during the wire manufacturing process. The treatment reduces the sliding friction resistance between the wire surface and the conduit liner or inner tube, making it less likely for the copper plating on the wire surfaces to fall off within the feeding path. By applying the New REGARC™ dedicated wire, it is possible to achieve stable welding performance even during extended periods of continuous welding.

### 3.3 High efficiency welding conditions for columns

As described in section 3.1, the new REGARC™ process enables an increase in welding current and wire feed speed, as shown in **Fig.10**. Leveraging the expanded range of welding current and wire feed speed, new welding conditions have been developed for welding around columns and through diaphragms. These newly developed high-efficiency welding conditions maintain the heat input for each path below 30 kJ/cm, similar to the conventional process, while achieving cycle time reduction by increasing welding current and welding speed. This is accomplished while maintaining mechanical performance equal to that of the conventional REGARC™ process.

### 3.4 Joint performance

The welding conditions for the conventional REGARC™ and the newly developed welding conditions were used to evaluate a test piece resembling a joint between a 32 mm thick column and a through diaphragm. The inter-pass temperature between welds was maintained below 250°C, and FAMILIARC™ MG-56R(A) was used for the welding wire. **Table 2** presents a comparison of the mechanical performance of the welded joint, as determined by the results of tensile tests and Charpy impact tests for the weld metal. It should be noted that the Charpy impact test was conducted at a depth of 7 mm from the upper surface of the column in the direction of the plate thickness. Both the tensile strength and Charpy impact test values satisfactorily meet the standards required for architectural steel frame, similar to the conventional method. Moreover, as demonstrated by the cross-sectional macrophotographs in **Fig.11**, comparable

**Table 1** Products applied New REGARC™ process

Products' name	JIS Z 3312 classification	T.S. grade of deposited metal
<b>FAMILIARC™</b> MG-50R(A)	YGW11	490MPa
<b>FAMILIARC™</b> MG-56R(A)	YGW18	550MPa
<b>TRUSTARC™</b> MG-60R(A)	G59JA1UC*	590MPa

\*Index of chemical composition; 3MIT

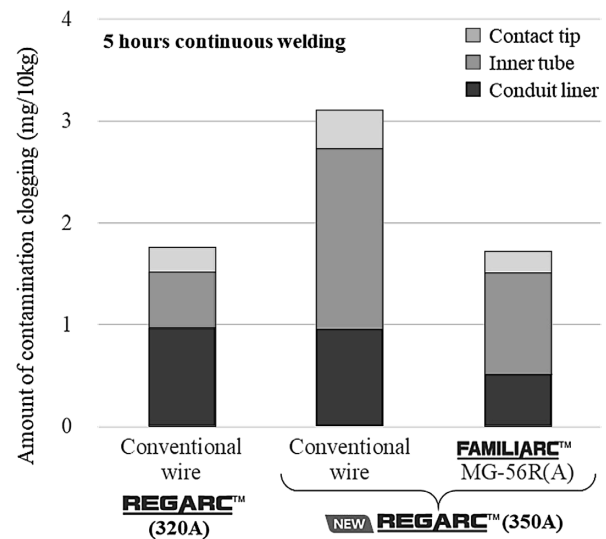


**Fig.9** Example about amount of contamination clogging in wire feeding route parts

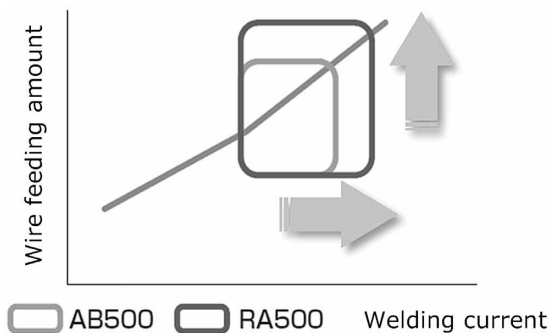


**Fig.10** Expansion of welding current range of REGARC™

**Table 2** Comparison of mechanical properties of weld metal between conventional process and developed process

Item	Location	Conventional	Developed
T <sub>S</sub> (MPa)	Straight	650	643
v <sub>E0°C</sub> (J)	Straight	111	108
	Corner	123	124

results were obtained for the penetration depth achieved by the conventional method and by the newly developed conditions.

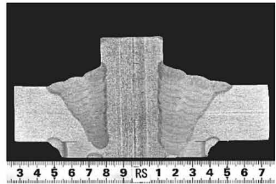
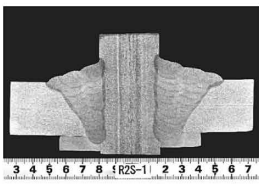
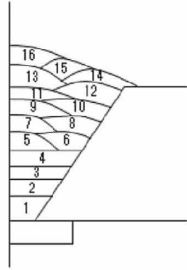
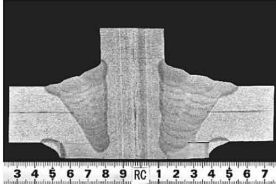
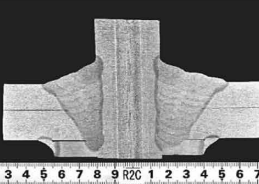
Condition Location	Conventional	Developed	Welding layer
Straight			
Corner			

Fig.11 Cross-sectional macro comparison between conventional method and developed construction conditions

#### 4. Configuration and advantages of new steel frame welding robot system<sup>3)</sup>

This section explains the system components mentioned in Chapter 2, specifically the arc welding robot ARCMAN™ A60, the nozzle autochanger (NAC-3), and other related equipment. Fig.12 displays the appearance of the welding robot and the nozzle autochanger.

One of the advantages of ARCMAN™ A60 is that the center of the robot's one-axis drive section is hollow, allowing for the internal installation of cables within the one-axis part. In the steel frame welding robot system, a slag removal automation device is used, which allows for interchangeability with the welding torch. This setup involves wiring the necessary air hoses and signal lines up to the robot's wrist section. In the conventional system, these hoses and signal lines are run aerially behind the robot. However, in the new steel frame welding robot system, they are wired along the manipulator's lower arm through the one-axis part. This eliminates concerns about interference with the hoses and signal lines, which have previously been wired aerially at the rear, while the robot is in operation.

The nozzle auto changer/cleaner (NAC-3) is designed to prevent nozzle attachment/detachment errors and reduce the time required for replacement operations. Additionally, it features a function that checks if the set nozzle matches the specified position before the nozzle replacement operation, thereby avoiding system stoppages and equipment failures. In conjunction with the development of the NAC-3, the arrangement of related equipment mounted on the robot transfer device and the driving plan of the robot has been optimized. This has led to a reduction in non-welding time for activities such as nozzle cleaning, nozzle replacement, wire cutting, and more. Fig.13

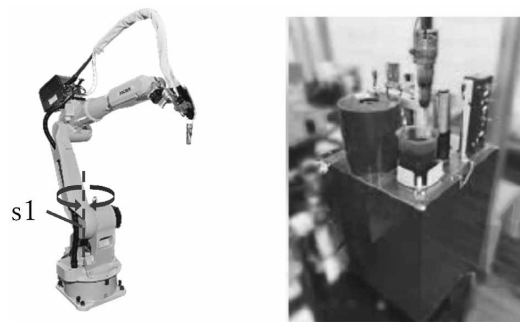


Fig.12 ARCMAN™A60, nozzle auto changer

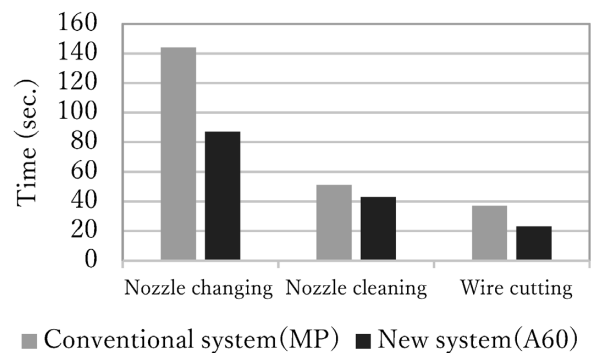


Fig.13 Comparison of related equipment time in structural steel assembly welding robot system

compares the operating times of the conventional ARCMAN™ MP system and the new ARCMAN™ A60 system.

As described above, efforts have been made to optimize the ARCMAN™ A60 and related equipment mounted on the transfer device. The main body of the transfer device has also achieved the high rigidity required for thick plate welding through structural and component shape optimization.

## 5. Benefits

Through the changes in welding conditions, leading to a reduction in welding time, and the optimization of the arrangement of related equipment, which reduced non-welding time, the production time for robot-based column welding has been reduced by up to 10% or more<sup>3)</sup>.

As an example, the cycle time for a single joint with a column dimension of 800 mm square, a plate thickness of 32 mm, and a root gap of 7 mm was estimated and compared. The results are presented in **Table 3**. Approximately 15% of the overall cycle time and about 12% of the arc-on time have been shortened. Furthermore, the reduction in arc-on time has led to a decrease in the usage of shielding gas. It should be noted that this cycle time is calculated using actually measured values for the developed welding conditions and related equipment operating times, with the assistance of Kobe Steel's steel frame software. Therefore, it may differ from the cycle time observed on the actual machine. Additionally, this calculated cycle time includes the time required for removing slag from the intermediate layer.

Table 3 Comparison of estimate cycle time

	Conventional MP×AB500	New system A60×RA500
Cycle time (min)	201	171
Welding time (min)	148	129
Arc ratio (%)	73.4	75.5
Shielding gas consumption (L)	3,689	3,229
Pass count (pass)	16	16

## Conclusions

This paper has introduced the latest technology and advantages related to Kobe Steel's steel frame welding robot system. The foundation for productivity enhancement enabled by these new technologies is stable and uninterrupted operation during continuous welding. While space constraints limited the extent of the description, it should be noted that Kobe Steel is not only focused on productivity enhancement but also on achieving stable operation and quality enhancement. Hopefully, the utilization of these new technologies and items in production settings can contribute to both productivity and quality enhancement in the field of welding.

## References

- 1) Steel Structure Journal, Japan Steel Structure Journal Co. Ltd. 2022, No.2082, p.1.
- 2) K. Yamazaki et al. Welding Technology. 2010, Vol.58, No.5, pp.80-84.
- 3) Y. Fujimoto et al. Boudayori Technology Guide, Technology Report. 2022, Vol.513, pp.2-6.
- 4) Y. Yokota et al. R&D Kobe Steel Engineering Reports. 2013, Vol.63, No.1, pp.42-47.

# Welding Process and Welding Consumables for Offshore Wind Power Generation Facilities

Kosuke YAMAGUCHI\*1 • Satoru KANO\*1

\*1 Welding Process Department, Technical Center, Welding Business

## Abstract

Japan's domestic policy aimed to achieve carbon neutrality by 2050 has resulted in a growing interest in power generation methods that employ renewable energy sources with low CO<sub>2</sub> emissions. Among these methods, offshore wind power generation has garnered significant attention in recent years. Wind turbines in offshore facilities rely on foundations such as monopiles for support. With the increasing size of wind turbines, the monopiles have also grown gigantic in diameter and length, making it necessary to use extra-thick steel plates for their construction. Welding these plates requires an appropriate welding process and welding consumables. To meet these requirements, Kobe Steel has developed a new electroslag welding process for extra-thick plates, SESLA™, and welding consumables for narrow-groove submerged-arc welding(SAW), FAMILIARC™ US-29HK and TRUSTARC™ PF-H55LT-N.

## Introduction

Since the Great East Japan Earthquake on March 11, 2011, the nation's energy policy has undergone scrutiny, with increasing anticipation for renewable energy as a new source. Among these, one renewable energy that is attracting particular attention is offshore wind power generation. In order to overcome the energy crisis that European countries are also facing, they are successively announcing plans for the large-scale introduction of offshore wind power generation. In Japan, Round 1 bidding in the offshore wind promotion area has concluded, with expectations for Rounds 2 and 3 bids in the future<sup>1)</sup>.

In offshore wind power generation, significant costs are associated with installation, mooring, grid connection, operation, and maintenance. Ensuring profitability requires a crucial focus on increasing power generation per windmill. Technology development to enhance output by upsizing rotor diameter is actively progressing and, as depicted in Fig. 1, the rated power output of wind turbines for wind power generation is increasing gradually. Recent years have seen the adoption of windmills with a rated power output of 5 to 8 MW in offshore wind power generation. The anticipation is for larger windmills exceeding 10 MW in rated power output

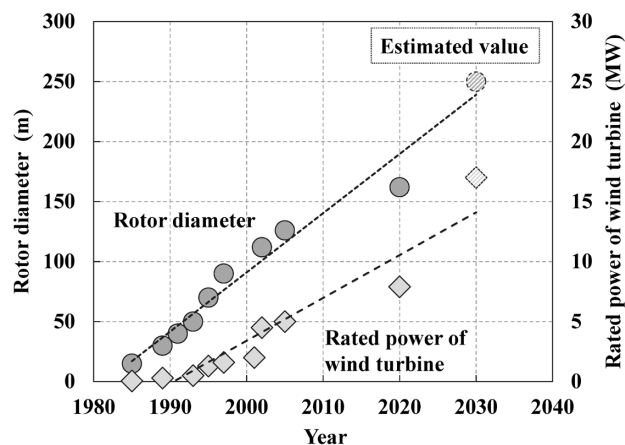


Fig. 1 Growth of rotor diameter of wind turbines and rated power for wind power generation<sup>3)-5)</sup>

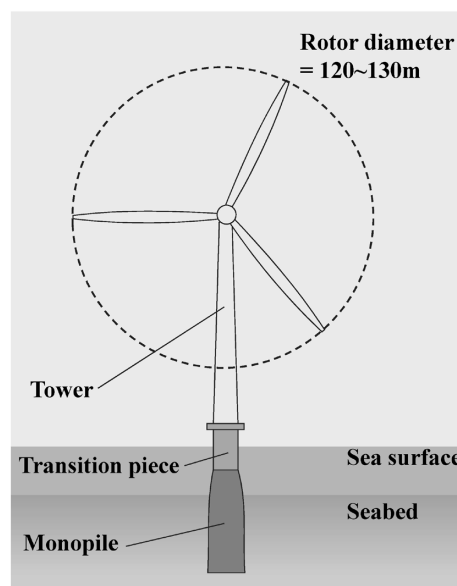


Fig. 2 Schematic image of a 5 MW-class offshore wind power generation facility

in the future, reflecting the trend toward upsizing offshore wind power generation equipment<sup>2)</sup>.

As illustrated in Fig. 2, offshore wind power generation equipment utilizes towers supporting windmills and monopiles beneath the sea surface as basic components. These are constructed by welding steel pipes made of extra-thick plates with a thickness exceeding 50 mm. For manufacturing single pipes and weld joints, both vertical and circumferential welding are indispensable, and an

efficient welding process for extra-thick plates is being sought.

This paper introduces a new electro slag welding (hereinafter referred to as ESW)<sup>6)</sup> process suitable for vertical welding (vertical seams) on extra-thick plates and welding consumables for narrow-groove SAW suitable for circumferential welding.

### 1. New ESW process, SESLA™

The new ESW process, SESLA™ (hereinafter referred to as SESLA™), is a high-efficiency vertical automatic welding process developed by Kobe Steel on the basis of the element technology of ESW. Unlike arc welding, ESW forms a slag bath, and welding progresses by melting the wire through resistive heating in this bath. This results in the significant advantage of minimal generation of spatter and fumes. Moreover, since the molten pool is protected by the slag bath, this welding process exhibits excellent wind resistance even without the use of shielding gas. The configuration of SESLA™ is illustrated in Fig. 3. The welding involves using a water-cooled copper sliding shoe on the front side of the groove and FAMILIARC™ KL-4 as a backing material on the back side. Similar to the process in conventional ESW, an arc is generated at the start of welding. The introduced flux is melted to form a slag bath. The electrical resistance heating of the molten slag bath serves as the heat source, melting the flux-cored wire. During this process, penetration is formed through the convection action of the slag bath, allowing welding to be completed in a single pass even in butt joints of thick plates.

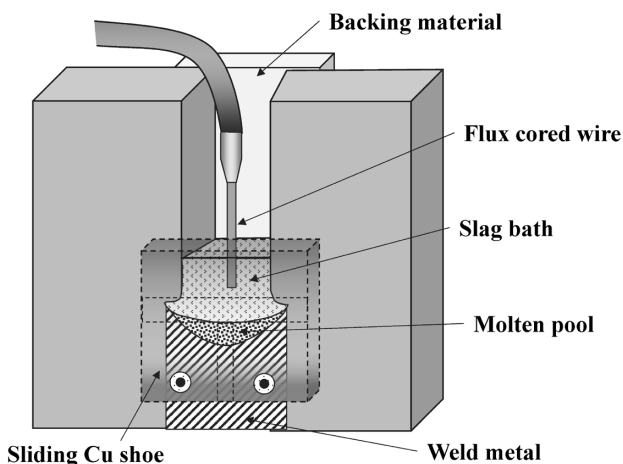


Fig. 3 Configuration of SESLA™

### 1.1 SESLA™ dedicated welding consumables

Electro gas arc welding (hereinafter referred to as EGW) is widely applied in the shipbuilding sector and other industries as a high-efficiency vertical automatic welding process, similar to ESW. EGW uses an arc as the heat source and employs shielding gas, so it is necessary to consider the welding environment, including the risk of shield failure and fume generation. On the other hand, while ESW allows welding without the use of shielding gas, there is a limitation on the welding length due to the structure of the welding equipment.

SESLA™ is a new welding process developed to overcome the shortcomings of ESW. It utilizes a specific welding apparatus and dedicated welding consumables, namely the flux-cored wire FAMILIARC™ ES-X55E and the melting-type flux FAMILIARC™ EF-4. A study has been conducted using JIS G 3106 SM490A steel plates to investigate the impact of preheating on the mechanical properties of SESLA™ weld metal. The relationship between heat input and proof strength/tensile strength is shown in Fig. 4, and the relationship between heat input and -20°C absorbed energy is shown in Fig. 5. The strength of SESLA™ weld metal decreases with an increase in heat input; however, it maintains excellent notch toughness.

### 1.2 Application to extra thick plates

The SESLA™ achieves excellent mechanical properties across a broad spectrum of heat inputs, and it has been verified that single-pass welding is viable for plate thicknesses up to 80 mm. Table 1 outlines the conditions for testing and welding extra-thick plates with a thickness of 80 mm. JIS G 3106 SM490A was used as the base metal. Fig. 6 displays

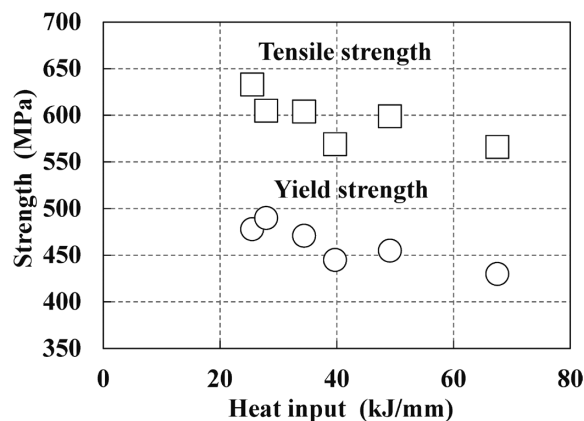


Fig. 4 Relationship between heat input and tensile strength of SESLA™

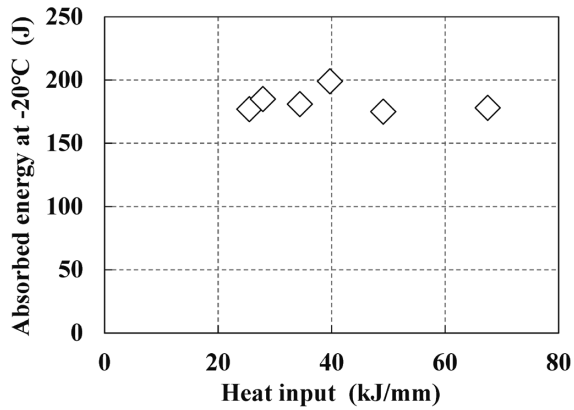
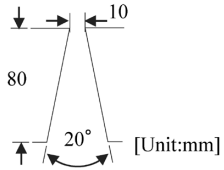


Fig. 5 Relationship between heat input and -20°C absorbed energy in SESLA™

Table 1 Test condition of butt joint welding

Wire-flux combination	FAMILIARC™ ES-X55E / FAMILIARC™ EF-4
Base metal	JIS G 3106 SM490A, 80 mm×(150+150) mm×600 mm <sup>L</sup>
Groove configuration	
Welding parameter	DCEP, 420 A-47 V-17 mm/min
Heat input	69.7 kJ/mm
Preheat	Room temp.
PWHT condition	As-welded

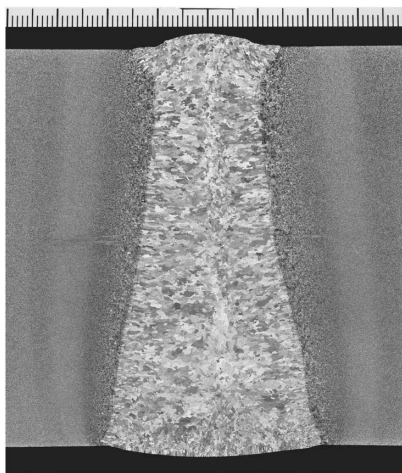


Fig. 6 Cross-sectional macrograph of weld joint

Table 2 Chemical composition of weld metal (mass%) \*1

C	Si	Mn	P	S
0.06	0.20	1.22	0.010	0.004

\*1 Location: Center of weld metal

Table 3 Mechanical properties of weld metal

Location	Tensile properties*1			Notch toughness*1			
	0.2%PS (MPa)	TS (MPa)	El. (%)	Absorbed energy (J)			
				[-40°C]		[-20°C]	
7 mm beneath the face side	435	561	24	168 169 153	Avg. 163	186 196 214	Avg. 199
40 mm beneath the face side	438	568	25	191 176 155	Avg. 174	191 202 207	Avg. 200
73 mm beneath the face side	446	577	23	162 159 163	Avg. 161	184 200 136	Avg. 173

\*1 Tensile test specimen: round tensile specimen, Dia.=10 mm, G.L.=50 mm  
Impact test specimen: 10×10 mm square shape, 2 mm V notch based on AWS B4.0

the macrostructure of the weld joint, while **Table 2** presents the chemical composition of the weld metal, and **Table 3** provides its mechanical properties. Satisfactory penetration is observed for a plate thickness of 80 mm. Despite the increased heat input of up to 69.7 kJ/mm, the weld metal maintains ample strength and exhibits excellent notch toughness at -40°C.

## 2. Consumables for narrow groove submerge arc welding

For welding extra-thick plates, the utilization of SAW with a high-deposition rate, is common. An effective approach to enhance its efficiency involves narrowing the groove. In response to narrow groove requirements in SAW, new SAW materials, namely FAMILIARC™ US-29HK and TRUSTARC™ PF-H55LT-N, have been developed. The following introduces the details:

FAMILIARC™ US-29HK is a solid wire for carbon steel, while TRUSTARC™ PF-H55LT-N is a fluoride-basic type bonded flux, adopting a flux design with enhanced basicity index. The advantages lie in the optimization of the flux design, ensuring excellent notch toughness and excellent slag removability in narrow grooves. Notably, these materials can be used with both direct current (DCEP) and alternating current (AC).

### 2.1 Performance of deposited metal

The investigation encompassed various performance characteristics of the deposited metals of FAMILIARC™ US-29HK and TRUSTARC™ PF-H55LT-N. **Table 4** presents the chemical composition of the deposited metal under both DCEP and AC. **Table 5** and **Fig. 7** present the as-deposited mechanical properties. It has been verified that a deposited metal with high strength (exceeding 550 MPa) and exceptional absorbed energy up to

**Table 4** Chemical composition of deposited metal (mass%)\*1, 2

	Polarity	C	Si	Mn	P	S
[F]US-29HK,	DCEP	0.07	0.29	1.85	0.013	0.002
[T]PF-H55LT-N*3	AC	0.08	0.27	1.73	0.013	0.002

\*1 Location: Center of the deposited metal  
 \*2 Welding condition: 550 A-30 V-420 mm/min; Ext.=30 mm; 4.0 mm wire dia.  
 \*3 [F]: FAMILIARC™ welding consumables,  
 [T]: TRUSTARC™ welding consumables

**Table 5** Mechanical properties of deposited metal\*1, 2

	PWHT condition	Polarity	0.2 %PS (MPa)	TS (MPa)	El. (%)
[F]US-29HK,	As-welded	DCEP	514	603	28
[T]PF-H55LT-N*3		AC	534	618	29

\*1 Size of impact test specimen is based on AWS B4.0  
 Tensile test specimen: round tensile specimen, Dia.=12.5 mm, G.L.=50 mm  
 Location: the same as analysis location for chemical composition  
 \*2 Welding condition: 550 A-30 V-420 mm/min; Ext.=30 mm; 4.0 mm wire dia.  
 \*3 [F]: FAMILIARC™ welding consumables,  
 [T]: TRUSTARC™ welding consumables

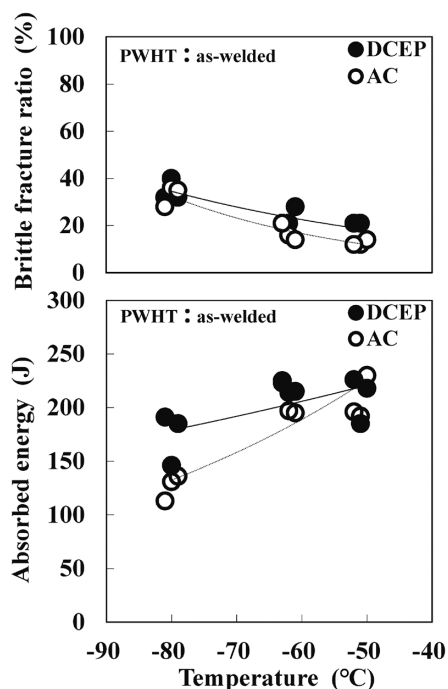


**Fig. 7** Transition curves of notch toughness of deposited metal in as-welded condition\*1, 2

\*1 Size of impact test specimen is based on AWS B4.0 Impact test specimen: 10×10 mm square shape, 2 mm V notch Location: the same as analysis location for chemical composition  
 \*2 Welding condition: 550 A-30 V-420 mm/min; Ext.=30 mm; 4.0 mm wire dia.

**Table 6** Diffusible hydrogen test results\*1

	Polarity	Diffusible hydrogen content (mL/100g)			
		N=1	N=2	N=3	Avg.
[F]US-29HK,	DCEP*2	3.2	3.3	3.3	3.3
[T]PF-H55LT-N					

\*1 Test method: JIS Z3118, gas chromatography method  
 \*2 Welding condition: 550 A-30 V-400 mm/min; Ext.=30 mm; 4.0 mm wire dia.  
 Redrying condition: 350°C×1 h, Welding atmosphere: 11°C×79 %RH

-60°C can be obtained.

**Table 6** displays the amount of diffusible hydrogen when welding with the combination of FAMILIARC™ US-29HK and TRUSTARC™ PF-H55LT-N under direct current (DCEP). Through the optimization of flux design, the amount of diffusible hydrogen has become as low as approximately 3 mL/100g.

## 2.2 Performance of weld joints

A test evaluating various performance characteristics of weld joints was performed using the combination of FAMILIARC™ US-29HK and TRUSTARC™ PF-H55LT-N in narrow gap SAW. **Table 7** outlines the test conditions, **Table 8** details the welding conditions, and **Fig. 8** illustrates the groove shape and welding procedure. Tandem welding aimed at achieving high efficiency was executed with a bipolar trailing electrode of 2.4 mm. The electrode arrangement for tandem welding is depicted in **Fig. 9**. **Fig.10** presents a cross-sectional macrograph of the weld joint, while **Table 9** details the chemical composition of the weld metal, and **Table 10** provides its mechanical properties. In the

**Table 7** Test condition of both side butt joint welding

Electrode	FAMILIARC™US-29HK, Leading electrode(L):4.0 mm dia. Trailing electrode(T):2.4 mm dia.×2 wires
Flux	TRUSTARC™PF-H55LT-N
Base metal	JIS G 3106 SM490A, 80 mm <sup>t</sup> ×(150+150) mm <sup>w</sup> ×800 mm <sup>L</sup>

**Table 8** Welding parameters for both side butt joint welding

	No. of passes	Welding parameter*1	Heat input (kJ/mm)
1st side	1	Single, DCEP, 600 A-30 V-600 mm/min	1.8
	2	Single, DCEP, 650 A-30 V-600 mm/min	2.0
	3-8	Tandem, L: DCEP, 650 A-30 V T: AC, 600 A-32 V-700 mm/min	3.3
2nd side	1	Single, DCEP, 600 A-30 V-600 mm/min	1.8
	2-21	Tandem, L: DCEP, 650 A-30 V T: AC, 600 A-32 V-700 mm/min	3.3

\*1 Preheat and inter pass temperature.:100~147°C

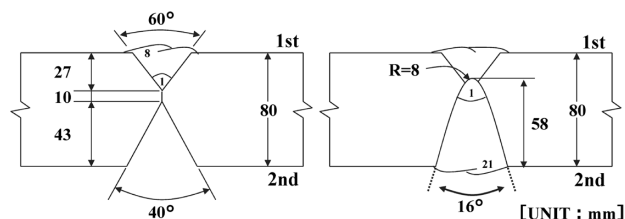


**Fig. 8** Groove configuration and pass sequences

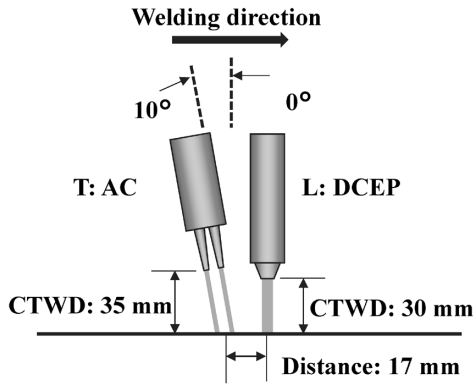


Fig. 9 Electrode configuration of tandem welding

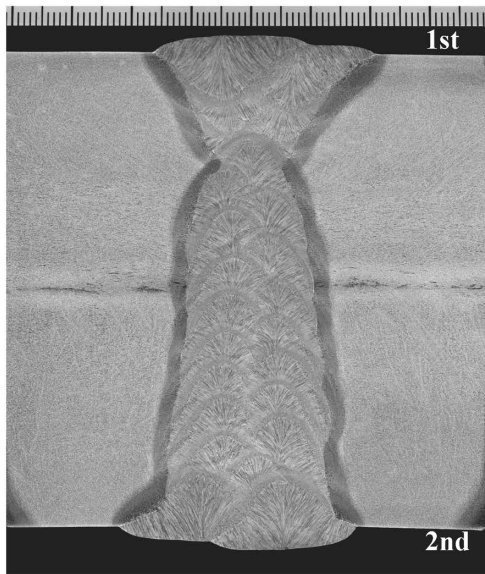


Fig.10 Cross-sectional macrograph of both side butt joint welding

weld joint, excellent impact performance at  $-60^{\circ}\text{C}$  is ensured while maintaining strength<sup>7</sup>.

## Conclusions

In recent years, there has been a growing expectation for the sustainable utilization of wind power generation as a renewable energy source. Particularly, offshore wind power generation is expanding globally, with significant growth observed in Europe. In Japan, the Cabinet has resolved to introduce offshore wind power generation on a large scale as a key strategy for the substantial integration of renewable energy into the main power supply. This decision is outlined in the 6th Next Energy Basic Plan (2021)<sup>8</sup>.

This paper has introduced SESLA<sup>TM</sup>, a suitable welding process for the extra-thick plates used in the fabrication of components like giant monopiles in offshore wind power generation facilities, as well as consumables for narrow gap SAW, namely "FAMILIARC<sup>TM</sup> US-29HK / TRUSTARC<sup>TM</sup> PF-H55LT-N." These contribute to the high-efficiency welding of extra-thick plates, allowing the weld metal to attain excellent mechanical properties, including the necessary strength and low-temperature notch toughness required for large steel structures used offshore. This is anticipated to result in a broad application spectrum in the offshore wind power sector, focusing not only on the integrity and reliability of weld joints but also on the demand for upsizing and mass production of power generation facilities.

Table 9 Chemical composition of weld metal (mass%)\*<sup>1</sup>

C	Si	Mn	P	S
0.09	0.30	1.78	0.014	0.003

\*1 Location: Center of weld metal

Table 10 Mechanical properties of weld metal\*<sup>1</sup>

Location	Tensile properties* <sup>2</sup>			Notch toughness* <sup>2</sup>			
	0.2 %PS (MPa)	TS (MPa)	El. (%)	Absorbed energy (J)			
				[-60°C]		[-40°C]	
7 mm beneath 2nd side	496	618	33	112	Avg. 121	161	Avg. 155
				123		156	
				127		147	
40 mm beneath 2nd side	580	634	28	162	Avg. 165	194	Avg. 195
				181		196	
				152		196	
73 mm beneath 2nd side	591	664	28	128	Avg. 146	184	Avg. 184
				130		185	
				179		183	

\*1 PWHT condition: as-welded

\*2 Tensile test specimen: round tensile specimen, Dia.=6.0 mm, G.L.=24 mm

Impact test specimen: 10×10 mm square shape, 2 mm V notch based on AWS B4.0

## References

- 1) Renewable Energy Institute. Trends in offshore wind power generation. 3rd edition, 2022, pp.6-19.
- 2) New Energy and Industrial Technology Development Organization. NEDO Renewable Energy Technology White Paper. 2nd edition, Chapter 3: Offshore Wind Power, Morikita Publishing, 2014, pp.45-46.
- 3) N. Honjio. The Institute of Electrical Engineers of Japan. 2009, Vol.129, No.5, pp.284-287.
- 4) IRENA. Renewable Power Generation Costs in 2021. 2022, p.106.
- 5) IEA. World Energy Outlook 2019. 2019, pp.619-620.
- 6) T. Kakizaki. Boudayori. 2020, Vol.507, pp.2-6.
- 7) Kobelco Welding Today. 2021, Vol.24, pp.3-7.
- 8) Ministry of Economy, Trade and Industry, Agency for Natural Resources and Energy. 6th Next Energy Basic Plan. 2021, pp.34-60.

# Development of Automatic Welding System for 9% Ni Steel LNG Tanks

Kenta YAMASAKI\*<sup>1</sup> · Hirofumi MANIWA\*<sup>1</sup> · Dr. Yoshihiko KITAGAWA\*<sup>1</sup> · Tsuyoshi MIWA\*<sup>2</sup> · Keito ISHIZAKI\*<sup>2</sup>

\*<sup>1</sup> Welding Process Department, Technical Center, Welding Business

\*<sup>2</sup> Technical Center, Welding Business

## Abstract

*The demand for liquefied natural gas (LNG) is expected to rise, and 9% Ni steel is the material of choice for the tanks (both for above-ground and marine applications) used to store and transport it. However, welding of 9% Ni steel requires high skill levels and is prone to defects like lack of fusion. To address this issue, this paper introduces a portable, specialized robot system designed for the highly efficient and deskilled welding of 9% Ni steel. The system utilizes a cartesian coordinate robot with mounting jigs, sensing methods, welding power supply, and optimal welding conditions tailored to the manufacturing of 9% Ni steel LNG tanks. This robot system allows welders to produce sound-quality welded joints during vertical welding of 9% Ni steel, with reduced defects. Furthermore, by using two robots simultaneously with one operator, significant improvements in efficiency can be expected.*

## Introduction

In line with the global trend towards decarbonization for carbon neutrality, there has been a sharp increase in demand for natural gas, which is a crucial transition energy with lower CO<sub>2</sub> emissions than oil and coal<sup>1)</sup>. When storing and transporting gas by vessels, it is common for it to be liquefied at -162°C and sealed in dedicated tanks. Therefore, many tanks for LNG are manufactured using 9% Ni steel, which excels in strength and low-temperature toughness.

This paper relates to the welding of 9% Ni steel LNG tanks, whose demand is expected to increase, and introduces the development of an automatic welding system using a compact portable robot (product name, “KI-700”), which enables deskilling and high efficiency by combining Kobe Steel’s nickel-based alloy flux-cored wire (hereafter referred to as Ni-based FCW) for 9% Ni steel LNG tanks.

## 1. Development background

Nickel-based alloys exhibit high viscosity when melted, leading to poor fluidity. Additionally, their melting point is lower than that of the 9% Ni steel base metal, making lack of fusion defects more likely to occur during welding. Consequently, establishing an appropriate groove shape and employing special

electrode manipulation are necessary to sufficiently melt the groove during welding. Blow holes are also prone to occur due to the infiltration of oxygen and moisture from the atmosphere and other factors, necessitating proper shielding and control of arc length. Thus, the use of nickel-based alloy welding consumables demands a high level of skill, with variations in quality likely due to the welder’s expertise. On the other hand, the shortage of highly skilled welders has become a serious issue, further exacerbated by the retirement of experienced welders. The environment for welding 9% Ni steel structures has become more tough<sup>2)</sup>.

Against this background, Kobe Steel has commercialized an automatic welding system using a compact portable robot, named “KI-700”, that can be applied to the welding of LNG tanks, which are experiencing a rapid increase in demand. This system is expected to compensate for the shortage of welders and decline in skill, thereby contributing to the high efficiency and high-quality construction of storage facilities, which are indispensable for CO<sub>2</sub> reduction.

## 2. Development of process for Nickel-based-alloy flux-cored arc welding (Ni-based FCAW)

The process introduced in this paper involves a specialized welding robot optimized for Kobe Steel’s HASTELLOY®<sup>Note 1)</sup> type Ni-based FCW, recognized for its outstanding resistance to hot cracking. The configuration also incorporates a digital welding power supply and dedicated rails. This section provides detailed information about the robot, power supply, and rails. In the development of this process, one factor causing the decrease in working efficiency of semi-automatic welding in a vertical position is considered to be the need for repair work associated with the occurrence of short-length bead connection. Therefore, the focus has been placed on achieving long-seam welding. The goal is to complete the welding without stopping midway in the vertical welding of 4 meters, the maximum width of 9% Ni steel plates, ensuring the production of sound weld metal.

Note 1) HASTELLOY is a registered trademark of HAYNES International Inc.

## 2.1 Development of compact portable robot

The KI-700 is a portable Cartesian coordinate robot system developed on the basis of a conventional model, which has a track record in the short-length welding of the medium-to-thick plate made of general carbon steel used in industries such as structural steel, bridges, and shipbuilding. The name “KI-700” covers a manipulator, controller, and teaching box. The appearance of the KI-700 is shown in Fig. 1.

The KI-700 features a manipulator weight of approximately 6 kg, making it both compact and lightweight. Another notable attribute is its capacity for remote operations using the teaching box. Additionally, its software functionality enables the automatic generation of a suitable build-up sequence and welding conditions tailored to Ni-based FCW, utilizing groove shape data automatically detected through touch sensing. Consequently, it can effectively address variations in machining and assembly precision, ensuring stable welding quality with straightforward operations, even without the need for highly skilled operators.



Fig. 1 Appearance of KI-700 compact portable welding robot for Ni steel

Improvements to the groove sensing method are depicted in Fig. 2. In the conventional welding of medium-to-thick plates, commonly involving robotic applications, a root gap of approximately 4 to 10 mm is utilized. However, in the application of welding marine tanks, where the KI-700 is expected to be utilized, the anticipation is for thin plates with an envisioned zero-millimeter root gap. Therefore, precise shape detection is essential due to the relative narrowing compared to the grooves traditionally considered in sensing methods. The KI-700 addresses this need by adopting a teaching-dedicated metal tip that excels in machining precision and rigidity, departing from the conventional practice of combining sensing with slightly bent welding wire. During sensing, the contact tip is replaced with this dedicated tip. Furthermore, the newly developed touch sensing, in contrast to conventional methods limited to obtaining location information from the welding groove surface, now captures location information from both the welding groove surface and the adjacent base metal surfaces.

## 2.2 Optimization of function for automatically generating welding conditions/build-up sequence

As indicated in Section 2.1, the KI-700 automatically generates suitable welding conditions and a build-up sequence tailored to Ni-based FCW on the basis of groove shape data. The unique aspects of this capability will be further detailed below.

As mentioned at the outset of Section 1, in vertical LNG tank welding, critical considerations encompass: inadequate fluidity leading to lack of fusion; joint strength reduction attributed to the disparity in melting points between the base metal and the weld metal; and the decrease in alloy components in the weld metal due to base

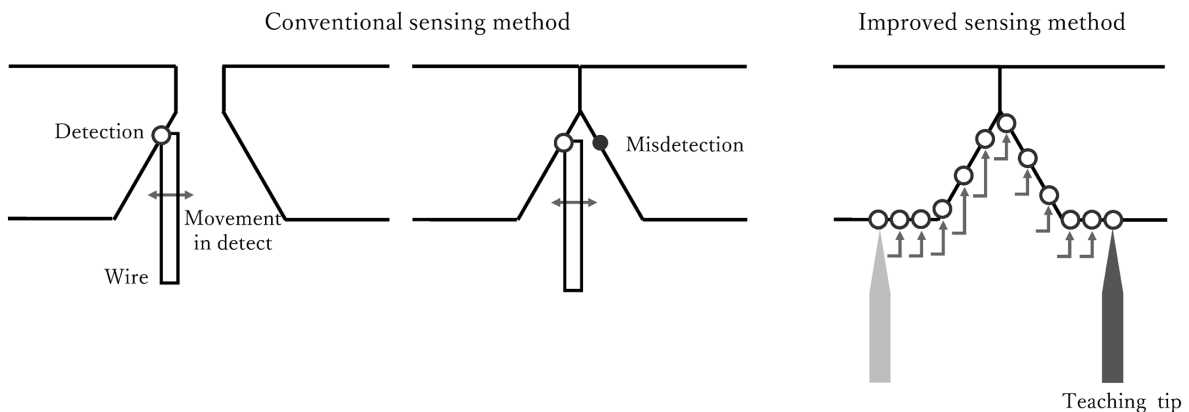


Fig. 2 Schematic diagram of improved sensing method

metal dilution. The decline in joint strength poses a particular challenge, especially with thin plates. This arises from the base metal temperature easily rising during welding, coupled with a substantial proportion of the root section where base metal dilution is more pronounced. Taking these factors into consideration, optimizations have been implemented.

Specifically, attention has been paid to wire aiming positions to prevent lack of fusion, adjusting welding heat input and weaving width for each path to prevent dilution, ensuring proper conditioning of the molten pool for arc stability in root welding, and considering the build-up sequence and weaving conditions that promote the attainment of a flat bead shape. Consequently, the capability to successfully perform vertical welding has been realized, as demonstrated by positive test results presented in Section 3 and subsequent sections.

### 2.3 Welding power source

The welding of 9% Ni steel using Ni-based FCW is carried out within a relatively low current range to mitigate the risk of hot cracking. In conventional power sources with thyristors, the low control frequency contributes to insufficient arc stability in the low current range, prompting a preference for inverter-controlled power sources. The robot-specific digital control inverter welding power source, **SENSARC™** AB500, introduced by Kobe Steel in 2010, is equipped with advanced current and voltage control capabilities. Leveraging these features, it offers high-quality and versatile welding modes, rendering it optimal for medium-to-thick plate welding<sup>3)</sup>. Furthermore, to enable the use of Ni-based FCW in the vertical welding position and improve arc stability in the low current range of 200 A and below, the KI-700 has been enhanced with a dedicated mode for the Ni-based FCAW process.

Assuming a welding length of 4 meters in an LNG tank, the external appearance of the shield nozzle after 40 minutes of continuous welding is displayed in **Fig. 3**. This outcome affirms that spatter adhesion to the shield nozzle, which can disrupt the shielding gas, is minimized. This is credited to the inherent low spatter design of Kobe Steel's Ni-based FCW and the additional reduction achieved through the digital control of the power source. Even during 40 minutes of continuous welding, the spatter adhesion to the shield nozzle remains minimal. Moreover, considering the heat resistance required for prolonged welding, a welding torch with a higher rated duty cycle than conventional robots has been chosen.

### 2.4 KI-700 dedicated rail

The length of the vertical welding joint in a 9% Ni steel LNG tank depends on the width of the steel plate, with a maximum length of approximately 4 meters. Furthermore, 9% Ni steel is susceptible to magnetization, leading to welding defects caused by magnetic arc blow during welding. As a result, the use of magnets, commonly employed to prevent the manipulator from falling and for securely fixing metal rails with a rack as the running axis to the base metal, is not feasible. Hence, owing to the lightweight effect of the KI-700 manipulator, it has been determined that secure fixation is achievable with easily attachable and detachable vacuum clamps. Consequently, the system has adopted vacuum clamps.

The overview of the dedicated rail developed for the KI-700 is illustrated in **Fig. 4**. To ensure rigidity, considering the lifting process, a reinforcement frame has been attached to the main rail. The suction power of the vacuum clamp is designed to withstand the weight of the manipulator and cables. To prevent unintended falls, a fall prevention fixture has also been added to ensure safety.

### 3. Vertical welding test using KI-700

This section presents the details of the vertical welding tests specifically designed for actual LNG tank welding using the KI-700.

The 9% Ni steel LNG tank is broadly classified into "above-ground storage tanks" and "marine tanks" employed for transportation on ships or as fuel tanks. To meet the distinct mechanical performance requirements of the welding sections, two types of Ni-based FCWs have been lined up, namely, **PREMIARC™** DW-N709SP (above-ground storage) and **PREMIARC™** DW-N609SV (marine).



**Fig. 3** Nozzle appearance after 40 minutes continuous of welding

Both products share the common advantage of excellent workability during vertical welding. As outlined in Section 2.1 and Section 2.2, the KI-700 automatically computes the optimal welding conditions (current-voltage-speed-weaving

condition) and build-up sequence for each Ni-based FCW on the basis of the sensed groove shape. The results of welding tests conducted under these specified welding conditions and build-up sequence demonstrated exceptional welding quality, as shown in Section 3.1 and Section 3.2. Further details are shown below.

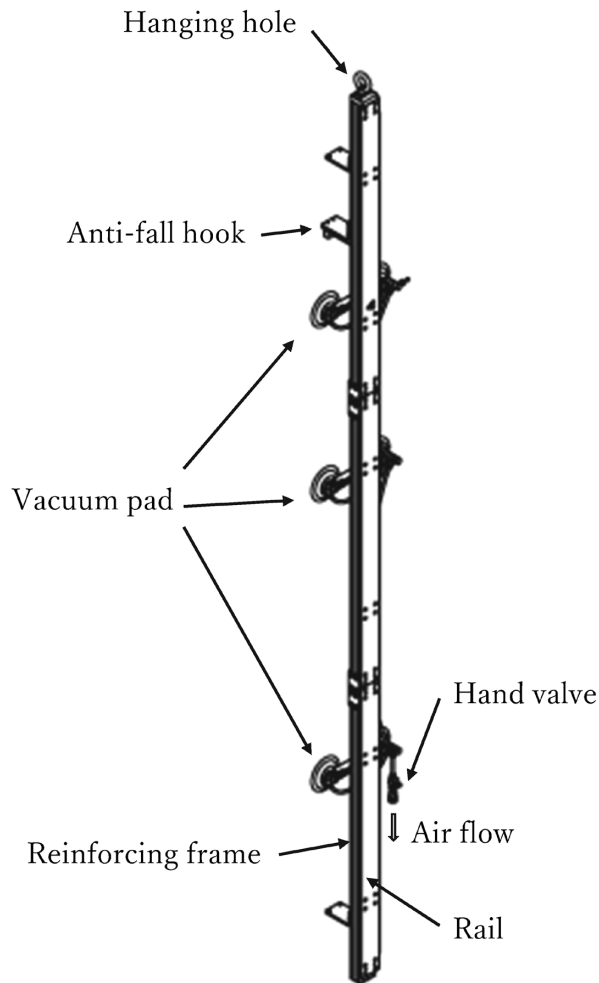


Fig. 4 KI-700 dedicated 4 m long welding rail

### 3.1 Conditions assumed for above-ground LNG tanks

Table 1 presents the scope of application for the KI-700, considering welding for an above-ground LNG tank. Additionally, Table 2 displays the output results of the recommended welding conditions automatically generated for joint welding with a plate thickness of 12 mm, considering the combination with the **PREMIARC™** DW-N709SP welding wire for the above-ground LNG tank. On the basis of these results, a groove was actually formed. The process involved a combination of gas cutting and grinding on the 1st side, and on the 2nd side, mechanical processing such as milling was performed after welding on the 1st side. Table 3 shows the bead appearance, cross-sectional macro photographs, and mechanical performance obtained when automatic welding has been conducted under the conditions specified in Table 2. Under both conditions with a root gap of 3 mm and

Table 1 KI-700 applicable groove dimension for aboveground LNG storage tank

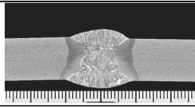
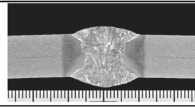
Welding position	Thickness	Groove angle	Root gap
Vertical upward	12-35 mm	55-65°	3-7 mm

Table 2 Welding conditions for **PREMIARC™** DW-N709SP generated by KI-700

Root gap 3 mm				
	Welding current (A)	Arc voltage (V)	Welding speed (mm/min)	Welding heat input (kJ/mm)
1st	150	26	156	1.5
	160	26	219	1.1
2nd	160	26	132	1.9
	160	26	114	2.2
Root gap 7 mm				
	Welding current (A)	Arc voltage (V)	Welding speed (mm/min)	Welding heat input (kJ/mm)
1st	150	26	96	2.4
	160	26	162	1.5
2nd	160	26	132	1.9
	160	26	114	2.2

※Machining [back chipping]  
※Ceramic backing bar consumable was used.

Table 3 Bead appearance, cross-sectional shape of weld metal, mechanical test results of weld metal by **PREMIARC™** DW-N709SP

	Root gap 3 mm	Root gap 7 mm
Bead appearance		
Macro-structure		
Tensile strength (MPa) (Test temperature : 20°C) [Target value ≧ 690 MPa]	754 (Fractured position : weld metal)	725 (Fractured position : weld metal)
Absorbed energy (J) (Test temperature : -196°C) V notch [Target value ≧ 55 J]	91,78,92 Avg. 87	86,95,78 Avg. 86

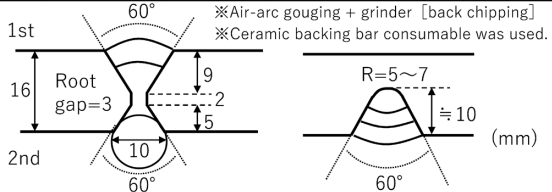
7 mm, satisfactory appearances and mechanical properties have been achieved. In the joint tensile test, the weld metal has fractured, but it satisfies the strength standards for the base metal and meets the requirements of the pressure vessel standard JIS B 8265. In semi-automatic welding performed by a welder, it is estimated that the maximum continuous welding length in a vertical position is generally around 700 mm. With the KI-700, there is no such limitation, enabling stable continuous welding even for long-length welds exceeding 1 meter. To evaluate the stability in long-length welding, a 1-meter-long vertical welding joint was created, and radiographic testing was conducted. The welding conditions and results are presented in **Table 4**. For a welding length of 900 mm, no lack of fusion has occurred, and there are a total of 7 blowholes. This level of performance is well within the passing criteria of JIS B 8265 (either Class 1 or Class 2 according to JIS Z 3106). It confirms the high-quality stability of long continuous welding achieved through the combination of **PREMIARC™** DW-N709SP and KI-700.

### 3.2 Conditions assumed for marine LNG tanks

**Table 5** outlines the KI-700's application scope, considering welding for a marine LNG tank. Given its role as a fuel tank, strict capacity assurance is required. To prevent deviation towards lower capacity due to welding-induced deformation, the allowable root gap range is narrower, specifically ranging from 0 to 3 mm, in comparison with above-ground LNG tanks. As demonstrated in Section 2.1, the conventional sensing method shows a reduction in touch sensing points at a 0 mm gap,

Table 4 Welding conditions for **PREMIARC™** DW-N709SP generated by KI-700 and radiography results

	Welding current (A)	Arc voltage (V)	Welding speed (mm/min)	Welding heat input (kJ/mm)
1st	150	26	126	1.9
	160	26	149	1.7
2nd	160	26	136	1.8
	170	27	143	1.9
	160	26	116	2.2

Linear defect	Spherical defect	JIS B 8265
N.D.	Blow hole 7pieces (dia. 0.6~0.9 mm)	Satisfied.

※Evaluation length in radiography : 900 mm

Table 5 KI-700 applicable groove dimension for marine LNG storage tank

Welding position	Thickness	Groove angle	Root gap
Vertical upward	12-35 mm	55-65°	0-3 mm

with increased likelihood of detection errors in the groove width direction sensing. Consequently, a newly developed sensing method has been adopted for marine LNG tank conditions.

**Table 6** shows the output results of the recommended welding conditions using the marine LNG tank welding wire **PREMIARC™** DW-N609SV,

Table 6 Welding conditions for **PREMIARC™** DW-N609SV generated by KI-700

	Welding current (A)	Arc voltage (V)	Welding speed (mm/min)	Welding heat input (kJ/mm)
1st	160	27	181	1.4
	170	27	151	1.8
2nd	160	25	237	1.0
	170	27	191	1.4

※Air-arc gouging + grinder [back chipping]

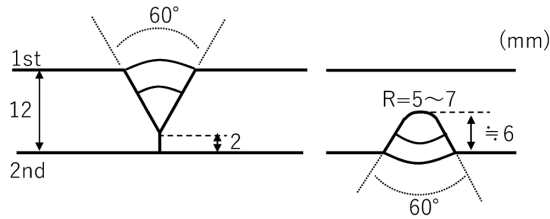
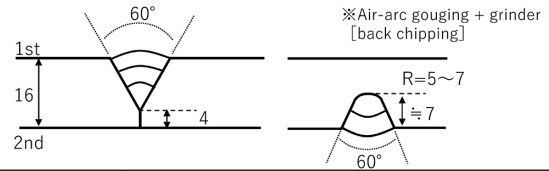


Table 8 Welding conditions for **PREMIARC™** DW-N609SV generated by KI-700 and radiography results

	Welding current (A)	Arc voltage (V)	Welding speed (mm/min)	Welding heat input (kJ/mm)
1st	160	27	207	1.3
	170	27	194	1.4
	170	27	167	1.7
2nd	160	25	199	1.2
	170	27	153	1.8



Linear defect	Spherical defect	JIS B 8265
N.D.	Blow hole 5pieces (dia. 0.6~0.9 mm × 4, dia. 1.0 mm × 1)	Satisfied.

※ Evaluation length in radiography :1800 mm

Table 7 Bead appearance, cross-sectional shape of weld metal, mechanical test results of weld metal by **PREMIARC™** DW-N609SV

	Root gap 0 mm
Bead appearance	
Macro-structure	
Tensile strength (MPa) (Test temperature : 20°C) [Target value ≧ 690MPa]	722 (Fractured position : weld metal)
Absorbed energy (J) (Test temperature : -196°C) V notch [Target value ≧ 34 J]	84, 80, 80 Avg. 81

with input conditions specified for joint welding with a plate thickness of 12 mm. On the basis of these results, an actual groove was formed. The process involved a combination of gas cutting and grinding on the 1st side, and on the 2nd side, a combination of air arc gouging and grinding was performed after welding on the 1st side. **Table 7** shows the bead appearance, cross-sectional macrographs, and mechanical properties obtained by automatic welding under the conditions outlined in Table 6. It is evident that excellent appearance and mechanical properties have been achieved.

Similarly to the case of above-ground LNG tanks, a vertical welding joint with a welding length of 2 meters was created to evaluate the stability of

long-length welding in the groove of the marine tank, and radiographic testing was conducted. **Table 8** presents the welding conditions and results. For 1,800 mm of welding length, there are 5 blowholes, and no lack of fusion has occurred. This performance level, akin to the previously mentioned **PREMIARC™** DW-N709SP, aligns well with the passing criteria of JIS B 8265, confirming the high-quality stability in long continuous welding achieved through the combination of **PREMIARC™** DW-N609SV and KI-700.

#### 4. Enhancement effect on work execution efficiency achieved by using KI-700.

In Ni-based alloys, cracks almost invariably occur at the bead's terminal crater. Therefore, it is necessary to completely remove the crater with a grinder for bead connection. As discussed in Section 3, the use of KI-700 in LNG tank vertical upward welding enables stable long-length welding with consistent quality. This reduces the need for grinding work during bead connection approximately every 700 mm, as required in semi-automatic welding. Furthermore, there is no longer a need for the welder to move scaffolding to align with the welding position of the vertical joint. Moreover, the KI-700 can continuously weld without constant monitoring, except for the task of removing slag. This allows a single operator to simultaneously execute work on two joints.

The estimated results for the total working hours when a welder individually executes 36 locations of vertical welding joints with a plate thickness

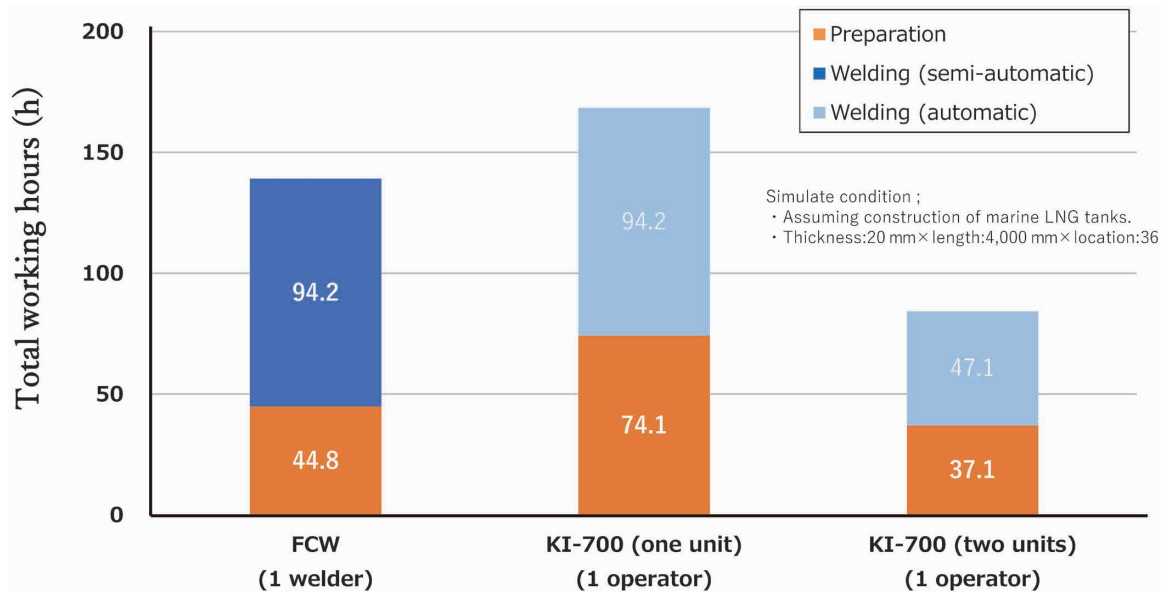


Fig. 5 Comparison of total working hours for various welding procedures

of 20 mm and a welding length of 4 meters are presented in Fig. 5. The breakdown of welding preparation includes slag removal, grinding of craters (bead connection), back chipping, and contact tip replacement. When applying the KI-700, the preparation time increases due to rail installation work and the time required for groove sensing with the KI-700. However, the welding process is automated, resulting in an approximately 50% working hour reduction for workers. While welding hours remain unchanged from those of semi-automatic welding, the productivity per day increases, as the operation continues even when welders are taking breaks. Furthermore, by having one worker handle two KI-700 units, alternately performing the preparation and welding, the total working hours, including welding, are reduced by approximately 40% compared with semi-automatic welding, contributing to a shorter project duration.

## Conclusions

This paper has outlined Kobe Steel's initiatives in achieving de-skilling, high efficiency, and stable quality in LNG tank vertical welding. Kobe Steel aspires to become the "most trusted welding solution

company in the world." The automatic welding system utilizing KI-700 in conjunction with Ni-based FCW represents a welding solution product that capitalizes on Kobe Steel's expertise in robotics, welding consumables, welding power sources, and welding execution methods. In recent years, there has been a noticeable surge in the demand for constructing energy infrastructure, encompassing not only LNG tanks but also hydrogen/ammonia tanks, and liquefied CO<sub>2</sub> tanks, aligning with the pursuit of carbon-neutral goals. The Kobe Steel welding solutions presented in this paper are put forth to make meaningful contributions to society.

## References

- 1) The Agency for Natural Resources and Energy. Comprehensive Energy Survey Committee, Resource and Fuel Division: Direction of oil and natural gas policies looking toward 2030/2050 (draft). General Resource and Energy Survey Committee, Resource and Fuel Subcommittee, Oil and Natural Gas Sub-Committee (13th meeting). 2021.
- 2) Y. Kitagawa, Boudayori Technology Guide. Technology Report. 2022, Vol.63, 2022-4.
- 3) K. Tsuji et al. R&D Kobe Steel Technical Reports. 2013, Vol.63, No.1, pp.48-53.

# Welding Consumables for 780 MPa Class Steel with Excellent Notch Toughness after PWHT

Satoru KANO\*1 • Masayuki NAGAMI\*1 • Masahiro INOMOTO\*2 • Dr. Takanori ITO\*2

\*1 Welding Process Department, Technical Center, Welding Business

\*2 Materials Research Laboratory, Technical Development Group

## Abstract

Over the past few years, the demand for larger structures like spherical tanks and pressure vessels has risen, leading to a requirement for higher strength steel and welding consumables. However, the use of post-weld heat treatment (PWHT) to relieve welding residual stress has been known to deteriorate the notch toughness of high-strength weld metal. To investigate the factors contributing to this deterioration, an analysis has been conducted on the fracture surface morphology and microstructure after impact testing of weld metal for 780 MPa class steel, with electrodes for flux-cored arc welding as the main focus. The findings suggest that temper embrittlement and precipitation hardening caused by carbide are the main reasons for the deterioration of notch toughness after PWHT. Following several studies, an empirically derived component system of weld metal has been developed to minimize the negative aspects of temper embrittlement or precipitation hardening caused by carbide after PWHT. Utilizing these results, Kobe Steel has launched TRUSTARC™ Note 1) LB-80LSR as a shield-metal arc-welding consumable for 780 MPa class steel, which boasts excellent notch toughness even after PWHT.

## Introduction

In the construction of spherical tanks, pressure vessels, and similar structures, PWHT is employed to reduce residual stresses introduced by welding and enhance fatigue properties. Due to the recent surge in energy demand, there is a trend toward upsizing and higher pressure in those structures, driving advancements in high-strength steel materials and welding consumables. More recently, significant progress has been made in the development of PWHT capable high-strength steel, exemplified by EN10028-6 P690QL2, boasting a tensile strength of 780 MPa, designed specifically for liquefied CO<sub>2</sub> tanks for ships<sup>1)</sup>. This advancement has resulted in an increased demand for welding consumables suitable for this type of steel.

Typical 780 MPa-class steel weld metal undergoes a decrease in notch toughness following PWHT. One

contributing factor is temper embrittlement (mainly referring here to embrittlement caused by the segregation of phosphorus (P) at grain boundaries) occurring after specific PWHT<sup>2)</sup>. Another factor is precipitation hardening resulting from the formation and growth of carbides during PWHT due to impurity elements like Nb, V, and solid-solution hardening elements such as Cr, Mo<sup>3), 4)</sup>.

This paper investigates the fracture morphology and microstructure of Charpy impact test specimens after PWHT, with weld metal produced using shielded metal arc welding rods (SMAW) and rutile-based flux-cored wire (FCW). Furthermore, the study explores the ingredient range of 780 MPa class steel weld metal, demonstrating excellent notch toughness even after PWHT.

## 1. Experimental method

Various components were integrated to manufacture the SMAW and FCW for 780 MPa class steel. **Table 1** outlines the composition range of the weld metals prototyped in this paper. Weld metals were created through prototype SMAW on a test plate with a thickness of 20 mm, a groove angle of 20°, and a root gap of 16 mm, employing direct current electrode positive (DCEP). Furthermore, weld metals were produced by prototype FCW on a similarly sized test plate through multi-layer welding using shield gas Ar+20%CO<sub>2</sub>.

The average heat input during welding was 2.0 kJ/mm for SMAW and 1.3 kJ/mm for FCW. In SMAW, preheat and interpass temperatures were maintained at 95-105°C, while in FCW, the preheat temperature was set at 100-120°C, and the interpass temperature ranged from 140 to 160°C. To assess the effects of temper embrittlement and carbide-induced embrittlement, PWHT was conducted under two conditions: 2 hours at 580°C and 8 hours at 620°C after welding. Tensile test specimens and Charpy

Table 1 Chemical composition range of weld metals investigated in this study (mass%)

C	Si	Mn	Ni	Cr	Mo	Others
0.05 - 0.08	0.2 - 0.3	0.7 - 2.0	2.4 - 5.5	Max. 0.3	0.1 - 0.5	Ti, B

Note 1) TRUSTARC is a registered trademark (TM) of Kobe Steel.

impact test specimens were extracted from the central portion of the weld metals to evaluate their tensile strength and notch toughness. Additionally, the microstructure of each weld metal was observed using an optical microscope, scanning electron microscope (SEM), and scanning transmission electron microscope (STEM). The STEM observation samples were prepared using the extraction replica method. The identification of trace elements that segregate locally in the weld metal was performed using the three-dimensional atom probe tomography (APT) method.

## 2. Effects of PWHT on 780 MPa-class steel weld metals

The Larson-Miller parameter (hereinafter referred to as “LMP”) serves as an index for PWHT conditions. LMP is calculated using Equation (1):

$$LMP = T (\log t + 20) \quad \dots\dots\dots (1)$$

wherein,  $T$  represents the PWHT temperature (K), and  $t$  is the PWHT holding time (h).

A PWHT at 580°C for 2 hours corresponds to an LMP of  $17.3 \times 10^3$ , and a PWHT at 620°C for 8 hours corresponds to an LMP of  $18.7 \times 10^3$ . The relationship between the Larson-Miller Parameter (LMP) and -40°C absorbed energy for conventional materials (SMAW and FCW) producing 780 MPa-class steel weld metals is depicted in Fig. 1. In terms of concentration in the weld metal, SMAW results in approximately 0.5% of Mo, while FCW yields around 2% of Mn.

SMAW exhibits reduced notch toughness as LMP increases. In FCW, notch toughness declines under low PWHT conditions when LMP ranges from 17.0 to  $18.0 \times 10^3$ . However, when LMP exceeds  $18.0 \times 10^3$ ,

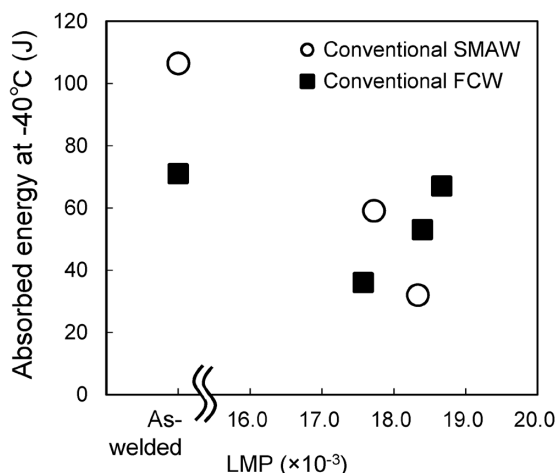


Fig. 1 Relationship between LMP and absorbed energy at -40°C with conventional SMAW and FCW

notch toughness gradually recovers. The reduction in notch toughness after PWHT in SMAW is thought to result from both “temper embrittlement” and “embrittlement due to precipitation hardening caused by Mo-dominated carbides.” The drop in notch toughness in FCW at LMP levels of 17.0 to  $18.0 \times 10^3$  is primarily attributed to temper embrittlement. The factors contributing to the gradual recovery of notch toughness at LMP levels above  $18.0 \times 10^3$  will be discussed later.

### 2.1 Effect at low LMP conditions (LMP $\leq 18.0 \times 10^3$ ) (Verification with FCW)

The investigation into the connection between low LMP conditions (PWHT at 580°C for 2 hours, corresponding to LMP= $17.3 \times 10^3$ ) and temper embrittlement was conducted using FCW within the composition range outlined in Table 1, with a specific focus on the Mn content in the weld metal. Fig. 2 displays the fractography of -40°C Charpy impact test specimens under low LMP conditions, showcasing variations in the Mn content in the weld metal. In such conditions, a higher Mn content in the weld metal leads to dominant grain boundary fracture along the prior austenite grain boundaries (PAGB), while a lower Mn content results in dominant ductile fracture.

In other words, it has been determined that the primary cause of temper embrittlement is grain boundary fracture along the PAGB, attributed to the Mn content in the weld metal. To explore elements cosegregating with Mn, trace elements around the PAGB in weld metals with varying Mn contents were measured using the APT method. The concentration profile of phosphorus (P), exhibiting local segregation, is depicted in Fig. 3. Phosphorus (P) segregates along the PAGB, and there is an observable trend of increased segregation with higher Mn content. Therefore, in weld metals with elevated Mn content, it is inferred that phosphorus (P) is more prone to cosegregation under low LMP conditions, thereby promoting grain boundary fracture.

### 2.2 Effect at high LMP conditions (LMP $> 18.0 \times 10^3$ ) (Verification with FCW)

In the composition range of weld metals outlined in Table 1, the study centers on weld metal with added chromium (Cr) and molybdenum (Mo) using FCW. Investigation has been carried out on the microstructure under high LMP conditions (8 hours of PWHT at 620°C, equivalent to LMP= $18.7 \times 10^3$ ). The microstructure, examined with an optical

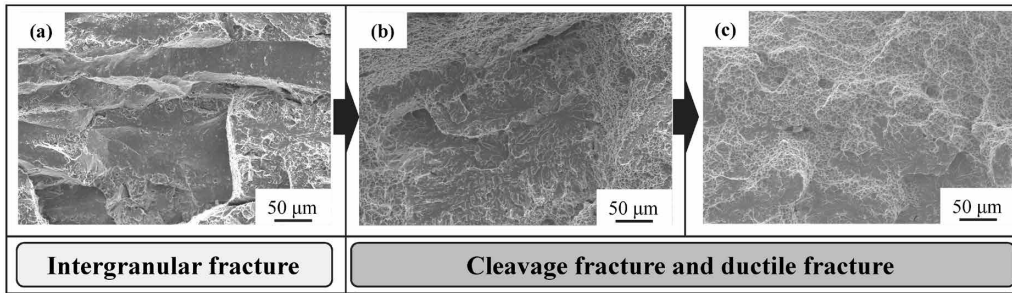


Fig. 2 Fractographs of impact test specimens containing different Mn content at low LMP condition (a) High Mn content, (b) Middle Mn content, (c) Low Mn content

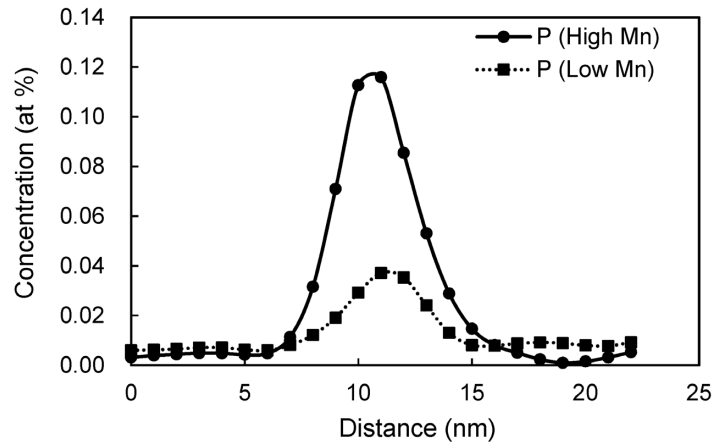


Fig. 3 Concentration profiles of phosphorus around the PAGB at low LMP condition measured by APT method

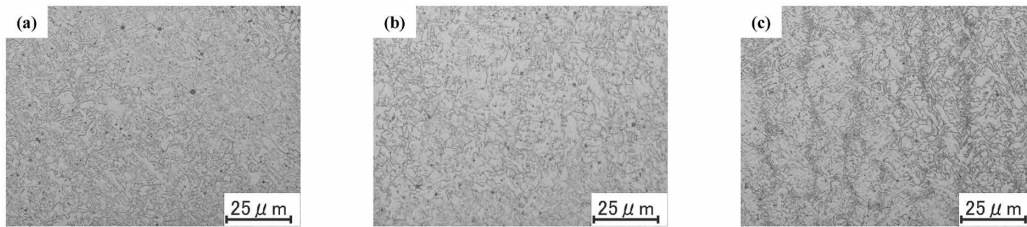


Fig. 4 Optical micrographs of weld metals (a) As-welded, (b) Low LMP condition, (c) High LMP condition

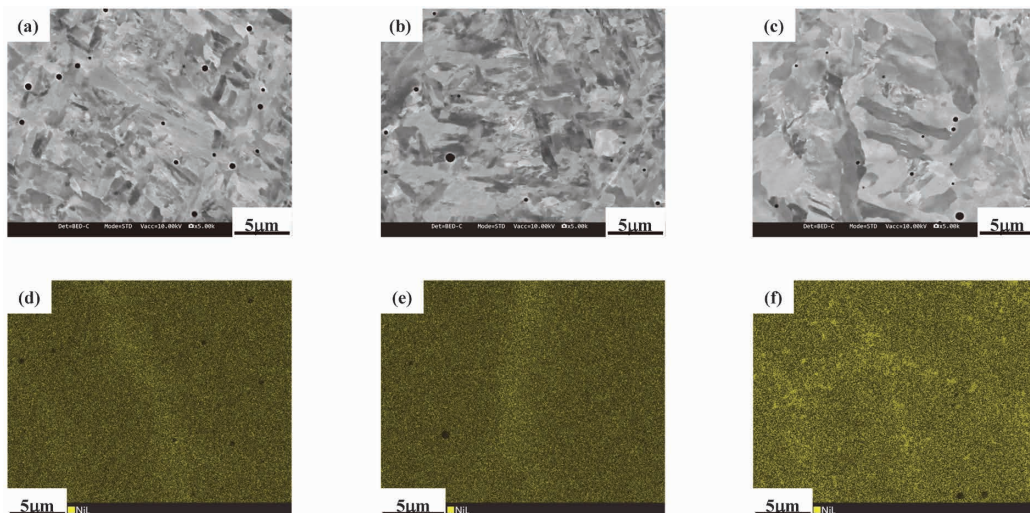


Fig. 5 SEM micrographs of weld metals and SEM-EDX analysis results of Ni (a), (d) As-welded, (b), (e) Low LMP condition, (c), (f) High LMP condition

microscope, is depicted in **Fig. 4** in its as-welded state, with the inclusion of low LMP conditions. In the targeted weld metal, a mesh-like micro segregation zone (referred to as the “segregation zone”) is observed under high LMP conditions, contrasting with the as-welded and low LMP conditions<sup>5</sup>.

Subsequently, in **Fig 5**, the microstructure near the segregation zone and the analytical results using a Scanning Electron Microscope with Energy Dispersive X-ray Analysis (SEM-EDX) are presented. Segregation zones were noted irrespective of PWHT, with a predominant concentration of Ni in the segregation zone. This hints at the potential for structural changes in the segregation zone after PWHT. Consequently, an analysis using electron backscatter diffraction (EBSD) was performed on the weld metal. The inverse pole figure (IPF) map and phase map obtained through EBSD are shown in **Fig. 6**. From the IPF map and phase map, it is apparent that the metallographic structure of the targeted weld metal is predominantly ferrite in the as-welded state, with PWHT causing the ferrite to coarsen. The microstructure referred to as “ferrite”

here is a composite structure consisting of bainitic ferrite and in-grain ferrite (acicular ferrite)<sup>6</sup>.

Under high LMP conditions, an increase in austenite has been observed compared with the as-welded state. This austenite is identified as retained austenite, undergoing reverse transformation, and retained until room temperature in the high LMP conditions.

In the previously mentioned conventional material (FCW), the gradual recovery of notch toughness under high LMP conditions is believed to stem from the presence of soft austenite. The effective utilization of austenite retained through PWHT necessitates a reduction in the Ac1 transformation point, indicating the essential addition of a specific amount of alloy. Further validation is required for the alloying additive that manifests this effect.

In high LMP conditions, the possibility of embrittlement due to carbides was considered, leading to an investigation using STEM. The microstructure observed through STEM is shown in **Fig. 7**. The carbides found in the targeted weld metal are primarily composed of cementite,

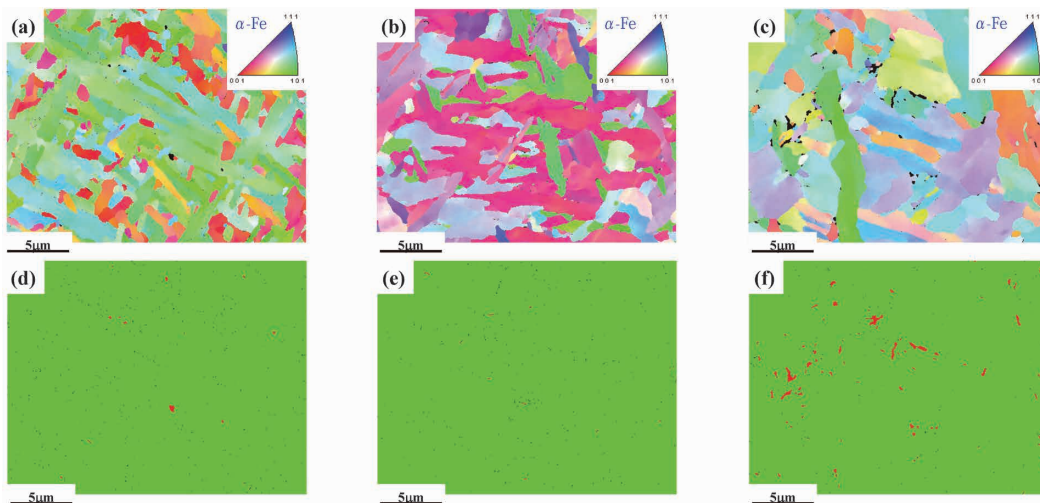


**Fig. 6** IPF maps and phase maps obtained by EBSD  
(a), (d) As-welded, (b), (e) Low LMP condition, (c), (f) High LMP condition (Green : Ferrite, Red : Austenite)

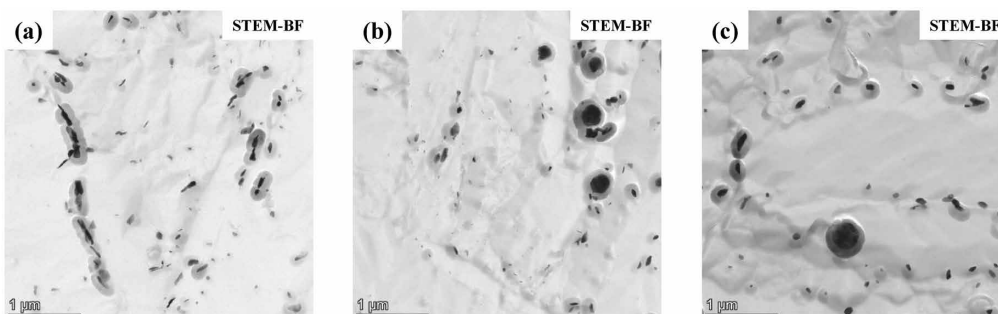


**Fig. 7** STEM micrographs of weld metal (a) As-welded, (b) Low LMP condition, (c) High LMP condition

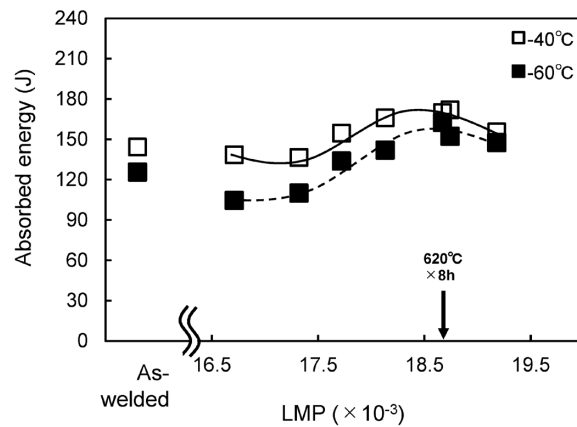
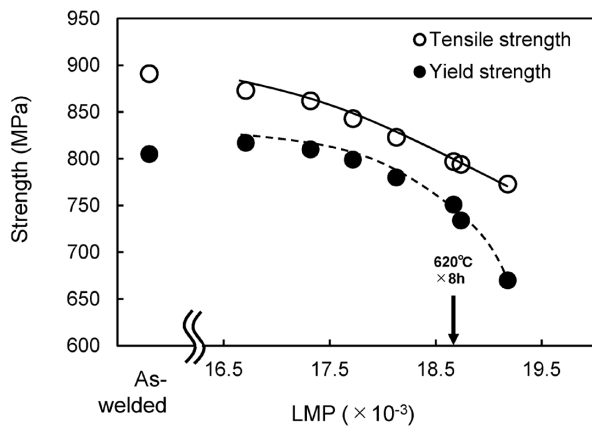


Fig. 8 Relationship between LMP and mechanical property of weld metals in this study

with only a small quantity of carbides other than cementite. Additionally, while some cementite exhibits Ostwald ripening tendencies after PWHT, generally, cementite in the range of 100 to 200 nm predominates. In weld metal where Cr and Mo have been adjusted, the formation and growth of carbides are suppressed, and embrittlement due to carbide-induced precipitation hardening is considered to be minor.

It should be noted that further investigation is necessary regarding these factors in the future.

## 2. Mechanical properties of the optimal composition system for weld metal

Within the composition range of the weld metal presented in Table 1, an investigation was conducted on the relationship between LMP and the mechanical properties of the weld metal. The shielding agent design for SMAW has been optimized to reduce oxygen levels, and the results are depicted in Fig. 8. The tensile strength of the weld metal meets or exceeds 780 MPa even under high LMP conditions. Moreover, regardless of the presence of PWHT, the absorbed energy at  $-40^{\circ}\text{C}$  consistently surpasses that of the conventional material. The embrittlement due to PWHT is minimal, allowing for responsive performance across a broad range of PWHT conditions. It is noteworthy that in SMAW weld metal, including the as-weld specimen, no grain boundary fractures are observed on the fracture surface of the Charpy impact test specimens after PWHT. SMAW for direct current electrode positive (DCEP) with excellent mechanical properties of weld metal of 780 MPa-class steel, has been commercialized as “TRUSTARC™ LB-80LSR.”

## Conclusions

A study has investigated the fracture morphology and microstructure of 780 MPa-class steel weld metal submitted to PWHT, with the aim of establishing design guidelines for achieving excellent notch toughness. The study found that adjusting the Mn content is effective in reducing temper embrittlement under low LMP conditions. Additionally, it identified the fact that adjusting the Cr and Mo content is effective in reducing embrittlement caused by precipitation hardening due to carbide formation/growth after PWHT. Furthermore, the insight was gained that optimizing other alloying additives contributes to the preservation of notch toughness after PWHT by facilitating the reverse transformation of austenite under high LMP conditions. On the basis of the insights gained, a shielded metal arc welding rod for 780 MPa-class steel, TRUSTARC™ LB-80LSR, has been developed, the rod exhibiting excellent notch toughness after PWHT. It is believed that this will contribute to expanding the possibilities of manufacturing in the future.

## References

- 1) Y. Satoh et al. JFE Technical Report. 2020, No.46, pp.70-75.
- 2) Y. Horii et al. Pressure engineering. 1996, Vol.34, No.1, pp.3-7.
- 3) T. Suga et al. Toughness of Weld Metal by MAG Welding Flux-Cored Wire for Low Temperature Service Steel. IIW Doc. XII-1492-97, 1997.
- 4) S. Kano et al. Proceedings of the Welding Structure Symposium. 2017, pp.551-554.
- 5) M. Inomoto et al. Effect of microstructure on fracture behavior of 780 MPa class weld metal submitted to PWHT. IIW Doc. IX-L-1252-2022, 2022.
- 6) H. Hatano et al. Kobe Steel Engineering Reports. 2008, Vol.58, No.1, pp.18-23.

# Effect of Tungsten (W) on Creep Properties of 9Cr-3W-3Co-Nd-B Steel Weld Metals

Hiromi OYAMADA\*<sup>1</sup> • Hideaki TAKAUCHI\*<sup>1</sup> • Shigenobu NANBA\*<sup>2</sup>

\*<sup>1</sup> Welding Process Department, Technical Center, Welding Business

\*<sup>2</sup> Materials Research Laboratory, Technical Development Group

## Abstract

ASME Gr. 93 steel is a heat-resistant steel, in which creep strength is increased by adding elements such as W and B to the conventional 9% Cr ferritic heat-resistant steel. An investigation has been conducted on the effects of W addition on the creep rupture time and metallographic structure of weld metals for Gr.93 steel. The results of the creep rupture test on weld metals with varying additions of W show that creep rupture time increases with the increasing amount of W. Observations of specimens thermally aged at 650°C have confirmed the presence of the Laves phase, suggesting that the increase in creep rupture time is attributable to particle dispersion strengthening by the Laves phase. Increasing the additive amount of W increases the number density of the Laves phase and, furthermore, suppresses the coarsening of the Laves phase during thermal aging. The coarsening rate of the Laves phase during thermal aging has been in good agreement with the calculated value obtained from the theoretical equation for Ostwald ripening. Like  $M_{23}C_6$ , the Laves phase may contribute to the creep strengthening by suppressing the coarsening of the lath size.

## Introduction

In Japan, the 6th Strategic Energy Plan<sup>1)</sup> was approved by the Cabinet in October 2021. As a result of this policy, it is considered that the proportion of electricity generated by coal-fired thermal power will decrease, and the predominant focus in thermal power generation will shift towards co-combustion and dedicated combustion of non-carbon fuels such as ammonia and hydrogen. Since thermal power generation is assumed to function as a regulating power source to supplement the unstable renewable energy supply, the frequency of the startup and shutdown cycle is expected to increase compared with conventional operations, and the thermal fatigue property of boilers is a concern. One of the methods to improve thermal fatigue properties is to enhance the strength of steel and thin out piping. The benefits associated with the increased strength of steel include the reduction of maintenance costs by extending the lifespan of piping.

ASME Grade 93 steel (9Cr-3W-3Co-Nd-B steel) has improved the creep strength and creep rupture ductility of conventional 9Cr ferritic heat-resistant

steel<sup>2)</sup>. Characteristics of this steel grade include the addition of boron to suppress formation of fine-grains in the heat affected zone (HAZ) of welding and improved creep strength. Additionally, tungsten (W) is added to achieve solid-solution strengthening and particle dispersion strengthening with the Laves phase ( $Fe_2W$ )<sup>2)</sup>. The addition of boron is reported by Nako et al.<sup>3)</sup> to contribute to the creep strengthening of weld metal for ASME Grade 92 (9Cr-1.8W-0.5Mo-Nb-V) steel by suppressing the coarsening rate of  $M_{23}C_6$ . Fedoseeva et al. have reported that increasing the W content from 2 mass% to 3 mass% in ASME Grade 92 steel improves its creep strength up to 10,000 hours, but the effect of W on creep strength disappears at 100,000 hours<sup>4)</sup>. However, it is not clear whether the weld metal of Grade 93 steel exhibits a similar trend. This paper focuses on W and reports the results of investigation into the way in which W addition to Grade 93 steel weld metal affects the creep rupture time and metallographic structure.

## 1. Experimental method

### 1.1 Test Material

Weld metals were produced using a covered electrode having a core diameter of  $\phi 4.0$  mm. For two types of weld metal with different compositions (A and B), specimens were prepared by varying the W content within the range of 1.6 to 2.8 mass% for each composition. The welding conditions were described as follows, polarity: direct current electrode positive (DCEP), heat input: 1.5 to 2.5 kJ/mm. The produced weld metals were subjected to post-weld heat treatment (PWHT) at 760°C for 4 hours. The chemical compositions of the weld metals are shown in **Table 1**.

### 1.2 Creep rupture test

The all-weld-metal creep specimens were taken from the center of weld metals in the longitudinal direction. The round bar specimens have a nominal diameter of  $\phi 6$  mm, and the nominal gauge length of 30 mm. The test temperature was set at 650°C, with stress conditions of 170 MPa and 80 MPa.

Table 1 Chemical compositions in weld metals

Specimen mark	W	C	Si	Mn	Ni	Cr	V	Co	(mass%)		
									B	Nb	N
2.8W-A	2.8	0.1	0.3 ~0.4	0.5	0.5	9	0.2	3	0.007 ~0.012	0.05 ~0.06	0.02
1.6W-A	1.6										
2.7W-B	2.7	0.1	0.3	0.5	0.5	9	0.2	3	0.004	0.08	-
1.7W-B	1.7										

### 1.3 Metallographic observation

The field emission scanning electron microscope (hereinafter referred to as “FE-SEM”) was used to evaluate the microstructure morphology of the weld metal. The observation positions were set to correspond to the reheated zone along the axis of the creep specimens of the weld metal. Elemental mapping data was obtained using Energy Dispersive X-ray spectroscopy (hereinafter referred to as “EDX”) to identify the precipitates.

## 2. Experimental results and discussion

### 2.1 Effect of W on creep rupture time

Fig. 1 shows the relationship between the creep rupture time and the W content in the weld metal under various stress conditions. Regardless of the stress conditions, increasing W tended to improve the creep rupture time. According to Kimura et al.<sup>5)</sup>, simultaneous addition of W and Co in 15Cr ferritic heat-resistant steel enhances creep strength, and the contributing factor may be precipitates. Morimoto et al.<sup>6)</sup> state that when the W content in the weld metal is between 1.6 to 1.7 mass%, the Laves phase precipitates during creep rupture testing at 600°C (after approximately 100 to 1,000 hours). In this study, microstructure observations were conducted considering the possibility that the Laves phase may have an impact on creep rupture time.

### 2.2 Effect of W on microstructure of weld metals

The microstructures of the weld metal were observed after PWHT and subsequent thermal aging at 650°C for 3,000 to 20,000 hours. It should be noted that, due to the absence of applied stress, the thermal aging causes diffusion to progress less readily compared with the creep rupture test. However, considering the cost of the tests, it was adopted for the purpose of understanding the trends. Fig. 2 shows the backscattered electron image taken by FE-SEM, and Fig. 3 shows the EDX elemental mapping images of 2.8W-A after 5,000 hours of

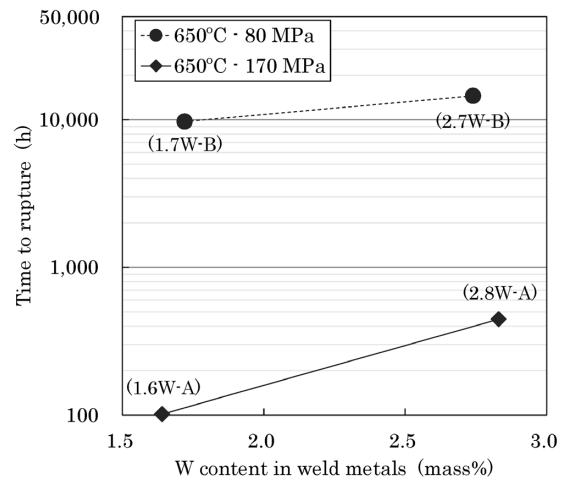


Fig.1 Relationship between time to rupture and W content in weld metals

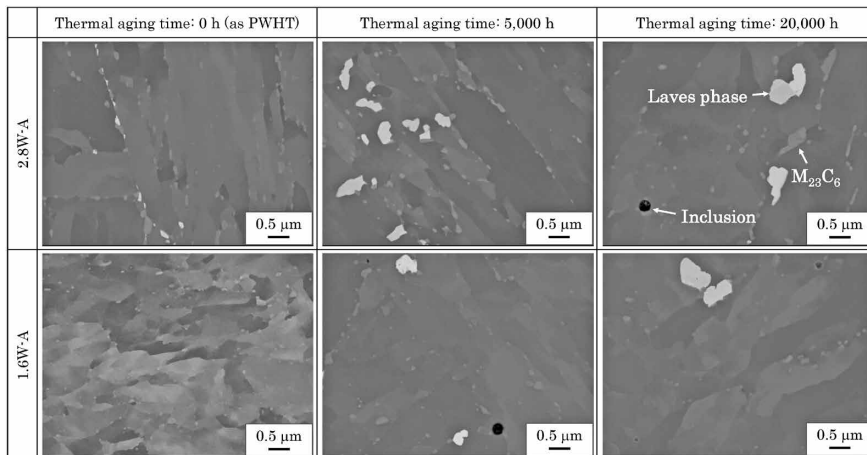


Fig.2 Backscattered electron images of weld metals

thermal aging. In FE-SEM observation, two types of precipitates, white and gray in color, were observed. The precipitation mainly occurred at the locations identified as lath boundaries within the martensite structure.

No white precipitates were observed after PWHT of 1.6W-A, but they were confirmed after 5,000 hours of thermal aging. However, the number density of these precipitates is significantly lower compared with 2.8W-A. The white precipitates observed in 2.8W-A were nearly elliptical after PWHT, and they grew with increasing thermal aging time. On the other hand, the grain size of the gray precipitates was smaller than that of the white precipitates and the shape is closer to a circle or ellipse. From the EDX elemental mapping, it has been confirmed that W is concentrated in the white precipitates, while Cr is concentrated in the gray precipitates.

The precipitates formed in equilibrium at 760°C and 650°C based on the composition shown in Table 1 were calculated by means of the thermodynamic calculation software, Thermo-Calc (Database: TCFE9). The results are presented in Table 2. The calculated phases include  $M_{23}C_6$ , the Laves phase, MX,  $Cr_2B$ , and Z phase. The particle diameter of MX in 9Cr ferritic weld metal is reported to be on the order of several tens of nanometers<sup>7)</sup>, the amount of  $Cr_2B$  is low in equilibrium, and Z phase is said to be formed during long-term thermal aging exceeding several tens of thousands of hours. Based on these factors, most of the precipitates seen in

Fig. 2 are  $M_{23}C_6$  and the Laves phase. According to these results, it is concluded that the white precipitates are the Laves phase, while the gray precipitates are Cr-dominant  $M_{23}C_6$ . Subsequent discussions focus on evaluating the Laves phase, where the effect of W is more prominently observed. The black inclusions present in some specimens are oxide compounds generated during the shielded metal arc welding.

Fig. 4 shows the average equivalent circle radius and number density of the Laves phase with thermal aging time, obtained from Fig. 2. In the case of 1.6W-A, no Laves phase has been observed after PWHT, which is consistent with the results from Thermo-Calc calculations. The equivalent circle radius of the Laves phase tends to increase with the progression of thermal aging for both 2.8W-A and 1.6W-A. However, in the case of 2.8W-A, the coarsening stagnates at around 150 nm after thermal aging for more than 10,000 hours. In contrast, the coarsening of 1.6W-A progresses to approximately 200 nm after thermal aging for 20,000 hours. The number density of the Laves phase increases during relatively short-term thermal aging after PWHT and then decreases until 20,000 hours of thermal aging. At any thermal aging time, the number density of the Laves phase of 2.8W-A is greater than that of 1.6W-A.

The formula for the creep strain rate  $\dot{\epsilon}$  of particle dispersion strengthening materials is known to be as follows<sup>8)</sup>:

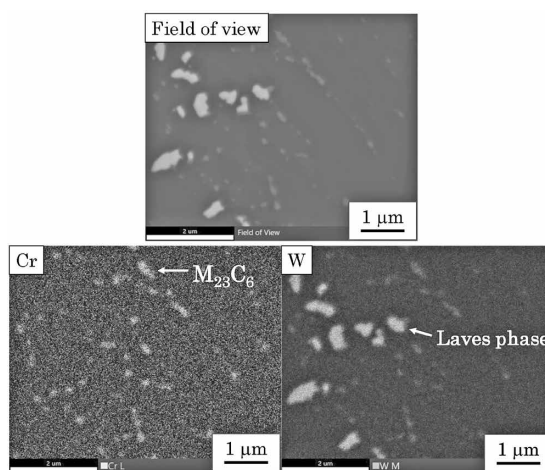


Fig.3 EDX mapping images of 2.8W-A after thermal aging for 5,000 h

Table 2 Volume fraction of precipitates at PWHT temp. and thermal aging temp. calculated by Thermo-Calc with TCFE9 database

Specimen mark	Calculated temp.	(vol.%)				
		$M_{23}C_6$	Laves phase	MX	$Cr_2B$	Z phase
2.8W-A	760°C [PWHT]	1.49	0.60	0.03	0.10	0.21
	650°C [Aging]	1.55	1.86	0.00	0.10	0.25
1.6W-A	760°C [PWHT]	1.31	0.00	0.19	0.18	0.00
	650°C [Aging]	1.42	0.65	0.03	0.18	0.24

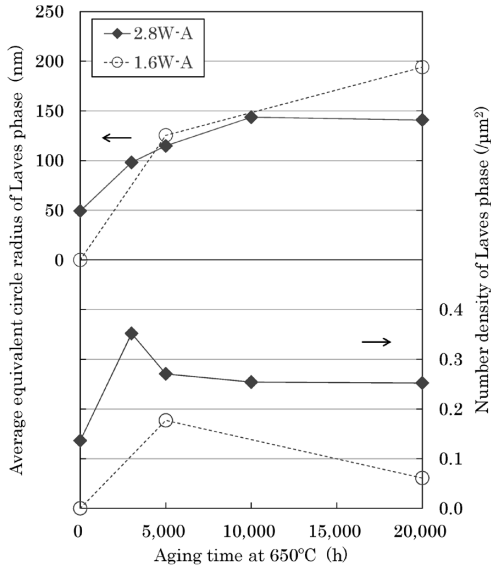


Fig.4 Change in average equivalent circle radius and number density of Laves phase with thermal aging

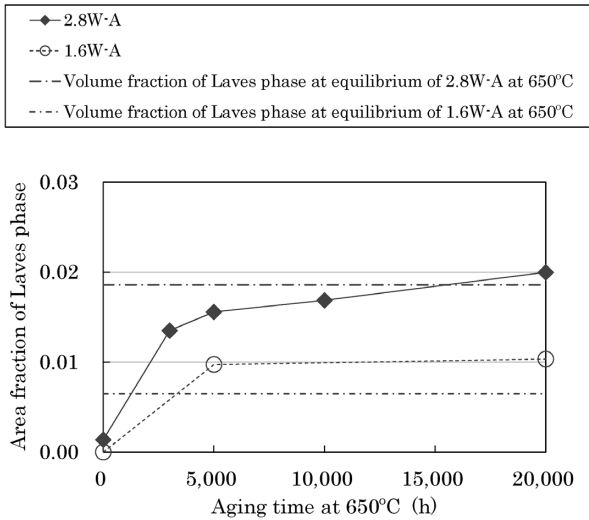


Fig.5 Change in amount of Laves phase with thermal aging

$$\dot{\epsilon} = \dot{\epsilon}_0 \left( \frac{\sigma - \sigma_{th}}{E} \right)^m \frac{D}{b^2} \quad \dots \quad (1)$$

wherein,  $D$  is the diffusion coefficient,  $E$  is the Young's modulus,  $b$  is the length of the Burgers vector, and the coefficients  $\dot{\epsilon}_0$  and the effective stress exponent  $m$  are material constants.  $\sigma_{th}$  is the threshold stress, below which the creep strain rate is assumed to be zero, and is independent of the external stress  $\sigma$ .

The threshold stress  $\sigma_{th}$  is known to be inversely proportional to the interparticle spacing, and the creep strength is improved by decreasing the interparticle spacing. It is inferred that increasing the W content results in a higher number density of the Laves phase and a smaller interparticle spacing, thereby increasing the creep rupture time.

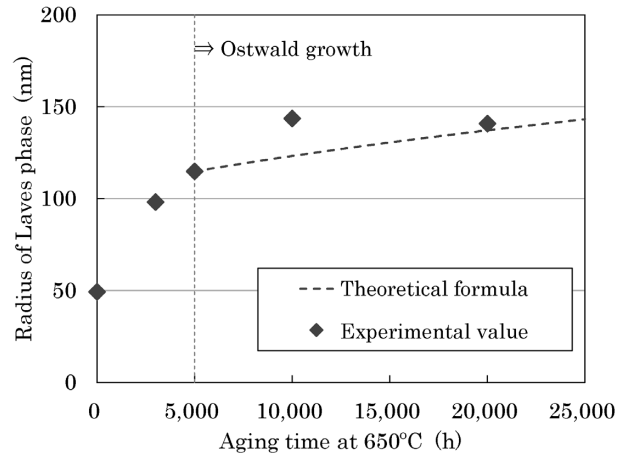


Fig.6 Comparison of theoretical formula and experimental values of Ostwald ripening in the Laves phase

### 2.3 Thermodynamic considerations

Fig. 5 shows the change in the precipitate amount of the Laves phase with aging time measured through FE-SEM observations. The dashed lines in Fig. 5 represent the volume fraction of the Laves phase in equilibrium at 650°C of 2.8W-A and 1.6W-A, as indicated in Table 2. For both 2.8W-A and 1.6W-A, the precipitate amount of the Laves phase reaches equilibrium after approximately 5,000 hours or more of thermal aging. Subsequently, the Laves phase became larger and the number density decreased. It is suggested that the Ostwald ripening of the Laves phase is occurring. The theoretical formula for the Ostwald ripening is represented by the following equation:

$$r^3 - r_0^3 = kt \quad \dots \quad (2)$$

$$k = \frac{8}{9} \frac{\sigma V^P}{\sum_i \frac{(x_i^P - x_i^M)^2}{x_i^M D_i / RT}} \quad \dots \quad (3)$$

wherein,  $r$  and  $r_0$  are the particle radii of the precipitates at any point during thermal aging and at the beginning of Ostwald ripening, respectively,  $t$  is the thermal aging time,  $\sigma$  is the interface energy between the matrix and precipitates,  $D_i$  is the diffusion coefficient of solute atom  $i$  in the matrix,  $V^P$  is the molar volume of precipitates,  $x_i^P$  is the concentration of solute atom  $i$  in the precipitates,  $x_i^M$  is the concentration of solute atom  $i$  in the matrix,  $R$  is the gas constant, and  $T$  is the absolute temperature.

Fig. 6 compares the Ostwald ripening process of the Laves phase derived from the theoretical formula to the experimental values. As mentioned above, the time for the precipitate amount of the Laves phase to reach equilibrium is approximately

5,000 hours. Hence, the theoretical formula has been calculated assuming that Ostwald ripening begins at the point when the thermal aging time reaches 5,000 hours. The theoretical formula shows excellent agreement with the experimental values. The average equivalent circle radius of the Laves phase is approximately 150 nm after thermal aging for 10,000 hours at 650°C, as determined from experimental values. The coarsening rate of the Laves phase during thermal aging does not always coincide with the coarsening rate of the Laves phase during creep rupture test because the creep rupture specimen has been applied stress. However, it is inferred that the particle radius of the Laves phase coarsened to more than about 150 nm under the condition of the creep rupture test time exceeding 10,000 h. Fedoseeva et al. reported that the dislocation pinning force of the Laves phase in 9Cr-3W steel significantly decreases when the creep rupture time exceeded approximately 2,000 hours at 650°C and 100-220 MPa<sup>4)</sup>. However, in this study, it is demonstrated that an increase in W content contributes to the improvement of creep rupture time even when the rupture time is 10,000 to 20,000 hours. This suggests that the Laves phase is effective in increasing the creep rupture time of the weld metal even if it coarsens to a radius of more than 150 nm. As the mechanisms by which precipitates contribute to the creep strengthening of ferritic heat-resistant steel, dislocation pinning, suppression of martensitic lath coarsening, and strengthening of grain boundaries are mentioned. The contribution of the Laves phase to the dislocation pinning may be small, and the MX which exists finely in the grain is more effective for dislocation pinning than the Laves phase which exists in the grain boundary. It is suggested that the coarsening of martensite lath during creep was suppressed by the Laves phase on grain boundaries which may be martensite lath.  $M_{23}C_6$  is known to exist along lath boundaries as well as the Laves phase and is effective in inhibiting the coarsening of the martensite microstructure<sup>9)</sup>, and in the case of 2.8W-A, the addition of W may have enhanced the effect by increasing the precipitates formed on the grain boundary.

## Conclusions

The effect of W addition on creep rupture time and microstructure for Gr.93 steel weld metal was investigated. The main results can be summarized as follows:

1. The creep rupture time at 650°C improved with increasing W content in the weld metal regardless of the stress condition.
2. The average equivalent circle radius of the Laves phase coarsens with the progress of thermal aging at 650°C. After 20,000 hours of aging, the average equivalent circle radius of the Laves phase is around 150 nm for W content of 2.8 mass%, while it grows to approximately 200 nm for W content of 1.6 mass%. The number density of the Laves phase increases throughout the period of 3,000 and 5,000 hours of thermal aging after PWHT, subsequently decreasing.
3. The creep rupture time of 2.8 mass% W is higher than that of 1.6 mass% W, and this is considered to be due to the high number density and narrow particle spacing of the Laves phase.
4. The formation of the Laves phase generally reaches an equilibrium amount after thermal aging for approximately 5,000 hours. Subsequently, coarsening of the Laves phase and the decrease of the number density are considered to cause Ostwald ripening. The experimental values and theoretical formula of Ostwald ripening exhibit good agreement.
5. Even under conditions where the creep rupture time is around 10,000 hours, the addition of W remains effective in increasing the creep rupture time. The Laves phase, is considered to be effective for creep strengthening, even if it coarsens to about 300 nm. Similar to  $M_{23}C_6$ , the Laves phase may enhance creep rupture time by suppressing the coarsening of lath size.

## References

- 1) Ministry of Economy, Trade and Industry. The 6th Strategic Energy Plan. October 2021 [https://www.enecho.meti.go.jp/category/others/basic\\_plan/](https://www.enecho.meti.go.jp/category/others/basic_plan/), (reference on November 30, 2022).
- 2) A. Iseda et al. "The Thermal and Nuclear Power Generation Convention Collected Works." Thermal and Nuclear Power Energy Society, 2016, Vol.12, pp.49-55.
- 3) H. Nako et al. "Preprints of the National Meeting of JWS.," Japan Welding Society, 2017, p.92.
- 4) A. Fedoseeva et al. "Metals." 2017, Vol.7, Issue 12, Article 573.
- 5) K. Kimura et al. "ISIJ International." 2001, Vol.41, pp.S121-S125.
- 6) H. Morimoto et al. "Quarterly Journal of the Japan Welding Society." 1998, Vol.16, No.4, pp.512-521.
- 7) Y. Banno et al. "Journal of the Japan Welding Society." 2016, Vol.85, No.6, pp.581-587.
- 8) K. Maruyama et al. "Kouonkyodo no Zairyokagaku (Revised Edition: Materials Science of High-Temperature Strength.) (in Japanese)" Revised 1st edition, Uchida Rokakuho, 2002, p.177.
- 9) F. Abe. "Bulletin of The Iron and Steel Institute of Japan (Ferrum)." 2012, Vol.17, No.8, pp.560-564.

# Slag Control Technology to Improve Electrodeposition Coatability of Arc Weld Joints

Hikaru KINASHI\*1 • Yue SUN\*2 • Kazuya IKAI\*1

\*1 Welding Process Department, Technical Center, Welding Business

\*2 Welding Process Department, Technical Center, Welding Business (currently Finance and Accounting Department)

## Abstract

*To improve the durability and reliability of arc weld joints of automobile chassis parts, a welding consumable has been developed that can improve the electrodeposition coatability of weld bead by adjusting the deoxidizing elements in the welding wire. In this paper, the lap fillet weld joints were prepared using conventional and developed wire, and the surface and cross-section of weld slag were observed to investigate the relationship between the oxide state and electrodeposition coating properties. It has been confirmed that the composition of the major oxides in the weld slag of the developed wire is multiple Mn-based oxides, rather than Si-Mn composite oxides. In addition, it has been confirmed that the constitutional state of the Mn-based oxides in the welding slag has changed due to the dilution effect of the base steel plate, and that these factors also affected the electrodeposition coatability.*

## Introduction

Automobile chassis components, including suspension systems, commonly utilize steel materials. These materials must fulfill the concurrent requirements of high strength, rigidity, fatigue resistance, and corrosion resistance. As for corrosion resistance, there is a need for enhanced performance, given exposure to severe corrosion environments like physical damage from road debris during driving, salt-laden air in coastal regions, and de-icing agents in cold climates.

In practice, a certain level of quality is ensured through measures like the partial adoption of galvanized steel sheets and rust prevention treatments<sup>1)</sup>, including electrodeposition coating for the entire surface of the components.

For joining automobile chassis components, gas shield arc welding is commonly employed. The welding wire used in gas shield arc welding contains deoxidizing elements such as Si and Mn. These elements react with oxygen dissolved in the molten metal and float up to form welding slag on the bead surfaces, resulting in a sound weld joint. On the other hand, since the welding slag is primarily composed of insulating oxides, mainly silicon oxide, the presence of these on the bead surface prevents the formation of coating in the

electrodeposition coating process after welding. In corrosive environments, it is known that areas where electrodeposition coating has not formed can serve as the starting points for rusting. The results of cyclic corrosion testing conducted on test pieces with lap welding joints created using pulse MIG welding after electrodeposition coating are presented in Fig. 1. It is observed that no electrodeposition coating has formed on the residual slag on the weld joint bead, and corrosion has begun from those areas.

To improve the condition of the electrodeposition coating of the weld joint, it is preferable to remove slag as much as possible beforehand. However, manual slag removal is limited due to its high labor intensity leading to a decrease in production efficiency. Additionally, methods such as shot blasting are available for physically removing slag; however, they not only incur increased costs but also present technological challenges, making their application difficult when it comes to complex shapes. Technology has been proposed for controlling slag during welding because it acts as an inhibiting factor for electrodeposition coating. Some approaches involve welding consumables and the welding process. For example, it has been proposed to deliberately add sulfur (S) to agglomerate welding slag or use processes that suppress the generation of welding slag as much as possible, while allowing the generated slag to agglomerate at the bead toe<sup>2),3)</sup>. Furthermore, a past report indicates that improving the electrodeposition coatability can be achieved by reducing the amounts of Si and Mn in the welding wire<sup>4)</sup>. The present authors have adjusted the balance of deoxidizing element additions in the welding wire, thereby altering the morphology

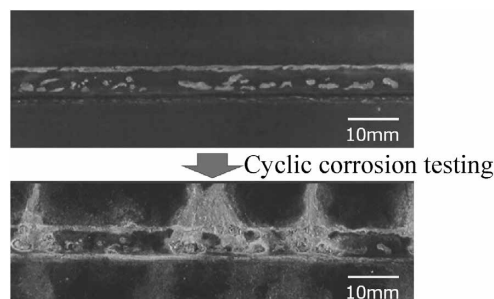


Fig.1 Appearance of weld bead before and after cyclic corrosion testing

and electrical properties of the welding slag. This development allowed for the electrodeposition coating to be formed even in the presence of residual slag in the weld joint. This paper reports the results of comparing the electrodeposition coatability of weld joints using this welding wire with those using the conventional pulse MIG welding wire and also reports on the composition of the welding slag and the internal structure of the oxide in the slag that improves electrodeposition coatability.

## 1. Test Method

### 1.1 Test Specimens

**Table 1** shows an example of the chemical composition of the welding wire used for the evaluation. As a comparison wire, a pulse MIG welding wire (JIS Z 3312 G 49 A 2 M 16) with a proven track record in welding automobile chassis components was used. The distinctive feature of the developed wire's chemical composition is its extremely low Si content and high content of Mn and Ti. Testing was conducted on a 440 MPa-class hot-rolled steel sheet (SPH440) and a cold-rolled steel sheet (SPCC). **Table 2** presents an example of the chemical compositions of the steel sheets.

### 1.2 Preparation of weld joint

The welding conditions are presented in **Table 3**. Each steel sheet, with a thickness of 2.3 mm, a width of 50 mm, and a length of 200 mm, were fixed by

a jig as shown in **Fig. 2**. Three sets of lap welding joints were created. The welding process utilized a Digital Power Supply P500L and a welding robot, FD-V8, both manufactured by Daihen Ltd. Pulse MIG welding was conducted under an 80% Ar-20% CO<sub>2</sub> mixed gas. Two sets of the prepared test pieces underwent electrodeposition coating, while the one remaining set was used for the analysis of various slag characteristics.

### 1.3 Electrodeposition coating

Enlarged photographs were taken of the central part of the bead immediately after welding, and the distribution of slag was noted and entered into comparison for each welding wire and steel sheet. Subsequently, as a pretreatment for electrodeposition coating, the test pieces underwent cleaning, degreasing, surface adjustment and chemical treatment. As a final step, black cationic electrodeposition coating was applied. The target coating thickness was 20 μm.

### 1.4 Composition and phase analyses of welding slag

From the vicinity of the bead center (the steady part of the bead) of the prepared test pieces, samples for composition analysis were collected through electrical discharge machining. To obtain average composition information about the slag, element analysis was initially conducted using a Scanning Electron Microscope and Energy Dispersive X-ray Spectrometry (SEM-EDS) from the surface side of

**Table 1** Chemical composition of welding wires (mass%)

	C	Si	Mn	P	S	Ti
Conventional wire	0.05	0.75	1.25	0.010	0.004	< 0.01
Developed wire (Low Si wire)	0.05	0.10	1.96	0.010	0.006	Add.

**Table 2** Chemical composition of steel sheets (mass%)

	C	Si	Mn	P	S	Ti
440MPa steel sheet* (SPH440)	0.12	0.02	0.88	0.014	0.004	< 0.01
Mild steel sheet (SPCC)	0.02	0.01	0.11	0.017	0.002	< 0.01

\*Hot rolled sheet.

**Table 3** Welding conditions

Robot	FD-V8 (DAIHEN Corporation)
Power supply	Welbee P500L (DAIHEN Corporation)
Welding method	Pulse MAG
Shielding gas	80%Ar-20%CO <sub>2</sub>
Base metal	440 MPa steel sheet (2.3 mmT×50 mmW×200 mmL)
Current-voltage	200 A-24 V
Travel speed	80 cm/min
Travel angle	Perpendicular
Contact-tip to work distance	15 mm

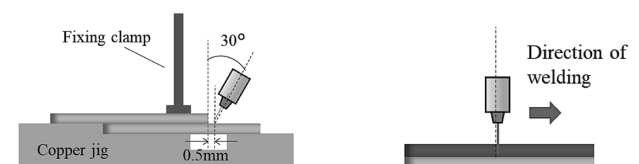


**Fig.2** Welding position

the slag. Subsequently, cross-sectional observations of the element distribution in the depth direction of the slag were carried out. The test pieces were embedded in resin and polished. Focusing on the slag location on the upper side of the sheet, where the slag was thickest in the bead cross-section, backscattered electron image observation was performed. For the developed wire, element mapping was conducted using an Electron Probe Micro Analyzer (EPMA). Furthermore, using the multivariate image analysis software, COMPASS, from Thermo Fisher Scientific Inc., phase separation analysis was performed by extracting individual oxide phases with distinctive spectra from the element spectra obtained through EDS<sup>5)</sup>.

### 1.5 Equilibrium state calculation of multi-component oxide

To understand how the composition differences in the welding wire affect the preferential formation of oxide types in the molten slag, equilibrium state calculations of oxides were performed using the thermodynamics equilibrium calculation software FactSage 8.1. In order to simplify the complex relationships among oxides, the calculation was limited to four elements—Si, Mn, Ti, and Fe. The Gibbs energy minimization method was applied to calculate the amount of oxide formed in each temperature range using the thermodynamics data base FToxid. To determine the mass ratio (coefficient) of each oxide in the slag, the coefficients for each oxide were calculated on the basis of the EDS analysis results from the slag surfaces, while ensuring that the sum of the coefficients for all oxides equaled 100.

## 2. Test results and considerations

### 2.1 Results of welding and electrodeposition coating

An example of the observed slag behavior on the molten pool during welding is shown in Fig. 3. The welding slag from the conventional wire exhibits a tendency to agglomerate on the molten pool. On the other hand, the welding slag from the developed wire shows suppressed agglomeration on the molten pool and a thin formation on the surface towards the rear of the molten pool. Photos showing the bead appearance after welding and after electrodeposition coating are presented in Fig. 4. The central part of the photo represents the welding bead, with the upper sheet above and the lower sheet below. With the conventional wire, glossy welding slag has been formed on the bead surfaces for both the SPH440

and SPCC steel sheets. In areas where this slag remains, no electrodeposition coating is formed. In contrast, the bead surfaces with the developed wire display a non-glossy dark brown slag that spread uniformly, regardless of the type of steel sheet. Although some areas of the welding slag on the upper sheet side allow no electrodeposition coating to form, the overall area without coating has been significantly reduced compared with the area where conventional wire was used. Focusing on the differences in steel sheets, the SPCC steel sheet exhibits superior electrodeposition coatability for both the conventional and developed wire.

### 2.2 Observation and composition analysis results for slag surface

The slag formed on the welding beads has been observed as-is on the surfaces using SEM, and composition analysis has been conducted using EDS. Both the conventional wire and the developed wire have been analyzed in the slag near the top sheet side. The positions for the composition analysis of the welding slag using the SPH440 steel sheet are shown in Fig. 5. The square frames indicate the analysis positions, and the circular frames indicate the analysis areas. In the slag from the conventional wire, charge-up traces are observed at the electron beam irradiation positions in the SEM image, suggesting relatively low conductivity. On the other hand, no charge-up traces were observed in the

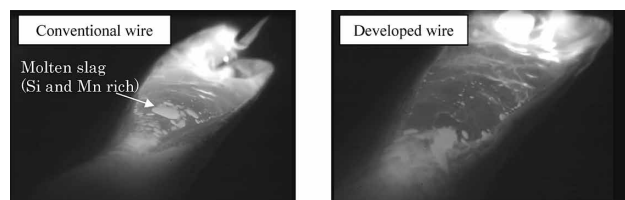


Fig.3 Observation image of molten pool during arc welding (SPH440)

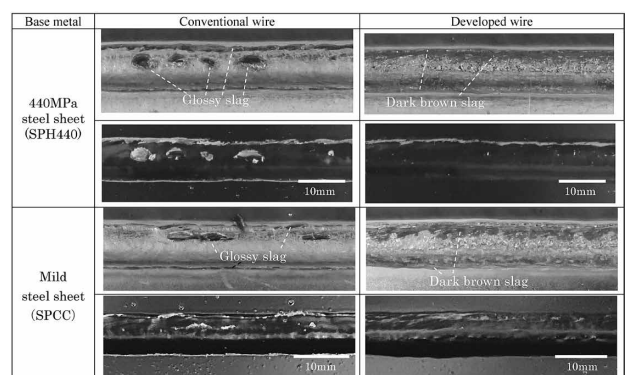


Fig.4 Weld bead appearance (Top: as-welded, Bottom: electrodeposition coated)

brown slag part where the developed wire was used. Next, the EDS analysis results for the welding slag formed using the SPH440 and SPCC steel sheets are shown in Fig. 6. In both the steel sheets, the proportion of Si in the entire slag is higher for the conventional wire. For the developed wire, the proportion of Si in the entire area of slag is smaller, aligning with the intended result that the welding slag is mainly composed of Mn and Ti oxides. Additionally, traces of Fe and minor amounts of Al are detected, which are believed to be inevitably detected in the base metal steel sheet.

### 2.3 Observation and phase analysis results for slag cross section

#### 2.3.1 Welding slag of conventional wire

Fig. 7 shows the backscattered electron images of the bead cross-sections of the SPH440 steel sheet welded using the conventional wire. The square frames in the figure indicate the locations for slag observation. The thickness of the slag formed in agglomeration near the top sheet side is approximately 200 μm locally. Three morphologies of welding slag are identified: dark areas, bright

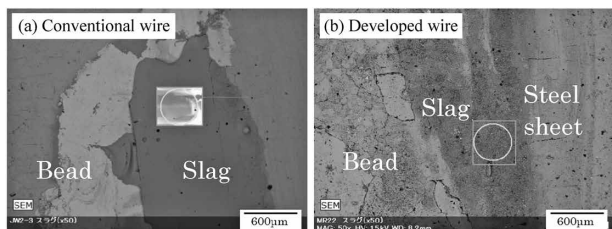


Fig.5 EDS Analysis position (SPH440)

areas, and areas exhibiting distinctive patterns. The results of the oxide phase analysis conducted using COMPASS are presented in Fig. 8. The elements listed in parentheses represent the elements with a higher mass ratio in a phase, in the order from left to right. The slag formed with conventional wire is composed of three main oxide phases: Phase ①, consisting of Mn and Si; Phase ②, consisting of Si and Fe; and Phase ③, consisting of Mn, Si, and Fe. Each of these phases corresponds distinctly to the results of the backscattered electron image observation, clearly existing in separate entities. Consistent with previous findings, it has been confirmed that the glossy slag formed with conventional wire is predominantly composed of oxides, primarily Si and Mn based, throughout the entire region.

#### 2.3.2 Welding slag of developed wire

The developed wire has been used to weld the SPH440 steel sheets. Fig. 9 shows the backscattered electron image of the slag cross-section and

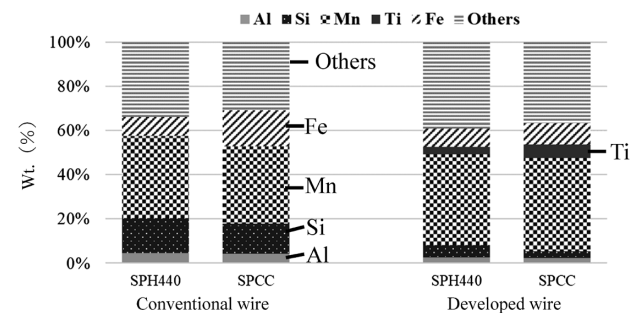


Fig.6 Result of EDS analysis

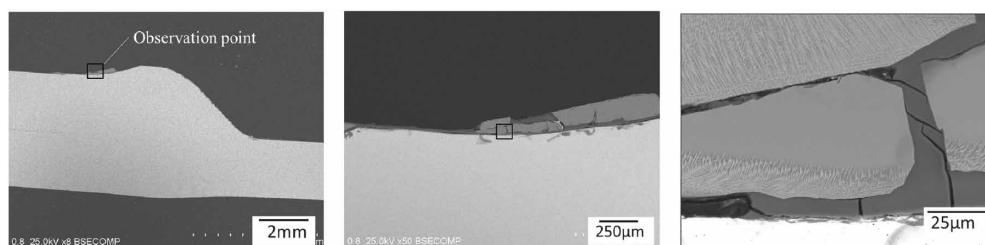


Fig.7 Slag observation point (frame) and backscattered electron (BSE) image (conventional wire, SPH440)

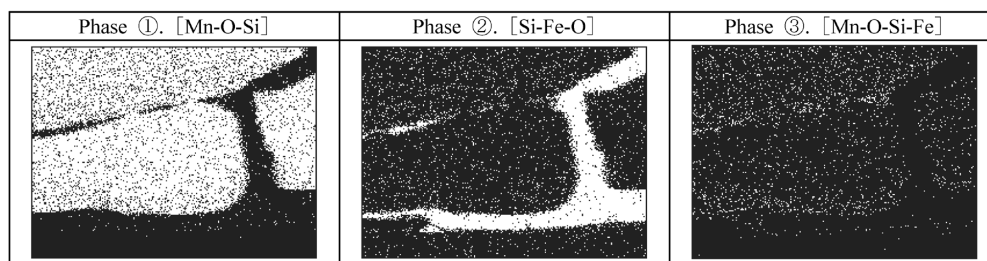


Fig.8 Results of phase analysis [chemical composition] (conventional wire, SPH440)

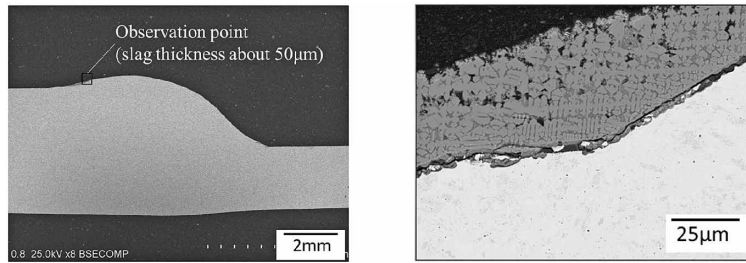


Fig.9 Slag observation point (frame) and BSE image (developed wire, SPH440)

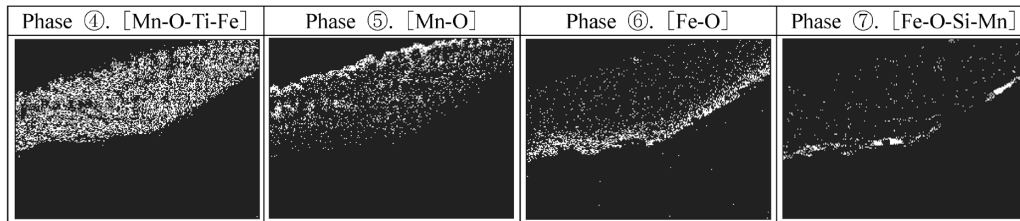


Fig.10 Results of phase analysis [chemical composition] (developed wire, SPH440)

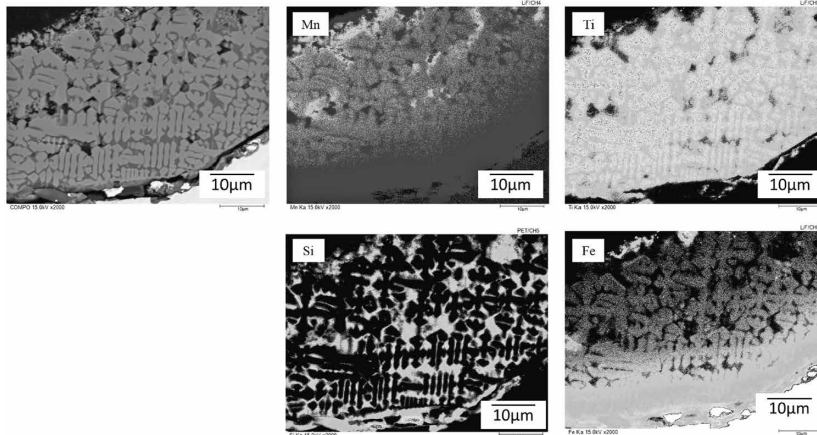


Fig.11 Results of EPMA analysis [chemical composition] (developed wire, SPH440)

enlarged images of the observation points within the square frame. The slag tends to form thickly on the upper side of the sheet, similar to the results of using conventional wire; however, its thickness has been confirmed to be a maximum of about 100  $\mu\text{m}$ , which is thinner than with conventional wire. The morphology of the slag exhibits a dendrite-like structure, a feature not observed in the case of conventional wire. Fig.10 presents the results of oxide phase analysis using COMPASS on the slag formed on the SPH440 steel sheet. The slag is composed of four types of oxide phases: a phase consisting of Mn, Ti, and Fe (Phase ④); Mn oxide phase (Phase ⑤); iron oxide phase (Phase ⑥); and an oxide phase composed of Fe, Si, and Mn (Phase ⑦). Phase ④ is formed throughout the depth direction, Phase ⑤ is formed near the surface of the slag, and Phases ⑥ and ⑦ are distributed on the interface between the slag and the base metal. Unlike the observation results for conventional wire, these

phases are not clearly separated but exist in an overlapping manner. The mapping results of the slag part using EPMA are shown in Fig.11. In the areas where dendrite-like crystalline structures appear bright in the backscattered electron image, mainly Mn, Ti, and Fe are condensed, while darker areas primarily contain condensed Si.

### 2.3.3 Effect of steel sheet composition on welding slag

The effect of the steel sheet composition on welding slag has been examined using the developed wire. Fig.12 shows the cross-sectional backscattered electron image of the welding slag on the SPCC steel sheet, welded using the developed wire, and an enlarged image of the observation points within the square frame. Similar to the SPH440 steel, there is a tendency for the slag to form thickly on the upper side of the sheet, but its

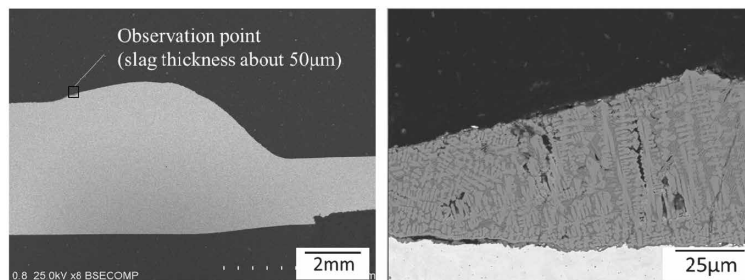


Fig.12 Slag observation point (frame) and BSE image (developed wire, SPCC)

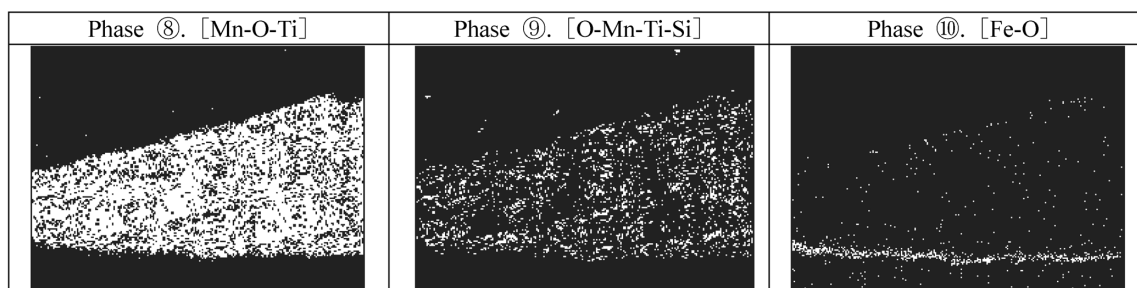


Fig.13 Results of phase analysis [chemical composition] (developed wire, SPCC)

thickness has been confirmed to be a maximum of about 50  $\mu\text{m}$ , and the slag exhibited a dendrite-like morphology on the SPCC steel sheet as well. Fig.13 presents the results of oxide phase analysis using COMPASS for the slag formed on the SPCC steel sheet. The slag is composed of three major phases, with a notably high ratio of oxide phase consisting of Mn and Ti (Phase⑧) and oxide phase consisting of Mn, Ti, and Si (Phase⑨). Additionally, iron oxide phase (Phase ⑩) is observed near the interface with the base metal. In the SPCC steel sheet, as in the SPH440 steel sheet, the main component of the slag is oxide composed of Mn and Ti.

In Fig.10, the surface condensation layer of Mn oxide observed in the SPH440 steel sheet is not observed on the SPCC steel sheet. This suggests that the significantly lower amount of Mn in the SPCC steel sheet, as compared with the SPH440 steel sheet, may be influencing this outcome.

### 2.3.4 Effect of welding slag thickness on electrodeposition coatability

To assess the effect of slag thickness on the state of electrodeposition coating, observations have been conducted on the slag cross-section after electrodeposition coating. Fig.14 shows the SEM observation results near the slag for the SPH440 steel sheet welded with the developed wire. Electrodeposition coating has been formed up to a slag thickness of about 40-50  $\mu\text{m}$ , but in the areas where the slag is thicker, no electrodeposition coating has been observed. This implies

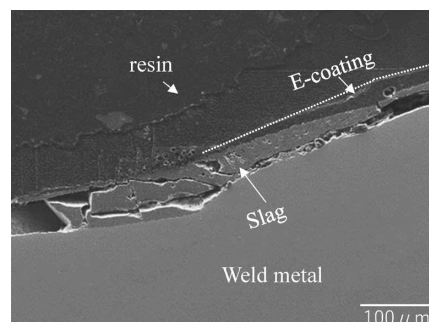


Fig.14 SEM image of weld slag (developed wire, SPH440) after electrodeposition coating)

that reducing slag thickness by suppressing agglomeration may be effective in improving electrodeposition coatability.

### 2.4 Structure prediction of multi-component oxide by equilibrium state calculation

The results of the equilibrium state oxide calculations for both conventional wire and developed wire are presented in Fig.15. The vertical axis represents the mass fraction of oxides, while the horizontal axis represents the temperature. In the case of the conventional wire, as the temperature decreases from 1800 $^{\circ}\text{C}$  to 1200 $^{\circ}\text{C}$ , the molten slag gradually disappears. This means that  $\text{MnFe}_2\text{O}_4$  begins to form initially, followed by the formation of Si-Mn composite oxides with Olivine structure, such as  $\text{Mn}_2\text{SiO}_4$  and  $\text{MnSiO}_3$  (Rhodonite). Particularly near room temperature, the proportion of  $\text{Mn}_2\text{SiO}_4$ , a composite oxide of Si and Mn, becomes significant.

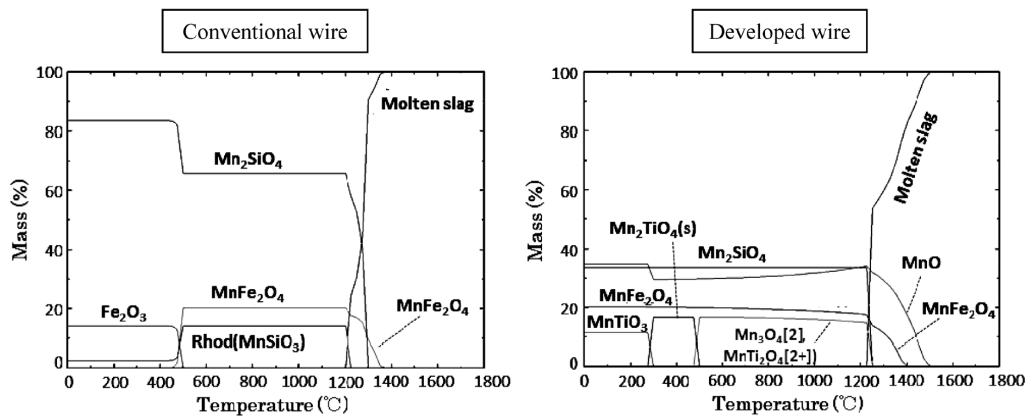


Fig.15 Oxide equilibrium state (effect of temperature on mass percent)

Previous reports have suggested that in the annealing environment of steel sheets with Si and Mn additions, Si and Mn can mutually enhance each other's oxidation reactions, promoting the reduction of iron oxides<sup>6)</sup>. It is considered that, even in the deoxidation process during slag formation in arc welding, mutual oxidation reactions (formation of molten slag) are promoted. Moreover, composite oxides of Si and Mn, such as  $Mn_2SiO_4$  and  $MnSiO_3$ , have lower melting points than composite oxides of Fe and Ti with Mn. As shown in Fig. 3, these Si-Mn composite oxides are likely to reside easily in the molten pool's rearward direction and may persist as thick, large residues during solidification.

Furthermore, the calculation results indicate that  $Mn_2SiO_4$ , an insulating composite oxide of Si and Mn, remains stable on the bead surfaces up to near room temperature after being formed from the molten slag. It is suggested that the preferential formation of these low-conductivity composite oxides during welding, coupled with their local growth through agglomeration, hinders the formation of electrodeposition coating.

On the other hand, in the calculation results for the components of the developed wire, MnO is first formed during the cooling process from the high-temperature side. Subsequently, a composite oxide of Mn and Fe with a spinel structure is formed, followed by the sequential formation of composite oxides with Olivine structure containing Si and Mn, as well as composite oxide of Mn and Ti. Among these, MnO is considered to correspond to the oxide represented by Phase ⑤ in the phase analysis shown in Fig.10. In light of the previous observations of slag cross-sections, it is inferred that in the developed wire, MnO (Monoxide) with higher melting point precipitates ahead of the composite oxide of Mn and Fe during the solidification of the slag formed on the molten pool. Then, the composite oxides of Mn and Si, as well as the composite oxides of

Mn and Ti, begin to form, and these oxides grow in such a way that they overlap, resulting in a dendrite-like solidification morphology. In terms of slag distribution, MnO and the composite oxide of Mn and Fe have a higher solidification initiation temperature and considering the lower ratio of composite oxide of Si and Mn, the agglomeration in the molten pool is less likely to occur, leading to a tendency for the slag to spread thinly. As a result, the conductivity of the slag portion increases, and electrodeposition coatability is inferred to have improved. Considering the conductivity of Mn oxides from the calculation results, MnO is generally known to have lower conductivity at room temperature compared with FeO. Therefore, it is believed that  $Mn_3O_4$  with a spinel structure and composite oxides of Mn and Fe, as well as those of Mn and Ti, contribute to the conductivity. However, since the formed slag consists of multiple oxides overlapping in a complex manner, separating the combined state of individual oxides to identify the specific current paths for the formation of electrodeposition coating is challenging. The mechanism is not yet fully understood, and further investigation and consideration are needed in the future.

## Conclusions

By adjusting the balance of deoxidizing element additions in the wire, a welding consumable has been developed that could change the morphology and electrical properties of welding slag, so as to make electrodeposition coating formable even when slag remains in the weld joint. In this report, the composition of slag and the internal structure of oxides within conventional wire and developed wire have been explained in detail, and the factors contributing to improved electrodeposition coatability have been discussed as follows:

- Changing the ratio of Si, Mn, and Ti components in the wire allows control over the ratio of elements constituting the welding slag, resulting in a change in the slag morphology on welding bead surfaces.
- The internal structure of the slag in conventional wire is primarily composed of oxides of Si and Mn throughout, and these oxides are locally thickly formed on bead surfaces.
- In the developed wire, phases of oxides consisting of Mn, Ti, and Fe are formed in the depth direction of the slag, exhibiting a dendrite-like structure. Slag agglomeration behind the molten pool during welding is suppressed, and the slag is formed thinner than for the conventional wire.
- The equilibrium calculation based on the results of slag analysis suggest that Mn oxides with a spinel structure may contribute to the conductivity of the slag in the developed wire.

However, in this investigation, the specific oxides responsible for the conductivity of the slag in the developed wire were not identified. Further research will be conducted to investigate the combined state of oxides constituting the slag and to work towards understanding the mechanism that improves electrodeposition coatability.

## References

- 1) Oyabu et al. Transactions ISIJ. 1983, Vol.23, p.994.
- 2) R. Yamazaki et al. R&D Kobe Steel Engineering Reports. 2019, Vol.69, No.1, p.98.
- 3) Umehara et al. Quarterly Journal of the Japan welding society. 2009, Vol.27, No.2, p.163s.
- 4) S. Kodama et al. JSW Technical Review. 2019, Vol.412, p.78.
- 5) M. Wada. Journal of Advanced Science. 2010, Vol.22, No.1&2, p.1.
- 6) S. Maeda et al. Tetsu-to-Hagane. 2018, Vol.104, No.9, p.509.

# Influence of LME Cracks in Resistance Spot Welds of Zinc-coated Ultra-high Strength Steel Sheets on Joint Strength

Kyohei MAEDA\*<sup>1</sup> · Dr. Reiichi SUZUKI\*<sup>1</sup> · Masao HADANO\*<sup>2</sup>

\*<sup>1</sup> Application Technology Center, Technical Development Group

\*<sup>2</sup> KOBELCO WELDING TechnoSolutions Co., LTD

## Abstract

*Liquid metal embrittlement (LME) cracking, seen in resistance spot welds of ultra-high strength steel, has become a subject of discussion in the automobile industry. However, only a few articles concerning the effect of this type of crack on joint properties have been reported. Therefore, in this study, LME cracks were classified into 3 types based on location and the influences of these cracks on static and fatigue strengths were investigated. Type A crack, occurring within an indentation of a spot weld, slightly affected the joint strength, while type B crack, generating on the indentation periphery or outside it, significantly lowered both tensile-shear and cross-tension strengths, which decreased by up to 35% and 44%, respectively. Type C crack, seen near the interface of the sheets, deteriorated fatigue strength as well.*

## Introduction

Since the 1990s, there has been a global demand for reducing greenhouse gases as a measure against global warming, with advocacy for achieving carbon neutrality by 2050. In the automotive industry, efforts are being made to decrease CO<sub>2</sub> emissions while driving by advancing the electrification and lightweighting of vehicle bodies<sup>1), 2)</sup>. The demand for collision safety is also increasing year by year. To achieve this, along with fuel efficiency, the application of ultra-high strength steel (referred to as “UHSS”) sheets to vehicle bodies is on the rise. In the case of UHSS, alloying additives may be increased to balance strength and workability<sup>3)</sup>. Generally, it is known that welding properties deteriorate with an increase in alloying additives. For example, in resistance spot welding, mainly used in the production line of automobiles, expulsion and surface flash occur on the low current side, narrowing the condition range for proper welding<sup>4), 5)</sup>. In tensile tests, brittle fractures, such as interface failure and partial plug failure, occur, causing a decrease in joint strength<sup>6)</sup>. Furthermore, in some recently developed UHSSs, LME cracks caused by molten zinc have been reported to occur during the welding of Zn-coated steel sheets<sup>7)-9)</sup>. As shown in **Fig. 1**, LME cracks occur when three

factors overlap: high crack susceptibility, molten zinc, and tensile stress.

In other words, if any one of these factors can be eliminated, the cracking can be prevented. Previous studies have demonstrated through numerical analysis that significant tensile stress occurs in the welded area immediately after electrode release<sup>10)</sup>. Suggestions have been proposed to mitigate LME cracking through process enhancements, specifically targeting stress alleviation and minimizing the volume of molten zinc during electrode release<sup>10)-15)</sup>. On the other hand, welding conditions are often restricted by production cycle time and part shapes, making it not always possible to apply these crack prevention methods. Therefore, to effectively utilize UHSS, it is believed that optimization of welding conditions alone is not sufficient, and structure design allowing the presence of LME cracks is also necessary. Generally, in the design of automobiles, the required strength in the welding area is calculated on the basis of the loads applied during both driving and collision. For spot welding, JIS Z 3140 specifies required values for tensile-shear strength (TSS) and cross-tension strength (CTS) for each category of sheet thickness and strength, and these may be used as indicators during design. Even if LME cracks occur, there is a possibility of expanding the application range of ultra-high-tensile steel by adopting a structural design approach that allows for cracks as long as the standard strength is achieved. A similar approach is adopted in JIS Z

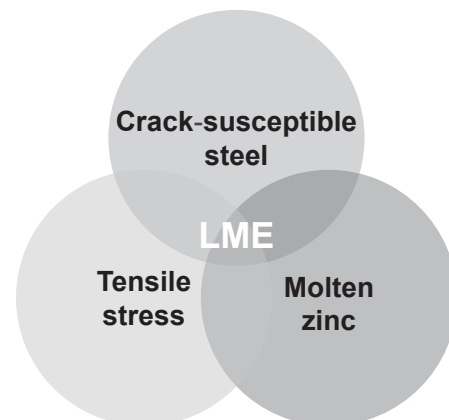


Fig.1 Factors of LME cracking

3104, where, among the four categories of scratches (defects), the first and fourth categories need not be counted if they are below certain dimensions. However, data regarding the effects of LME cracks on joint strength is limited, and as of now, there are no established standards for LME cracks. Against this backdrop, this study aims to classify LME cracks in accordance with their occurrence locations and elucidate the effects of various cracks on static strength and fatigue strength.

## 1. Experimental method

### 1.1 Classification of LME cracks

LME cracks are broadly categorized into outer cracks occurring on the surfaces of joints and inner cracks occurring internally<sup>16)</sup>. As shown in Fig. 2, this study further classifies the outer cracks into type A cracks, which occur within an indentation, and type B cracks, which occur at the periphery of an indentation. Inner cracks occurring in the heat-affected zone (HAZ) are classified as type C cracks.

### 1.2 Investigation of the effects of LME cracks on static strength and fatigue strength

The test material used was a 980MPa-grade GA steel sheet with a thickness of 1.4 mm. For the static tensile test, the test pieces were prepared in accordance with JIS Z 3136 and Z 3137, and for the fatigue test, the test pieces followed Z 3138, with the size as shown in Fig. 3. The steel sheets were immersed in hydrochloric acid, creating samples with a remaining plating layer on only one side near the welded area (hereinafter referred to as “plated material”) and samples with all plating layers removed on both sides (hereinafter referred to as “bare material”).

A servo-pressure-type DC inverter welding machine was used for welding. The electrodes were DR-type electrodes made of chrome copper, with a tip diameter of 6 mm and a tip curvature radius of 40 mm. The welding conditions are shown in Fig. 4, and the schematic diagram of the joint preparation method is illustrated in Fig. 5.

The plated material was used to control the initiation positions of cracks; i.e., for outer cracks, the plated surfaces of the upper and lower sheets were positioned facing the electrode, and for inner cracks, they were positioned facing the side of the mating material. For the latter, aiming at promoting crack formation, a strike angle of 7° was set, and a 2 mm gap was introduced between the sheets. For comparison, joints with no cracks but having a

nugget with a diameter equivalent to the joint with outer and inner cracks were produced using the bare material (hereinafter referred to as “defect-free jointing”). The type B cracks have initiated from the periphery of the indentation to the outside, and it

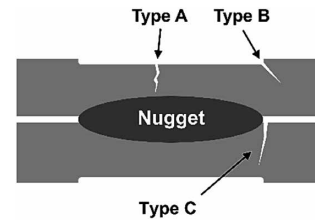


Fig.2 Classification of LME cracks

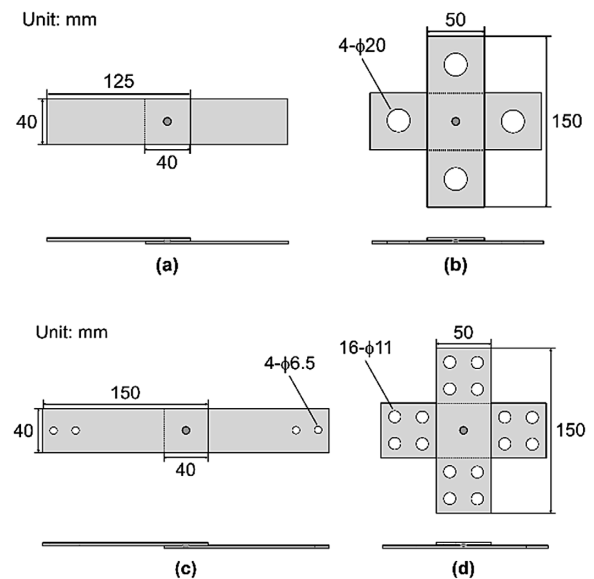


Fig.3 Dimensions of tensile specimens  
(a) static tensile-shear, (b) static cross-tension tests  
(c) tensile-shear fatigue, (d) cross-tension fatigue tests

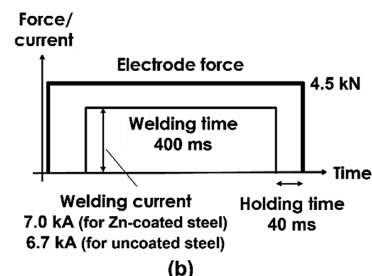
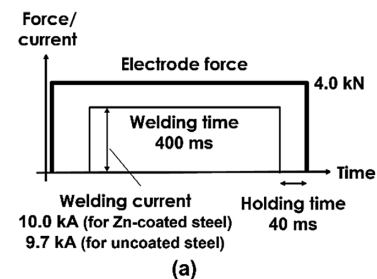


Fig.4 Welding conditions for producing welds with LME  
(a) outer, (b) inner cracks

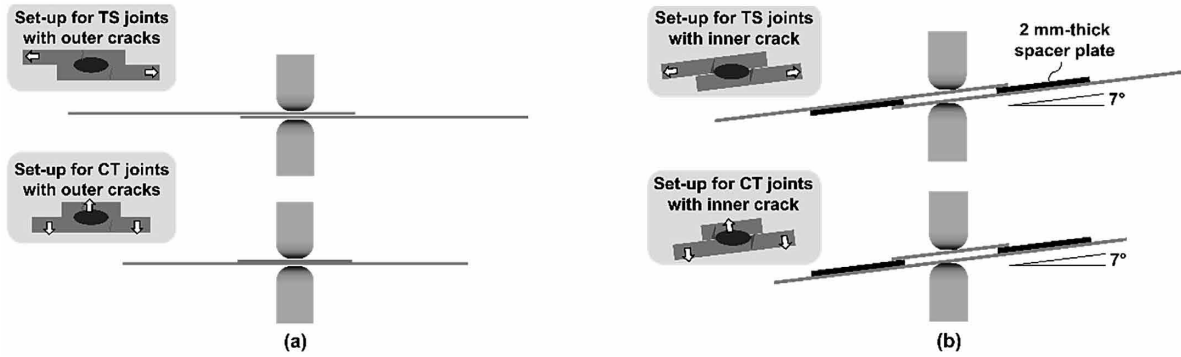


Fig.5 Schematic illustration of set-up for producing welds with LME (a) outer, (b) inner cracks

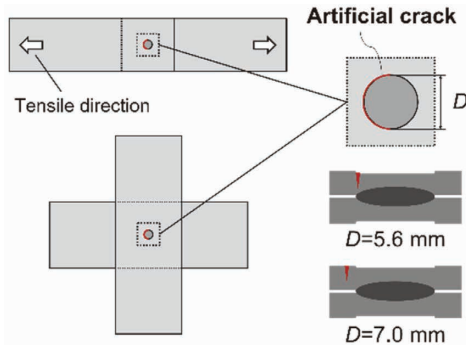


Fig.6 Schematic illustration of creating artificial crack in welds

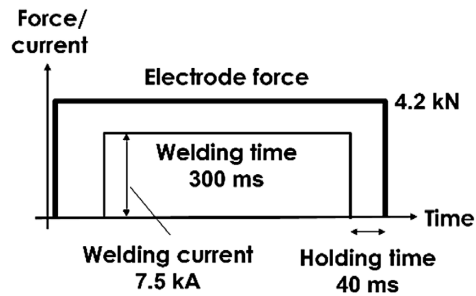


Fig.7 Welding conditions for producing welds without crack

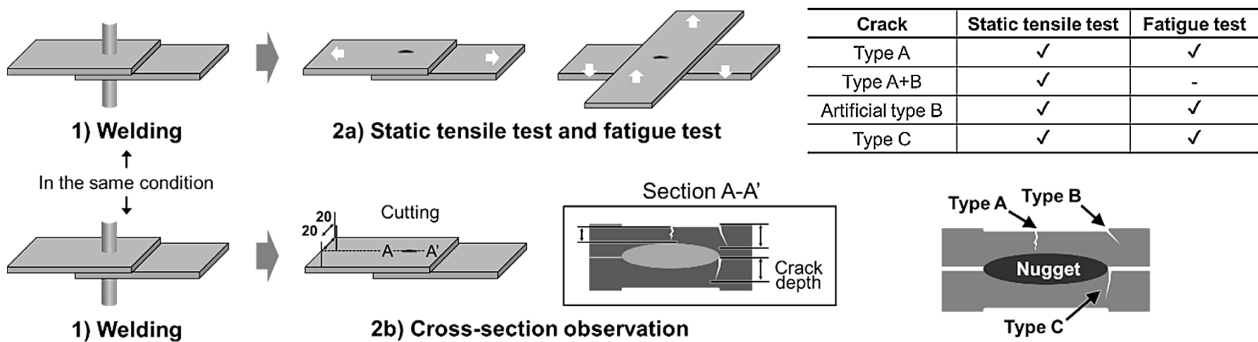


Fig.8 Process flow of testing and evaluation

is assumed that the degree of adverse effects varies depending on the location of initiation. Controlling the subtle initiation positions of cracks through welding is challenging. Hence, the cracks were simulated using a femtosecond laser. As shown in Fig. 6, joint strength at various initiation positions was investigated by forming a semi-circular groove with a width of millimeter-order (hereinafter referred to as an “artificial defect”) on a defect-free joint. After welding the bare material under the conditions shown in Fig. 7, artificial defects were introduced to the inner and outer peripheries and outside of the indentation on the side of the upper sheet. The diameter of the artificial defect was 5.6 mm for the former and 7.0 mm for the latter. The flow of evaluation tests for the prepared joints is

shown in Fig. 8. Two types of static tensile tests (tensile-shear test and cross-tensile test) and two types of fatigue tests (tensile-shear fatigue test and cross-tension fatigue test) were conducted. The number of samples (denoted by a numerical value following n) for the static tensile test was n3 to n5, and the tensile speed was set at 10 mm/min. Fatigue tests were conducted for n2 at each load, with a stress ratio of 0.1, frequency of 5 to 20 Hz, and a maximum repetition number of  $2 \times 10^6$ . It should be noted that, for joints where outer cracks were induced experimentally, some included only type A cracks, and others included both type A and B cracks. Therefore, visual observation with a microscope was conducted, and for the former, both static tensile and fatigue tests were performed, while

for the latter, only static tensile tests were conducted. Additionally, cross-sectional observations were carried out for another set of n3 samples apart from the tensile test. Observations of the welded area were conducted by cutting the center of the nugget in the tensile-shear test piece along the longitudinal section, followed by corrosion in a picric acid-saturated solution, and examination using an optical microscope. The depth of the cracks was measured following the procedure shown in Fig. 8.

## 2. Experimental results and discussions

### 2.1 Effect of outer cracks on static strength and fatigue strength

The appearances and cross-sections of the joints are shown in Fig. 9. A joint with only type A cracks (b) has been checked as well as a joint with both type A and B cracks (c) (hereinafter referred to as “joint with type-A cracks” and “joint with type A+B cracks,” respectively). The depths of the type A and B cracks are 0.07 to 2.13 mm and 0.07 to 0.91 mm, respectively, and the type A cracks have been observed to penetrate both surfaces of the indentation.

The results of the static tensile test are shown in Fig.10. In the lower part of the graph, the types of cracks are also described. In comparison with the defect-free joint, the joints with type A cracks

have been found to have equivalent joint strength, confirming that the type A cracks have little effect on static strength. On the other hand, the joints with type A+B-cracks have cases where TSS and CTS are lower than the defect-free joint. When comparing the joint strength of the lowest strength combinations, the joints with type A+B cracks show an approximately 35% reduction in both TSS and CTS compared with the defect-free joint. Fig.11 shows the appearances of the joints with type A+B cracks before and after the tensile tests. Also included in this figure are the crack initiation positions, and the schematic diagrams of fracture positions during the tensile test. For the tensile-shear test joint, the crack initiation positions have been classified into the transverse area and longitudinal area, as shown in this figure. In both joints, fractures have occurred along the type B cracks. For joints with a small crack initiation zone in the transverse area, TSS is almost equivalent to that of the defect-free joint. In contrast, joints with a wide-ranging presence of cracks exhibit a significant decrease in TSS. In the cross-tension testing, stress is uniformly applied at the periphery of the nugget, resulting in a decrease in strength regardless of the location of crack initiation. In contrast, in shear-tension testing, stress concentration primarily occurs in the transverse area. Therefore, cracks that occur in the longitudinal area are believed to have minimal impact on the overall strength. The results of fatigue test for the

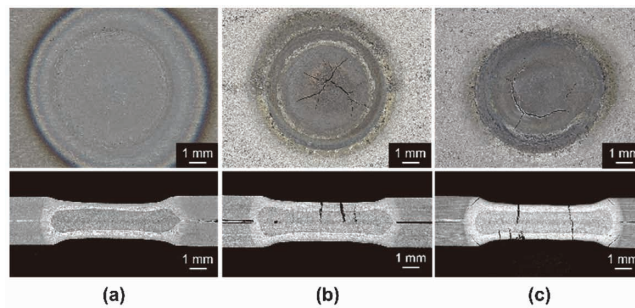


Fig.9 Surface and cross-section images of welds (a) without LME crack, (b) with type A crack, (c) with type A+B cracks

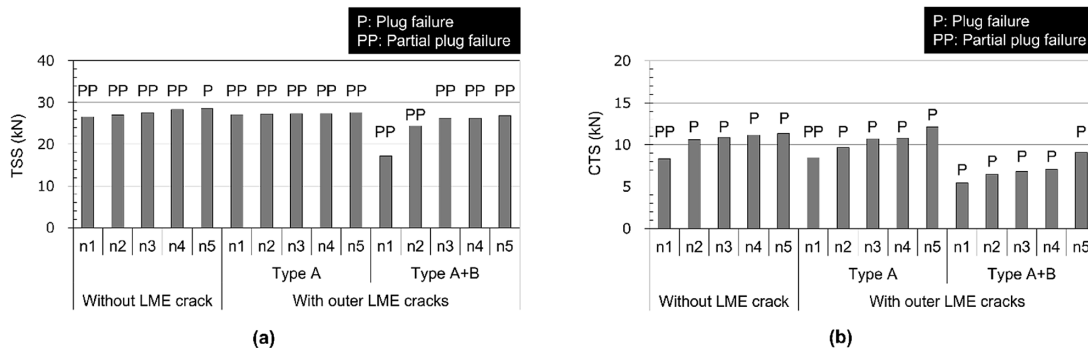


Fig.10 Results of static (a) TS, (b) CT tests

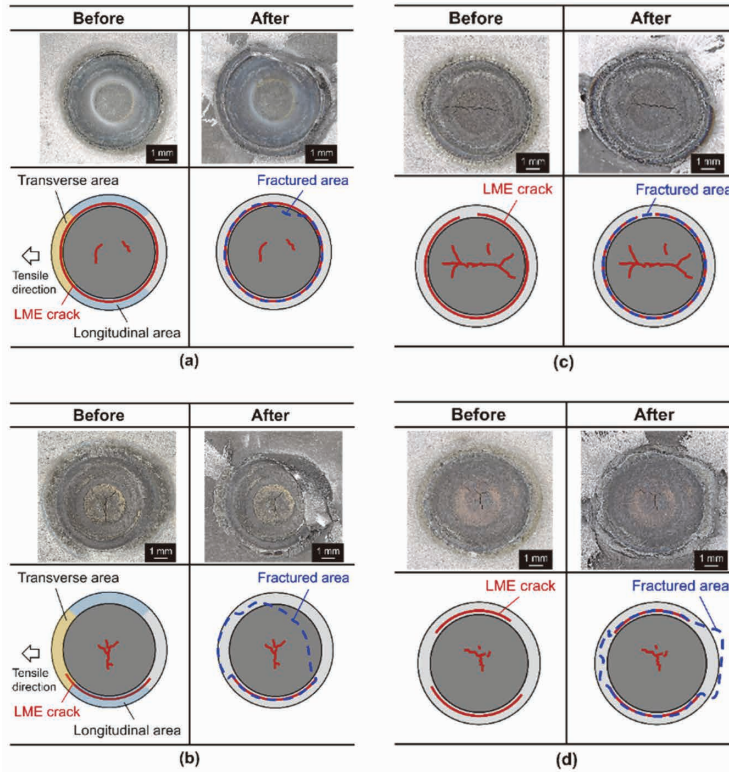


Fig.11 Surface view of specimens with type A+B cracks before and after static tensile tests (TS test: (a)n1, (b)n3, CT test: (c)n1, (d)n4)

joint with type A cracks and the defect-free joint are shown in Fig.12. No significant difference has been observed in the L-N diagram due to the presence or absence of type A cracks, indicating that type A cracks have little effect on fatigue properties.

## 2.2 Effect of occurrence position for Type B cracks on static strength and fatigue strength (Results of study utilizing artificial defects)

The appearance and cross-sectional images of the joint are shown in Fig.13. The depths of artificial defects at the inner and outer peripheries of the indentation and the outside of the indentation are 0.55 to 0.63 mm and 0.54 to 0.61 mm, respectively. The results of the static tensile test are presented in Fig.14. For joints with artificial defects at the inner and outer peripheries of the indentation, TSS is equivalent, while CTS is lower in comparison with the defect-free joint. On the other hand, for joints with artificial defects on the outside of the indentation, a slight decrease in TSS, in addition to CTS, is observed. When the lowest CTS values are compared, the former joint shows approximately a 35% reduction in strength compared with the defect-free joint, and the latter joint shows approximately a 44% reduction. This suggests that the further away from the indentation, the greater the negative impact on cracks. In comparison with the tests

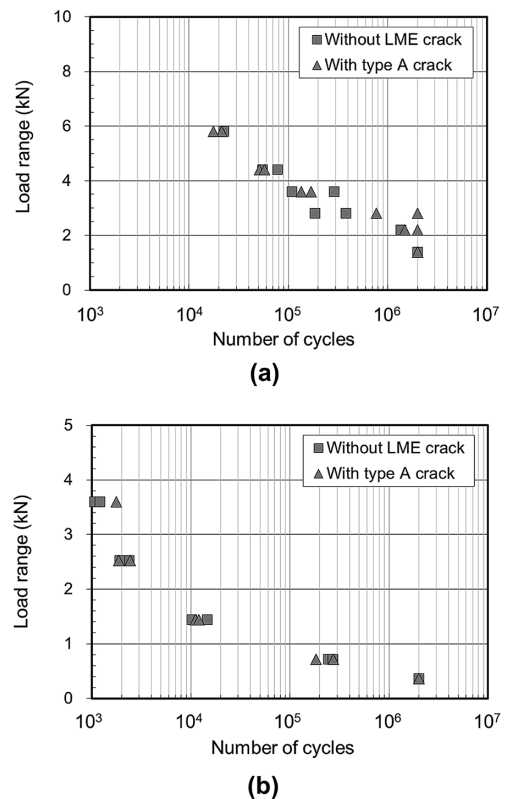


Fig.12 Results of (a) TS, (b) CT fatigue tests

using the previously mentioned joint with type A+B cracks, no significant decrease in TSS has been observed in joints with introduced artificial defects.

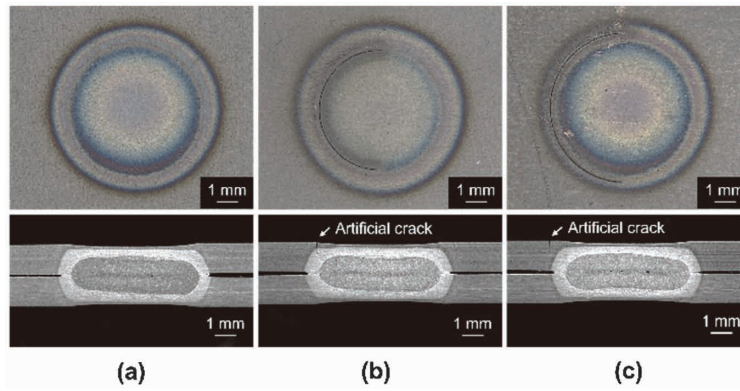


Fig.13 Surface and cross-section images of welds  
 (a) without crack, with artificial crack (b) on indentation periphery, (c) outside indentation

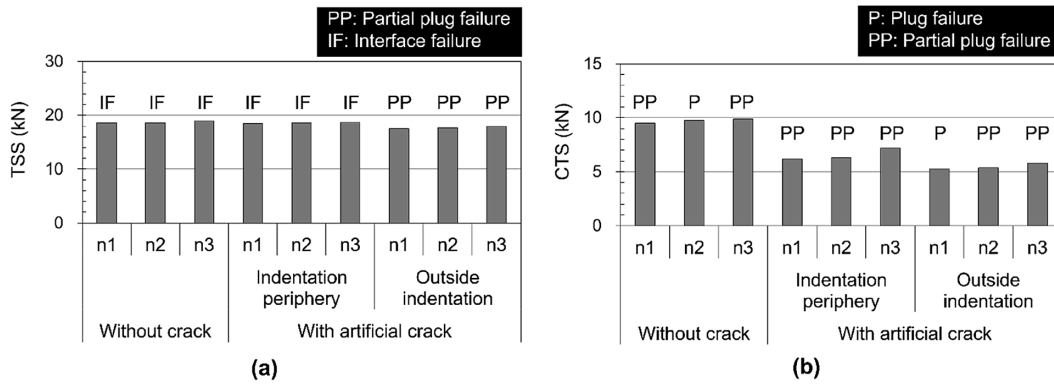


Fig.14 Results of static (a) TS, (b) CT tests

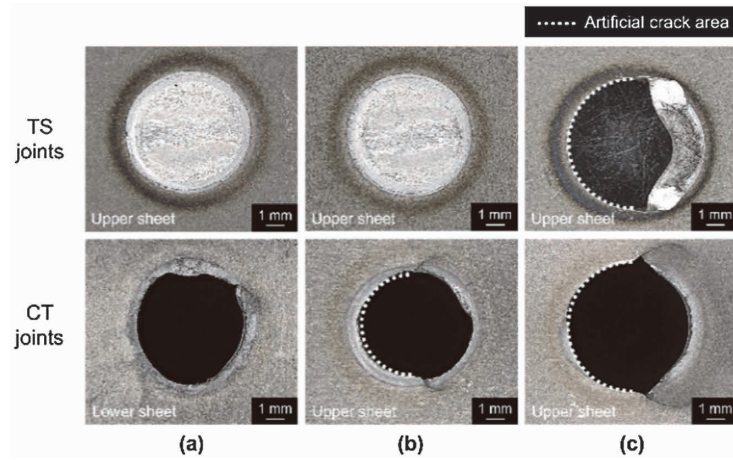


Fig.15 Surface view of fractured TS and CT specimens  
 (a) without crack, with artificial crack (b) on indentation periphery, (c) outside indentation

This is presumed to be due to the difference in size between actual cracks and artificial defects. Due to constraints in the laser processing machine used in this experiment, the depth of artificial defects has been aimed at 0.6 mm, which is smaller than the actual depth of the type B cracks. In a previous study based on numerical analysis, Ma et al. have demonstrated that the reduction in tensile-shear strength is enhanced with the increasing size of the type B cracks<sup>17</sup>. Appearance images after tensile-

shear and cross-tensile tests are shown in Fig.15. In joints where a decrease in strength has been observed, fractures have occurred along the artificial defects. The results of the fatigue test are presented in Fig.16. No significant differences are observed in the L-N diagram due to the presence or absence of artificial defects. In other words, in the range of depths equivalent to the artificial defects studied in this experiment, there is a high probability that the fatigue properties would not significantly decrease

due to type B cracks.

### 2.3 Effect of inner cracks on static strength and fatigue strength

Fig.17 shows the cross-sectional images of joints. Type C cracks have been observed at the corona bond edges of the upper and lower sheets (hereinafter referred to as a “joint with type C cracks”). The depth of the cracks ranges from 0.25 to 0.79 mm. The results of the static tensile test are presented in Fig.18. Within the range studied in this experiment, there is little decrease in joint strength due to inner cracks. Both the joint with type C cracks and the defect-free joint exhibit interface fractures in the tensile-shear test and plug fractures or partial plug fractures in the cross-tensile test. Although no changes are observed in joint strength or fracture morphology due to the presence of inner cracks in this experiment, a study using 1.2 GPa-grade steel sheets confirmed a reduction in TSS due to the type C cracks<sup>18</sup>. The reasons for the varying effect of cracks due to differences in steel sheet strength are not clearly understood. However, it is speculated that the distribution of stress during the tensile-shear test may change depending on the hardness distribution in the nugget-HAZ-base metal interfaces and the depth of the cracks. In the case of 1.2 GPa-grade steel sheets, it is presumed

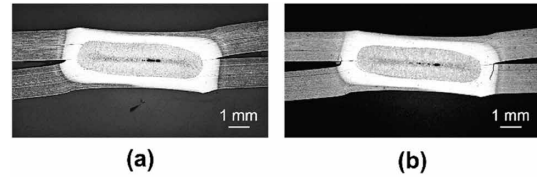


Fig.17 Cross-section images of welds (a) without LME crack, (b) with type C crack

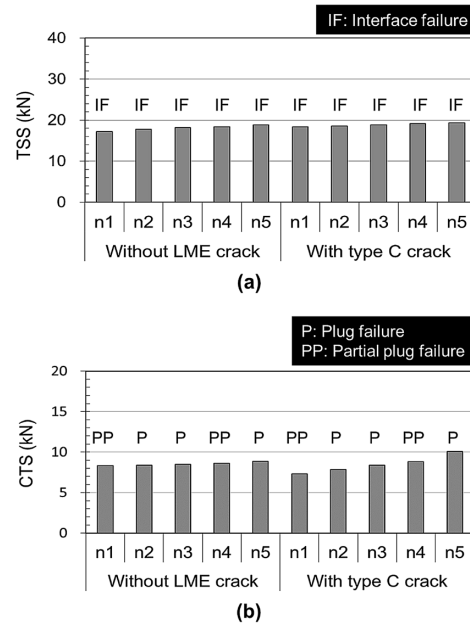


Fig.18 Results of static (a) TS, (b) CT tests

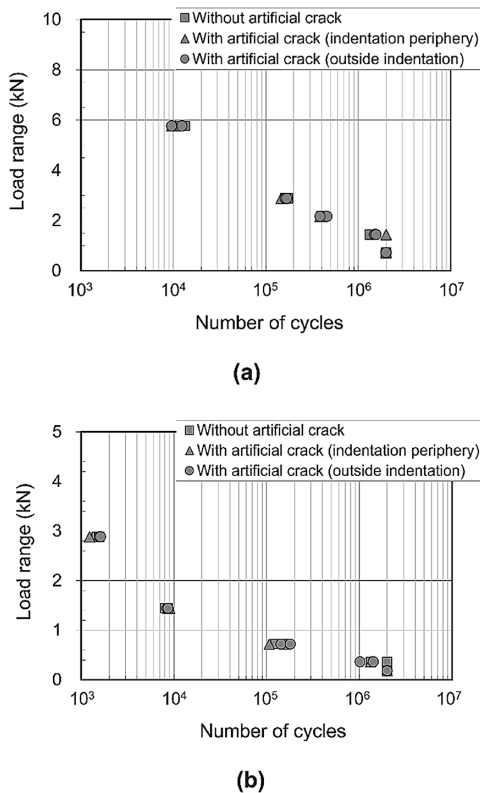


Fig.16 Results of (a) TS, (b) CT fatigue tests

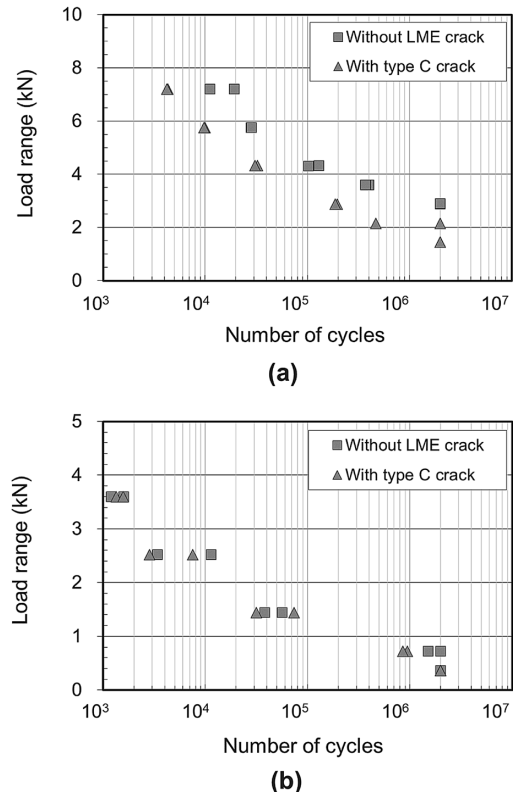


Fig.19 Results of (a) TS, (b) CT fatigue tests

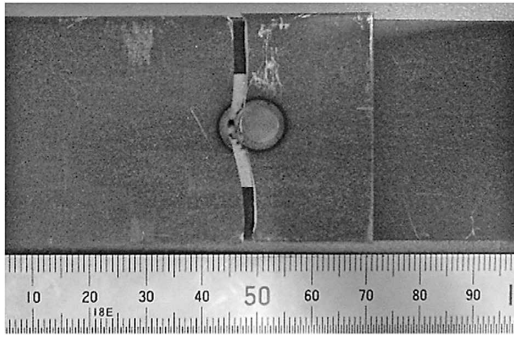


Fig.20 Surface view of fractured TS fatigue specimen with type C crack

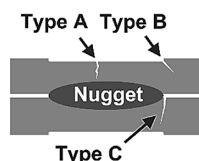
that the stress concentration on the type C cracks is more pronounced. The results of the fatigue test are shown in Fig.19. No significant differences are observed in the L-N diagrams for cross-tension fatigue tests between the joint with type C cracks and the defect-free joint. On the other hand, in the tensile-shear fatigue test, early fractures occur in the joint with type C cracks under all load conditions, indicating that type C cracks lead to a reduction in fatigue properties. As shown in Fig.20, cracks have propagated from around the nugget towards the base metal in the joint with Type C cracks, suggesting that type C cracks may have served as the initiation point for the cracks. Initial cracks in tensile-shear fatigue tests have been reported to occur near the corona bond edges<sup>19</sup>. As type C cracks occur in almost the same position as these cracks, they are considered a potential factor contributing to the reduction in fatigue properties.

### Conclusions

LME cracks have been classified into types A to C, and their respective effects on joint strength

have been experimentally investigated. The summarized results are shown in Fig.21. Regarding type A cracks, even those penetrating through both the surfaces have little effect on joint strength. In contrast, it has become evident that type B and C cracks could potentially reduce joint strength. It should be noted that, in this study, tensile tests and cross-sectional observations have been conducted separately; hence, a thorough discussion on the relationship between joint strength and crack depth has not been provided. In a previous study<sup>18</sup>), the authors have attempted to quantify the effect of crack depth on joint strength by non-destructively observing LME cracks in tensile test samples using X-ray CT scans. As mentioned earlier, the adverse effects of LME cracks vary with steel types and sheet compositions. Performing tests for a vast range of steel types and sheet compositions similar to this study is impractical. Therefore, the use of numerical analysis is essential. The authors have already begun numerical analysis and have constructed a model that can predict the effects of cracks at the test piece level<sup>17</sup>). Furthermore, the investigation into the effect of LME cracks at the level of actual vehicle components is ongoing. Dynamic three-point bending tests have been conducted on simulated center pillar samples with artificially induced outer and inner cracks. The results have revealed that, under assumed IIHS side impact distribution conditions, the presence of LME cracks did not lead to the fracture of resistance spot welded parts. The effects on component performance, such as maximum load and absorbed energy, have been found to be extremely small<sup>20</sup>). Vehicle lightweighting is a persistent need, and the application of ultra-high tensile steel is predicted to further expand in the future. While multiple spot welding processes for preventing LME cracks have

Crack type		Crack depth (mm)	Static strength		Fatigue strength	
			TS	CT	TS	CT
A	Weld crack	0.07~2.13	Influenced slightly	Influenced slightly	Influenced slightly	Influenced slightly
B	Weld crack	0.07~0.91	<b>Weakened</b>	<b>Weakened</b>	-	-
	Artificial crack	Approximately 0.60	Influenced slightly <sup>1)</sup>	<b>Weakened</b>	Influenced slightly	Influenced slightly
C	Weld crack	0.25~0.79	Influenced slightly <sup>2)</sup>	Influenced slightly	<b>Weakened</b>	Influenced slightly



- 1) TSS might be weakened with a greater artificial crack.
- 2) The result of the experiment using 1 GPa steel. Type C crack weakened TSS of spot welds of 1.2 GPa steel.

Fig.21 Summary of experiments

been developed and proposed, establishing quality assurance methods for LME cracks is also deemed necessary. It is hoped that the approaches and insights introduced in this paper can contribute to these efforts.

## References

- 1) Y. Miyazaki et al. Journal of Japan Laser Processing Society. 2019, Vol.26, No.1, pp.13-23.
- 2) D. Tarui. Journal of the Japan Society of Precision Engineering. 2018, Vol.84, No.5, pp.404-407.
- 3) H. Matsuda. Journal of the Japan Welding Society. 2020, Vol.89, No.6, pp.420-424.
- 4) K. Yamazaki et al. Quarterly Journal of the Japan Welding Society. 1999, Vol.17, No.4, pp.553-560.
- 5) H. Oikawa et al. Nippon Steel Technical Report. 2006, No.385, pp.36-41.
- 6) R. Ikeda. Journal of the Japan Welding Society. 2015, Vol.84, No.6, pp.11-16.
- 7) A. G. Kalashami et al. Journal of Manufacturing Processes. 2020, Vol.57, pp.370-379.
- 8) R. Sierlinger et al. White Paper; voestalpine Stahl GmbH. 2016, pp.1-16.
- 9) G. Jung et al. Metals and Materials International. 2016, Vol.22, No.2, pp.187-195.
- 10) K. Takashima. Welding Journal. 2021, Vol.90, No.7, pp.24-28.
- 11) C. Bohne et al. Science and Technology of Welding and Joining. 2020, Vol.25, No.7, pp.617-624.
- 12) C. Bohne et al. Science and Technology of Welding and Joining. 2020, Vol.25, No.4, pp.303-310.
- 13) E. Wintjes et al. Journal of Manufacturing Science and Engineering. 2019, Vol.141, No.10, Article 101001, 9p.
- 14) K. Maeda et al. Prevention of LME Cracks in Resistance Spot Welding by Optimization of Pressure and Welding Current. Preprints of the National Meeting of JWS. The Japan Welding Society, 2020, pp.130-131.
- 15) Y. Shimoda et al. Development of Prevention Method for LME Cracks in Resistance Spot Welding of Zinc-Coated Ultra-High Tensile Steel Sheets - Development of Mechanical Upset Control Shank. Preprints of the National Meeting of JWS. The Japan Welding Society, 2020, pp.132-133.
- 16) O. Siar et al. Metals. 2020, Vol.10, No.9, Article 1166.
- 17) Y. Ma et al. Materials & Design. 2021, Vol.210, Article 110075, p.21.
- 18) K. Maeda et al. Quarterly Journal of the Japan Welding Society. 2022, Vol.40, No.3, pp.123-133.
- 19) Y. Uematsu et al. Quarterly Journal of the Japan Welding Society. 2019, Vol.37, No.4, pp.152-161.
- 20) N. Mizutani et al. Effect of Resistance Spot Welding LME Cracks in Hat Section Parts on Part Performance. JSAE Autumn Convention Proceedings. The Japan Welding Society, Society of Automotive Engineers of Japan. 2021, Article 20216153.

# Metal Surface Preparation Technology for Adhesive Joining Reliability

Dr. Yusuke TAKAHASHI\*<sup>1</sup> • Shintaro YAMAMOTO\*<sup>2</sup> • Daiki KATSUNO\*<sup>2</sup> • Yoko MURATA\*<sup>2</sup>

\*<sup>1</sup> Materials Research Laboratory, Technical Development Group (currently Business Development Department)

\*<sup>2</sup> Materials Research Laboratory, Technical Development Group

## Abstract

*In recent years, adhesive bonding has attracted interest as a key joining technology for lightweight metals and dissimilar materials, and its importance is increasing across various industrial fields.*

*When bonding metallic materials, surface preparation technology plays a crucial role in maximizing the inherent bonding properties of the adhesive, because its bonding strength is greatly affected by the surface condition. This paper aims to discuss the relationship between the surface condition of metallic materials and adhesion properties. Additionally, it will cover the improvement of adhesion by surface preparation, and efforts to evaluate adhesion strength and durability, while considering the actual environment of use.*

## Introduction

In the field of metal joining technology, welding and bolted connections play a leading role and are widely utilized across various industries mainly for ferrous materials. On the other hand, for joining parts requiring complex shapes, high dimensional accuracy, dissimilar materials, or areas where heating is to be avoided, adhesive joining takes precedence. Adhesive joining excels in rigidity, thanks to its ability to secure joints over a large surface area, offering high air and water tightness. Moreover, it avoids the distortions and embrittlement caused by heat, often experienced in welding. Additionally, it eliminates the need for pre-drilling and screwing associated with bolted connections, showcasing superior attributes in terms of appearance and productivity. Given these advantages, in recent years, the application of adhesive joining has expanded in the automotive industry for joining dissimilar materials, like joining aluminum and composites, and for improving NVH (Noise, Vibration, Harshness) characteristics<sup>1)</sup>. Some manufacturers outside Japan utilize adhesive joining in skeleton structures for enhancing the collision safety.

Adhesive joining poses unique challenges compared with bolted connections and welding. When designing the joint strength of adhesive joining, for example, consideration must be given to both adhesion strength and the material strength

of the adhesive itself. From a standpoint of strength stability, it is desirable for the adhesion strength to be higher than the material strength to ensure that any fracture would consistently occur in the adhesive material (hereinafter referred to as “cohesive failure”). Insufficient adhesion strength may lead to delamination at the interface between the adhesive and metal before cohesive failure occurs (referred to as “interfacial delamination”), making it challenging to achieve stable joint strength. Furthermore, since adhesives are typically resin-based, they are prone to undergo changes in state due to water, heat, UV radiation, and stress. Consequently, when selecting adhesives, consideration must be given to their effects in real-use environments<sup>2)</sup>.

Due to these challenges, adhesive joining falls short of providing sufficient strength reliability compared with other joining technologies. Its adoption is limited in applications requiring prolonged use in harsh environments or demanding high safety standards. Therefore, this paper aims to contribute to the understanding and improvement of adhesive joining for metal materials. Specifically, it compiles and explains factors that significantly affect adhesion strength, such as the surface condition of materials, surface modification technologies for achieving stable adhesion strength, and case studies on ensuring long-term strength reliability<sup>3)</sup>.

## 1. Surface conditions of metal materials and adhesiveness

When bonding metal materials, the adhesive comes into contact with their surfaces, making the surface conditions of the material significantly affect the adhesion strength. In most cases, the surfaces of metal materials are covered with natural oxide films. The effect of material compositions and various processes such as rolling, extrusion, cutting, as well as heating, water cooling, and others during manufacturing can lead to excessive growth of the oxide film, structural defects, alterations and corrosion, creating non-uniform conditions. Additionally, organic matter from processing oil, packaging materials, storage environments, etc., may be adsorbed onto the oxide film, significantly impacting the adhesiveness of metal materials<sup>4)</sup>

(Fig. 1(a)).

## 1.1 Surface contamination

In bonding any substance, not limited to metal materials, the first essential step is to eliminate factors hindering the physical contact between the adhesive and the adherend material surfaces. Due to these factors, residues on the surfaces of adherend materials reduce the contact area between the adhesive and the surfaces of the adherend materials, hindering the intended adhesion strength. Therefore, it is necessary to clean the surfaces of adherend materials before adhesion. While particles and oil content adsorbed on material surfaces can be removed to some extent by solvent cleaning and the like, some substances, such as those forming a strong chemical bond with the oxide film, may not easily be removed. Hence, alkaline degreasing agents are commonly used for chemical cleaning<sup>5)</sup>. On the other hand, certain adhesives have properties that allow them to absorb and disperse oil content within the resin. These adhesives can exhibit good adhesiveness even when there is some oil on the surfaces of adherend materials and are used in the automotive manufacturing processes<sup>6)</sup>.

## 1.2 Vulnerable Areas

The next important point is the strength of the material surface. As previously mentioned, the surfaces of metal materials are covered with oxide films that change their states due to alloy composition, manufacturing processes, and storage conditions, leading to structurally or chemically brittle areas. These vulnerable areas, known as weak boundary layers (WBL), become fracture initiation points in adhesive joining and can destabilize adhesion strength.

For example, the surfaces of high-strength aluminum alloys containing magnesium are known to have a brittle, magnesium-containing oxide film

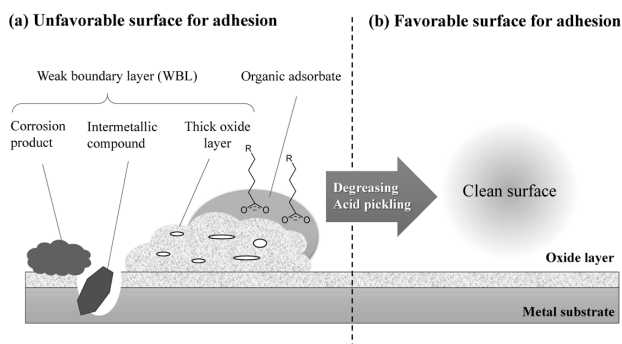


Fig.1 Image of metal surface condition

due to the heat effect during manufacturing, leading to WBL<sup>7)</sup>. This oxide film can be dissolved and removed with acid, which is why acid pickling is often carried out as part of the pre-treatment for adhesive bonding of aluminum alloys, typically in conjunction with degreasing processes. After acid pickling, only a thin, well-bonding natural oxide film is present on the surfaces of aluminum alloy, enabling the material's inherent adhesiveness to be expressed (Fig. 1(b)). In addition to acid pickling, processes such as blasting treatment and laser treatment can effectively remove surface contamination and WBL simultaneously, making them useful as pre-treatments for adhesion.

Metal materials vary in manufacturing methods and composition depending on the type, shape, and application of the material. Additionally, manufacturing processes and facilities may differ among manufacturers. Consequently, even for metal materials with the same strength specifications, their surface conditions may not be identical. Therefore, the pre-treatment processes discussed in this section, aimed at removing surface contamination and WBL, are fundamental operations for achieving high strength reproducibility in adhesive bonding.

## 2. Adhesion mechanism and surface modification of metals

As stated in Section 1, the ability to demonstrate the inherent adhesiveness of an adhesive can be achieved by "resetting" the surface of the metal material by removing contamination and WBL and returning it to a state with only the natural oxide film. Furthermore, a crucial factor is the compatibility between the adhesive and the oxide film. Due to the polymer nature of the adhesive, its chemical structure varies depending on the type of resin composing it. Similarly, the composition and chemical properties of the oxide film vary, depending on the type of base material, leading to differences in adhesiveness based on the combination of adhesive and metal material, as reported in the literature<sup>8)</sup>. For instance, Fig. 2 shows the observation results of the fracture morphology after lap-shear tests on epoxy-bonded joints of titanium and copper sheets which had been cleaned and had their surface morphology controlled by blast treatment. In the untreated state, both materials have their metal surface, and interfacial delamination dominates between the adhesive and material. However, blasting treatment changes the fracture morphology to cohesive failure of the adhesive. In the case of copper, the fracture is almost entirely cohesive failure. In contrast, with titanium,

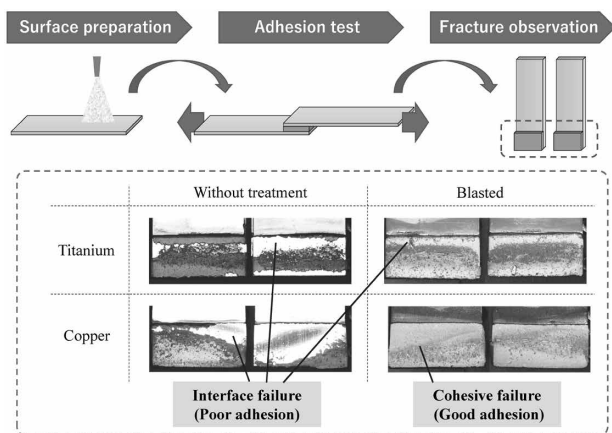


Fig.2 Difference of fracture surface after adhesion test of blast-treated or untreated titanium and copper

interfacial delamination occurs. This indicates that, even when the material's cleaning conditions and surface shapes are identical, there are differences in adhesiveness based on the type of metal material, specifically, the differences in the oxide film.

Moreover, the stability of the oxide film is a crucial factor affecting adhesion strength. While the oxide film immediately after cleaning treatment is immaculate, it easily adsorbs organic matter and moisture from the atmosphere, leading to changes in its surface condition over time, causing a variation in adhesion strength. Therefore, to consistently achieve adhesion strength, a surface modification treatment is necessary to chemically stabilize the oxide film against temperature and humidity changes.

Automotive manufacturers in EU and USA have included surface modification treatment in their standard specifications, in addition to surface cleaning, with the aim of improving the adhesiveness and storage stability of aluminum alloy oxide films. This ensures the long-term stability of adhesive strength<sup>9)</sup>. Hence, this section introduces Kobe Steel's research on the mechanism by which adhesive strength manifests at the interface between adhesive and metal material, providing a foundation for understanding the surface conditions of metal materials that excel in adhesion stability.

## 2.1 Improvement of adhesiveness with silane coupling agent

The adhesion action occurring at the interface between the adhesive and the oxide film has given rise to various hypotheses, including the anchoring effect, chemical bonding such as acid-base bonding and covalent bonds, as well as physical bonding like hydrogen bonding and van der Waals forces. In reality, these factors act in combination, and it is

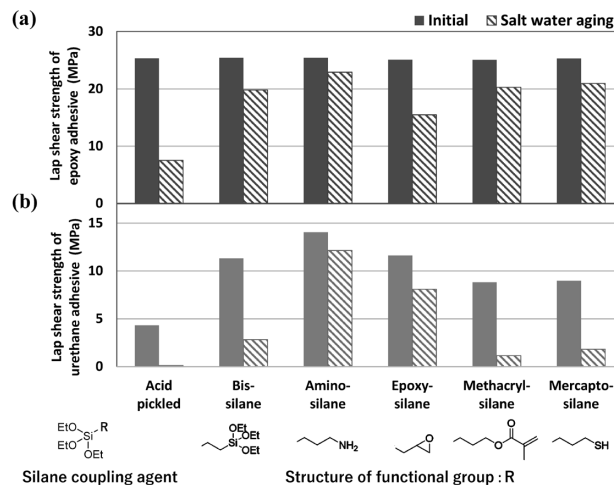


Fig.3 Adhesion test results of silane-treated aluminum alloy with (a) epoxy and (b) urethane adhesive. 6000 series alloy, 1mmt, aging condition; 5%NaCl aq., 40°C, 14 days

believed that their contributions vary, depending on the types of adhesive and oxide film<sup>10)</sup>. For example, commonly used structural adhesives such as epoxy-based adhesives and urethane-based adhesives are thought to exhibit adhesive strength between the “functional groups of the resin that constitutes the adhesive” and the “functional groups on the surface of the oxide film”<sup>11), 12)</sup>. Additionally, the improvement of adhesiveness through coupling agents that excel in bonding with both the resin and the oxide film has been reported<sup>13)</sup>. Hence, investigations have been conducted into the relationship between the state of the metal surface after surface modification and adhesiveness.

Aluminum alloy sheets surface-treated with silane coupling agents comprising a variety of functional groups have been bonded with epoxy adhesive and urethane adhesive to evaluate the joint strength before and after degradation due to saltwater immersion. The results are shown in Fig. 3. In the case of joints bonded with epoxy adhesive, there is no significant difference in strength before saltwater immersion, as all evaluations have led to base aluminum fracture. However, after saltwater immersion, the use of coupling agents has resulted in less strength reduction compared with the acid-pickled material. On the other hand, in the case of urethane adhesive, the improvement effect of adhesiveness for different types of functional groups is significant. Particularly, the use of coupling agents containing amino groups has demonstrated a superior adhesiveness improvement effect. To elucidate the mechanisms of these effects, the following sections introduce the results of the analysis of the adhesive interface states using

various spectroscopic methods. This analysis has utilized bis-silane and amino-silane treated materials, which demonstrated effects for epoxy adhesive and urethane adhesive, respectively.

## 2.2 Mechanism of adhesion strength improvement for epoxy adhesive

In recent years, there has been progress in research on the methods of analyzing the adhesion action directly and non-destructively at the interface between the adhesive and the oxide film<sup>14</sup>. As an example, Fig. 4 shows the results of the analysis of the electronic state of aluminum oxide film before and after epoxy adhesive coating, using Hard X-ray Photoelectron Spectroscopy (HAXPES). The electron state of aluminum atoms constituting the oxide film is represented by the broad spectrum, and the peak top position shifts to the low-energy side after coating the adhesive (Fig. 4(a)). This indicates the donation of electrons from the functional groups of the adhesive's resin to the aluminum atoms in the oxide film. The electron transfer, namely the acid-base interaction, occurs with the adhesive's resin acting as the electron donor (base) and the oxide film as the electron acceptor (acid)<sup>15</sup>. The HAXPES spectrum of the bis-silane treated material shows a greater peak shift after adhesive coating, compared with the acid-pickled material, suggesting a stronger acid-base interaction. Fig. 4(b) presents the analysis results by fitting the HAXPES spectra to the acid-pickled material and bis-silane treated material, separating the peaks corresponding to the chemical bonding that constitutes the oxide film. The analysis has been conducted on the assumption that the peaks labeled Al-O represent the bonding

that makes up the oxide film, the peaks labeled -OH bonds (Al-O-Si-OH, Al-OH) represent the bonding on the oxide film surface, and the peaks labeled -O-C bonds (Al-O-Si-O-C, Al-O-C) represent the bonding with the adhesive. The bonding on the acid-pickled material is Al-OH, while the bonding on the bis-silane treated material includes Al-OH and silanol groups (Si-OH) in Al-O-Si-OH, indicating a higher proportion of OH groups on the oxide film surface. Furthermore, the analysis of the bonding state after adhesive coating has revealed that the bonding quantity with the adhesive is higher for the bis-silane treated material (Al-O-Si-O-C and Al-O-C) compared with the acid-pickled material (Al-O-C). Silane coupling agents are known to generate silanol groups through hydrolysis during surface treatment, and these groups bond with the oxide film (Fig. 5). Silanol groups have a higher acidity than the hydroxyl groups (Al-OH) present

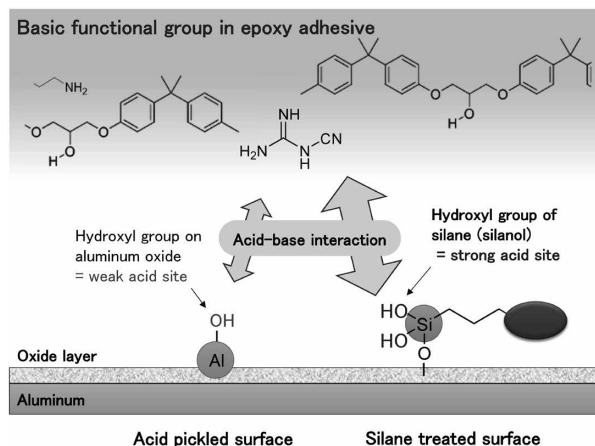


Fig.5 Proposed adhesion mechanism between epoxy adhesive and acid-pickled or silane-treated aluminum surface

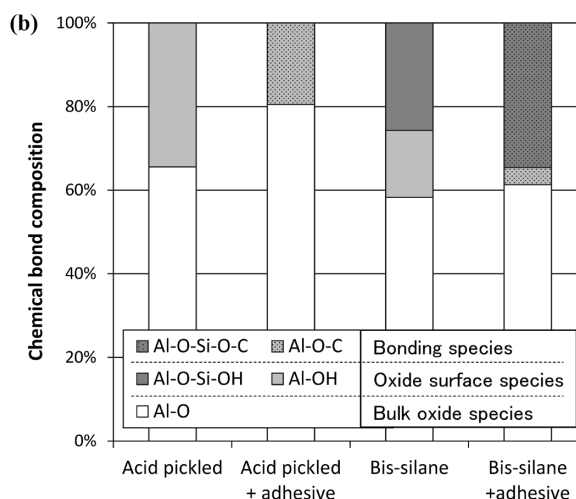
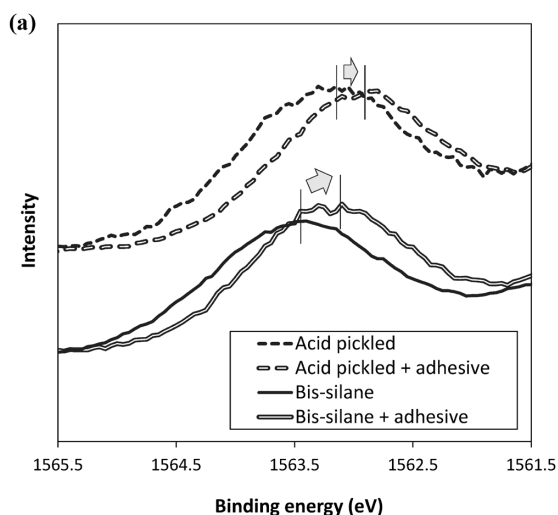
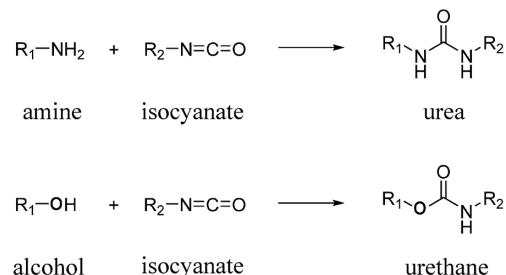


Fig.4 HAXPES results of acid pickled or bis-silane-treated 6000 series aluminum alloy before and after epoxy adhesive coating. (a) Al 1s spectra, (b) curb-fitting result of chemical bonds in oxide layer

in aluminum oxide, and oxides containing silanol groups, such as silicic acid, are known to have excellent compatibility with organic compounds of a basic nature compared with aluminum oxides containing Al-OH<sup>16), 17)</sup>. Therefore, it is believed that silane coupling treatment results in the generation of acidic silanol groups on the oxide film, leading to a greater and stronger acid-base bonding with the adhesive, improving the bonding properties between the adhesive and the oxide film, and suppressing the reduction in strength due to saltwater immersion.

### 2.3 Mechanism of improvement of adhesion strength for urethane adhesive

Urethane adhesive is believed to express adhesive strength by the isocyanate ( $\text{—N=C=O}$ ) in the curing agent reacting with the adherend material surface, forming a covalent bond. Therefore, to investigate the change in chemical bonding on the sample surface, isocyanate was coated on the amino-silane treated material, in which improvement in adhesiveness had been observed. The change was analyzed using Infrared Reflection Absorption Spectroscopy (IRRAS) (Fig. 6). In the amino-silane treated material, an absorption peak around 1,640  $\text{cm}^{-1}$  is observed. In contrast, the acid-pickled material, which exhibited inferior adhesiveness, shows almost no absorption peak in this region. Therefore, it is believed that this absorption peak indicates the chemical bonding related to the adhesive strength of urethane adhesive. Isocyanate is known to react with various functional groups. For example, it reacts with amines to produce



Scheme 1 Reaction mechanism isocyanate with functional groups

urea ( $\text{—NHCONH—}$ ) and bonds with hydroxyl groups, such as those in alcohols, to form urethane ( $\text{—OCONH—}$ ) (Scheme 1). These reactions are characterized by absorption peaks around 1,650  $\text{cm}^{-1}$ . Therefore, the absorption peak around 1,640  $\text{cm}^{-1}$  in Fig. 6 is attributed to the urea bonding generated by the reaction between the amino group introduced to the oxide film surface through amino-silane treatment and the isocyanate in the urethane adhesive. The covalent bond formation between the oxide film and the adhesive has improved adhesiveness. Furthermore, with other silane treated or acid pickled materials, varying degrees of adhesion strength have been obtained. It is assumed that these agents introduced silanol groups onto the oxide film surface through silane coupling agents or that the hydroxyl groups on the oxide film surface bonded with the isocyanate, generating urethane bonding, and expressing adhesion strength. Urethane adhesive typically exhibits limited adhesiveness to metal materials and usually requires the use of specialized primers or coatings for pretreatment. However, performing modification treatment on the oxide film as described provides a certain level of strength stability without the need for a primer.

### 2.4 Effect on dissimilar metal materials

As observed in the improving of aluminum oxide film's adhesiveness to the adhesive by modifying the film, comparable effects can be anticipated for dissimilar metal materials. Various metal materials were subjected to blasting treatment followed by silane coupling treatment, and the adhesiveness to epoxy adhesive was evaluated as shown in Fig. 7. It is observed that, in addition to aluminum and stainless steel, the adhesiveness of titanium, which exhibited interfacial delamination with blasting treatment alone, as demonstrated in Fig. 2, can also be improved. By enhancing the adhesiveness of metal materials through appropriate surface treatment and suppressing interfacial delamination,

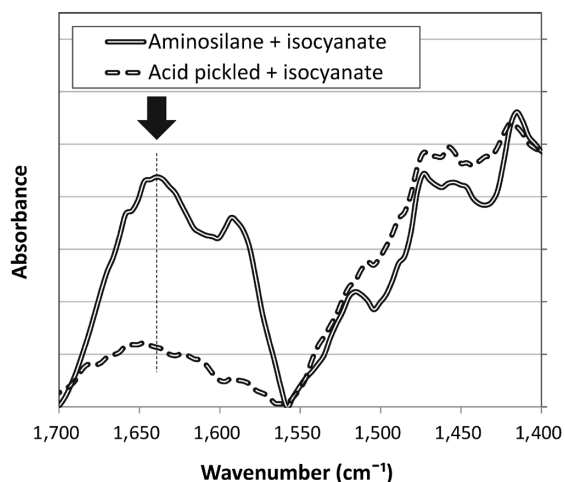


Fig.6 FT-IR spectra of acid-pickled and amino-silane-treated 6000 series aluminum alloy after isocyanate compound coating (data was taken by reflection absorption spectroscopy method under nitrogen stream)

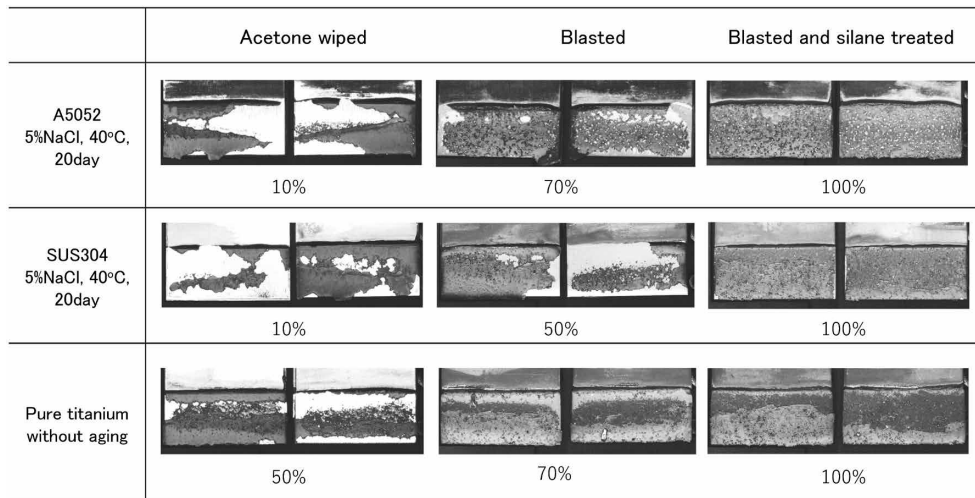


Fig.7 Fracture surface structure and rate of cohesive failure mode of metals with different surface preparation

it is possible to mitigate the decrease in strength in adhesive joints, thereby enhancing the reliability of long-term strength. Furthermore, the establishment of suitable surface modification technologies for different materials and adhesives holds the potential for further utilization of adhesive joining, especially in the context of dissimilar material joints.

### 3. Reliability of adhesion strength

When using adhesive bonding over an extended period, it is crucial that the designed joint strength does not easily deteriorate in the face of external environmental changes, such as temperature, humidity, ultraviolet radiation, and repetitive stress. In other words, adhesive durability becomes paramount. The durability of adhesive itself can be estimated to some extent by controlling the type of resin and the skeleton structure that constitutes the adhesive and evaluating the resin material in practical terms. On the other hand, predicting the durability of adhesion strength with the material involves considering changes in the adhesive, oxide film, and the interface between them, making it challenging. Hence, this section will introduce the mechanisms through which strength reduction occurs at the adhesive interface due to water, which requires particular attention when using adhesive bonding over an extended period. Also discussed are approaches to reliability evaluation that take these effects into account.

#### 3.1 Factors of strength reduction

Adhesive undergoes changes in its chemical structure during the curing process, often resulting in volume changes such as expansion or contraction,

as well as the generation of bubbles. Particularly at the adhesive interface, structural defects and compositional imbalances are prone to occur. As a result, the interface between the adhesive and the metal is more susceptible to water infiltration than the adhesive itself<sup>18)</sup>. When water infiltrates the adhesive interface, it not only hinders the adhesion action between the adhesive and the oxide film, but also leads to various changes in the state, such as hydration of the oxide film and alterations in pH, as predicted by theoretical calculations. Consequently, this can result in a reduction in adhesion strength<sup>19)</sup>.

Therefore, water infiltration into the adhesive interface and the associated changes in the oxide film's state are significant factors causing a reduction in the adhesion strength of metal materials. The impact of these phenomena becomes more pronounced in the presence of factors that accelerate these processes. For instance, higher environmental temperatures cause the resin to become plasticized, accelerating the diffusion of water and, consequently, promoting strength reduction. Additionally, applying stress to the joint exacerbates the reduction in strength<sup>20)</sup>. It is known that applying stress to the joint has the effect of expanding voids in the resin or adhesive interface, facilitating water absorption. Furthermore, the stability of the metal oxide film significantly decreases in the presence of chloride ions, leading to corrosion reactions, dissolution of the base metal, and changes in pH that can invade the adhesive interface. Therefore, special attention is required when using adhesives in environments exposed to saltwater (Fig. 8)<sup>21)</sup>.

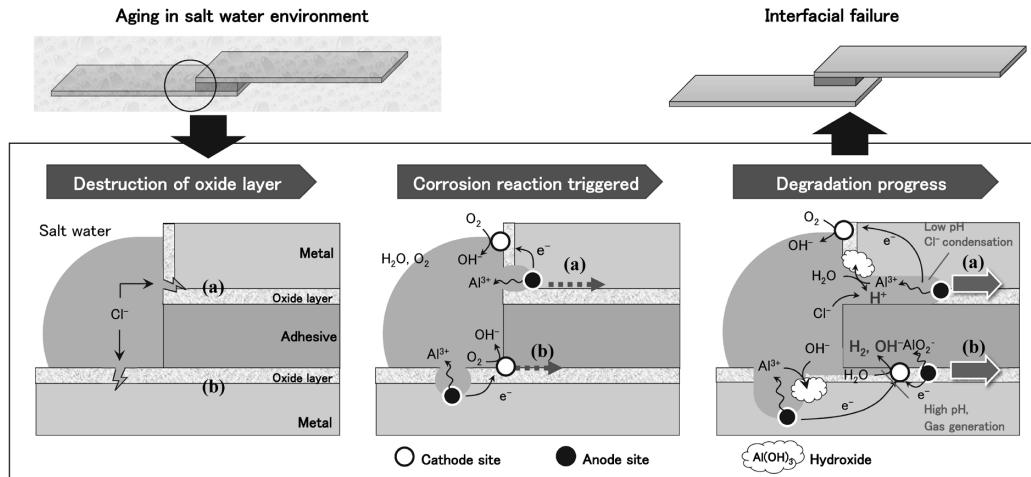


Fig.8 Degradation mechanism between adhesive-oxide layer interface in salt water condition  
 (a) crevice corrosion, (b) cathodic delamination

### 3.2 Measures to inhibit strength reduction

To mitigate the reduction in adhesive strength, two key measures are crucial: “preventing water infiltration into the adhesive interface” and “restraining changes in the oxide film’s state.” Regarding measures on the metal side, the surface modification technology discussed in Section 2 becomes essential.

To prevent the infiltration of water into the adhesive interface, it is crucial to enhance the adhesion between the adhesive and the oxide film, eliminating crevices and voids between them, and thereby preventing the creation of pathways for water infiltration. As illustrated in Fig. 3, the use of a silane coupling agent has been shown to increase the bonding between the adhesive resin and the oxide film, contributing to improved adhesion durability in a saline environment. Furthermore, as a modification treatment to suppress changes in the oxide film’s state, various protective film treatments have been employed for surface pretreatment in painting, such as chromate treatment, anodizing, and zinc phosphate treatment. These treatments create stable protective films against acids, bases, and chloride ions and have been utilized for an extended period<sup>22)</sup>. On the other hand, while these protective films excel in chemical stability, the protective film itself may become a starting point for fractures depending on the adhesive’s strength characteristics. Hence, the selection of an appropriate film depends on the adhesive used, the operating environment, and the required product lifespan.

### 3.3 Strength durability in real environment

When designing a product using adhesive joining, it is essential to consider the expected decrease in adhesion strength over the product’s lifespan and to design joint strength accordingly. To achieve this, it is desirable to conduct an accelerated evaluation that intentionally exposes the joint over a specific period to environmental factors known to have a significant effect on adhesion strength, as described in Section 3.1. This evaluation allows for predicting the strength lifespan in actual market conditions.

The following presents examples of efforts to improve adhesion strength reliability in the automotive market outside Japan. The auto manufacturers in the EU and USA have established their own criteria. In Europe, as part of accelerated tests simulating market environments, adhesive joints undergo cycle tests combining saltwater spray and drying for several thousand hours, with criteria specifying that interfacial delamination after strength testing remains below a certain percentage. In North America, a different approach is taken, where pre-oiled test pieces are adhered, subjected to environmental cycle tests with applied stress, and evaluated for their strength lifespan<sup>23)</sup>. To meet these stringent testing criteria, surface modification treatments applied to aluminum alloys include barrier treatment using a composite oxide with titanium and zirconium (TiZr treatment) in Europe and a coupling agent treatment (A951 treatment) based on organic phosphoric acid in North America<sup>9), 24)</sup>. These treatments have been adapted to volume production. Both treatments have demonstrated the ability to maintain the majority of the initial adhesion strength even after more

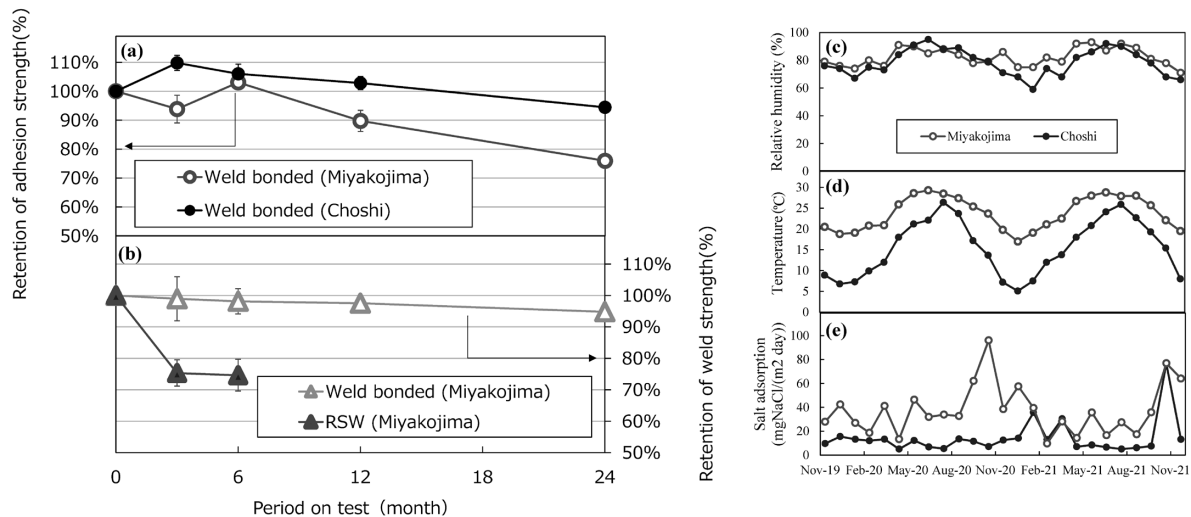


**Fig.9** Joint strength result of bonded steel under climate exposure test (a) weld-bonded specimen at Miyakojima and Choshi, (b) weld-bonded and spot-welded specimen at Miyakojima, climate conditions during exposure period (c) relative humidity, (d) temperature, (e) salt adsorption

than ten years of use in various regional market environments. It is inferred that reliability has been established over an extended period on the basis of the results of “1 to 2 months of accelerated laboratory testing” and “several years of actual vehicle driving tests”<sup>25)</sup>.

Also in Japan, there is a correlation being established between the residual strength of adhesive joints evaluated by recovering vehicles that have been on the market for several years and the accelerated laboratory evaluation results based on the adhesive used in those vehicles. These efforts have led to estimating a correlation between “short-term accelerated tests in high-temperature and high-humidity environments” and “results equivalent to several years of actual driving”<sup>26), 27)</sup>.

Finally, the benefits of using adhesive in combination with other joining methods for durability are introduced. Steel sheets were joined using resistance spot welding or a weld-bonding method combining adhesive and resistance spot welding. After exposing them to environmental conditions for a certain period at the outdoor testing sites in Choshi City or Miyakojima City, the remaining strength of the joints was evaluated, and the results are shown in **Fig. 9**<sup>28)</sup>. As shown in Fig. 9(a), even when exposed to harsh corrosive conditions such as the sea breeze and sunlight for two years, the majority of the initial strength is maintained. This indicates that the adhesive used in this test, a structural epoxy adhesive for automobiles, possesses high durability. Furthermore, in Miyakojima City, where the average temperature is higher and the salt adhesion level is greater, a more significant decrease in strength is observed

(Fig. 9(c)-(e)). This result reflects the influence of the factors causing strength reduction as discussed in Section 3.2. It should be noted that in joints joined only by spot welding, corrosion occurs around the welded area, and the joining strength decreases shortly after the exposure. In contrast, the weld-bonded joint whose welded area is sealed with adhesive is protected from the corrosive environment, resulting in the suppression of strength reduction in the welded area (Fig. 9(b)). Thus, by combining adhesives with other joining technologies, synergistic effects can be expected, leading to an enhancement of joint strength over an extended lifespan.

## Conclusions

The expectations for adhesive joining are increasing year by year. In the automotive industry, particularly in response to the electrification trend leading to the lightweighting of vehicles and increased production of batteries, the adoption of adhesive joining is expected to expand further. Additionally, in non-automotive industries, there is a growing demand for adhesive joining of dissimilar materials and productivity improvement. Considering societal challenges such as a shortage of welders<sup>29)</sup>, adhesive joining is anticipated to become one of the primary joining technologies for metal materials across various industrial sectors.

On the other hand, as mentioned in this paper, to be able to rely on adhesive joining, it is crucial to consider the surface conditions of metal materials. Proper management of their state, including surface treatment, becomes essential. Furthermore, since

the products, environments, and performance requirements vary among users, it is important to organize the relationships among adhesives, metal materials, their surface conditions, and the strength durability in the specifications in each case. With the consolidation of such cases and experiences, there is an expectation that the strength reliability of adhesive joining will continue to improve.

## References

- 1) K. Yamamoto et al. Mazda Technical Report. 2019, No.36, pp.283-288.
- 2) K. Haruga. Journal of the Adhesion Society of Japan. 2007, Vol.43, No.8, pp.319-324.
- 3) Y. Takahashi et al. Journal of the Adhesion Society of Japan. 2021, Vol.57, No.5, pp.201-210.
- 4) Isayama Eizo et al. Journal of Japan Institute of Light Metals. 1985, Vol.35, No.3, pp.176-187.
- 5) H. Yamamoto. The journal of the Surface Finishing Society of Japan. 2018, Vol.69, No.9, pp.376-379.
- 6) S. Maeda. Journal of the Japan Color Material Association. 2011, Vol.84, No.9, pp.313-320.
- 7) T. Usami et al. Sumitomo light metal technical reports. 1993, Vol.34, No.3, pp.171-178.
- 8) M. Fukumura. The journal of the Surface Finishing Society of Japan. 1979, Vol.30, No.4, pp.170-179.
- 9) European Aluminum Association. EAA Aluminum Automotive Manual - Joining 9. Adhesive bonding. Version 2015. [https://european-aluminium.eu/wp-content/uploads/2022/11/9-adhesive-bonding\\_2015.pdf](https://european-aluminium.eu/wp-content/uploads/2022/11/9-adhesive-bonding_2015.pdf), (Accessed 2022-12-14).
- 10) K. Takemoto et al. Adhesive Chemistry. Kodansha, 1997, p.42.
- 11) S. Maeda. Journal of the Adhesion Society of Japan. 2005, Vol.41, No.10, pp.404-414.
- 12) K. Sensui et al. Chemical Communications. 2019, Vol.55, Issue 98, pp.14833-14836.
- 13) H. Yamabe. Journal of the Japan Color Material Association. 2006, Vol.79, No.4, pp.140-146.
- 14) Y. Takahashi. Journal of Surface Analysis. 2022, Vol.28, No.2, pp.102-107.
- 15) Y. Takahashi. The journal of the Surface Finishing Society of Japan. 2021, Vol.72, No.4, pp.238-241.
- 16) M. Nakazawa. Journal of the Japan Color Material Association. 1995, Vol.68, No.7, pp.424-433.
- 17) J. van den Brand. On the adhesion between aluminium and polymers. Ph.D. diss. TU Delft, 2004, pp.6-10.
- 18) R. Iwasaki et al. Journal of the Adhesion Society of Japan. 2007, Vol.43, No.3, pp.81-88.
- 19) Computational Chemistry Promotion Foundation. Supercomputer and Industrial Use Case Collection. 2022, No.12, pp.32-33.
- 20) M. Mitoh. Journal of Japan Institute of Light Metals. 1991, Vol.41, No.10, pp.650-659.
- 21) S. Askarinejad et al. Corrosion Science. 2022, Vol.203, Article 110356.
- 22) T. Shimakura. The journal of the Surface Finishing Society of Japan. 2010, Vol.61, No.3, pp.223-231.
- 23) Ford Motor Company. Ford Laboratory Test Method BV101-07. Stress Durability Test for Lap-Shear Bonds.
- 24) Y. Ota et al. R&D Kobe Steel Technical Reports. 2017, Vol.66, No.2, pp.82-85.
- 25) I. Wilson et al. SAE Transactions Section 5. 1997, Vol.106, No.5, pp.6-14.
- 26) Y. Himuro et al. Mazda Technical Report. 2012, No.30, pp.219-223.
- 27) M. Anan. Kobelnix. 2020, Vol.28, No.50, pp.1-4.
- 28) H. Katsuno et al. JSCE Materials and Environments, ZAIRYO-TO-KANKYO 2022 Abstracts. 2022-05-25/27, Corrosion Prevention Society of Japan, 2022, pp.23-24.
- 29) M. Osawa. Journal of light metal welding. 2023, Vol.61, No.1, pp.2-6.